MARCH 1959

VOLUME 4 (1959) No. 2

GREGG M. SINCLAIR LIBRARY
UNIVERSITY OF HAWAII
8-7-63

NUCLEAR INSTRUMENTS & METHODS

A JOURNAL ON ACCELERATORS, INSTRUMENTATION AND TECHNIQUES IN NUCLEAR PHYSICS

EDITOR: K. SIEGBAHN - UPPSALA

CONTENTS

EDWARD A. SILVERSTEIN, Calculation of the G factor for gas scattering experiments 53
E. MALAMUD and A. SILVERMAN, Magnetic measurements on the Cornell alternate gradient synchrotron 67
H. BIENLEIN, K. GÜTHNER, H. VON ISSENDORFF und H. WEGENER, Eine Apparatur zur Messung der longitudinalen Elektronenpolarisation durch Mott-Streuung 79
W. MÜLLER-WARMUTH und P. SERVOZ-GAVIN, Hochstabilisierende Protonenresonanz-Magnetfeldregelung mit elektronischem Integrator 90
MORTON D. KOSTIN, Gas scattering in a strong focusing synchrotron 99
C. SHARP COOK, Calculation of the penetration of gamma rays through the edges of a $\frac{1}{2}$-inch diameter lead collimator 103
T. R. GERHOLM and B.-G. PETTERSON, Instrument for electron-gamma directional correlation experiments with magnetic momentum selection 107
WOLFGANG GRUHLE, Impuls-Zeitformer für schnelle Koinzidenzstufen 112
F. A. MULLER, A fast scaling stage 115
E. BALDINGER, P. SANTSCHI and P. WEHRLI, High speed transistorized scale-of-two (Letter to the Editor) 117
PIERRE AMIOT, The selection of stainless steels for use in liquid hydrogen bubble chambers (Letter to the Editor) 118
Book reviews 120

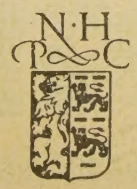

NORTH-HOLLAND PUBLISHING COMPANY - AMSTERDAM

NUCLEAR INSTRUMENTS AND METHODS

A journal on accelerators, instrumentation and techniques in nuclear physics

EDITOR: K. SIEGBAHN, UPPSALA

EDITORIAL BOARD:

J. B. ADAMS (CERN)
E. AMALDI (Rome)
H. L. ANDERSON (Chicago)
K. T. BAINBRIDGE (Cambridge, Mass.)
C. J. BAKKER (CERN)
P. R. BELL (Oak Ridge)
R. E. BELL (Montreal)
A. BERTHELOT (Saclay)
H. BRINKMAN (Groningen)
S. DE BENEDETTI (Pittsburgh)
M. DE HEMPTINNE (Louvain)
A. DE-SHALIT (Rehovoth)
M. DEUTSCH (Cambridge, Mass.)
S. DU TOIT (Pretoria)
B. S. DŽELEPOV (Leningrad)
W. GENTNER (CERN)
P. C. GUGELOT (Amsterdam)
H. HALBAN (Paris)
O. HAXEL (Heidelberg)
P. HUBER (Basel)
D. J. HUGHES (Brookhaven)
S. KIKUCHI (Tokyo)
J. KOCH (Copenhagen)
M. S. KOZODAEV (Moscow)
S. LIVINGSTON (Cambridge, Mass.)
E. M. MCMILLAN (Berkeley)
M. G. MEŠČERJAKOV (Moscow)
P. B. MOON (Birmingham)
M. L. OLIPHANT (Canberra)
W. PAUL (Bonn)
A. S. RAO (Bombay)
G. SALVINI (Rome)
P. SAVIĆ (Belgrade)
P. SCHERRER (Zürich)
CH. SCHMELZER (CERN)
H. W. B. SKINNER (Liverpool)
R. TANGEN (Blindern)
D. TAYLOR (Harwell)
V. I. VEKSLER (Moscow)
O. WERNHOLM (Stockholm)
G. VON DARDEL (CERN)
R. R. WILSON (Cornell)
S. D. WINTER (Saclay)

INSTRUCTIONS FOR CONTRIBUTORS

Contributions may be sent to the Editor, Professor K. Siegbahn, Institute of Physics, University of Uppsala, Sweden, either directly or through the intermediation of one of the members of the Editorial Board. Contributions may be written in English, French or German but should always, except for very short papers, be supplied with a brief abstract in English. Figures should be in inked original drawings or glossy prints and they should be sufficiently large. Contributors should make sure that important details in drawings and photographs will show up clearly in the diminished copy used by the publisher.

Books for review should be sent to Professor Siegbahn.

Objective and descriptive material on endeavours and product developments from the industry for the section "Spotlight on Industry" should be sent directly to the publishers, North-Holland Publishing Company, P.O. Box 103, Amsterdam.

Nuclear Instruments and Methods is published monthly. The subscription price of a volume of 360 pages is $ 17.00 (130 s), postage free.

Subscriptions should be sent to the publishers, North-Holland Publishing Company, P.O.Box 103, Amsterdam or to any subscription-agent.

No part of this issue may be reproduced in any form, by print, photoprint, microfilm or any other means without written permission from the publisher. Reprints, photoprints or microfilms are obtainable at cost from the publisher.

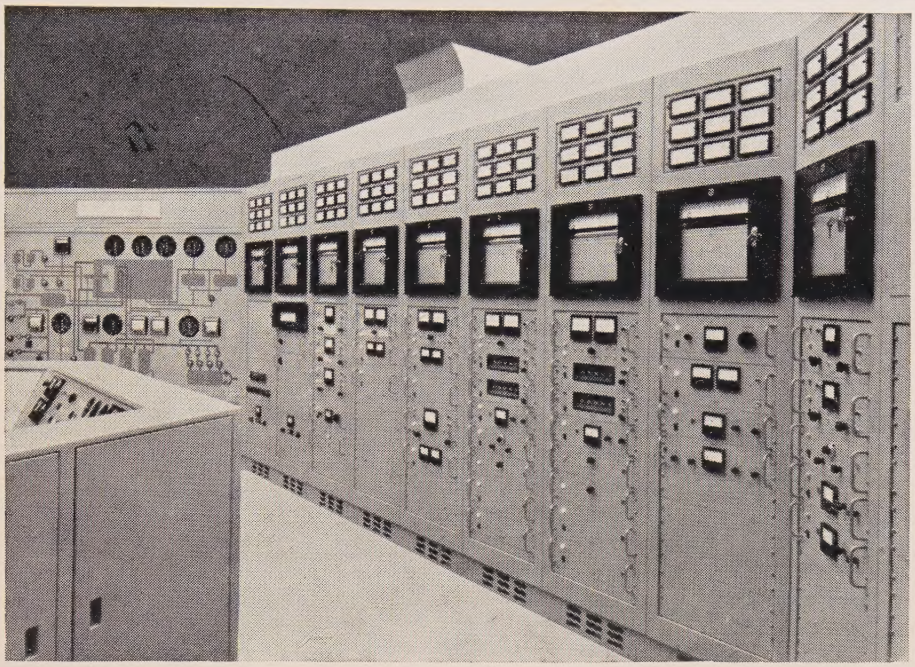

PHILIPS

equipment for
Nuclear Physics and Atomic Energy

Instrument panel for a 20 MW High Flux tank-type reactor. Graphic panel at the left includes flow and pressure meters for the cooling circuits. Centre section houses neutron flux measuring channels with recorders for flux and period as well as recorders indicating coolant temperatures. Right-hand panels contain radioactivity monitors for water and gas circuits. Indication of abnormal operating conditions is provided by annunciators above recorders.

- Synchro-cyclotrons for various final energies.
- Cockcroft-Walton accelerators.
- Generators for very high d.c. voltages.
- Linear electron accelerators.
- Reactor control instrumentation.
- Radiation measuring and detection equipment.
- Civil defence instruments.
- Area monitoring instrumentation.
- Geiger counter tubes.
- Photomultipliers.
- Radio-active isotopes.
- Air & gas liquefiers.
- Vacuum measuring equipment.

PHILIPS

PHILIPS
Nuclear Equipment

For further information please apply to one of the following addresses:

N.V. PHILIPS' GLOEILAMPENFABRIEKEN, Scientific Equipment Department, Eindhoven-Holland
RESEARCH & CONTROL INSTRUMENTS LTD., Instrument House, 207/215, King's Cross Road, London WC1
PHILIPS ELECTRONICS INC., Instruments Division, 750, South Fulton Avenue, Mount Vernon N.Y. U.S.A.

NDO

Société d'Applications Industrielles de la Physique
S. A. I. P.
38, rue Gabriel Crié - MALAKOFF (Seine)

NUCLEAR PHYSICS

PROPORTIONAL COUNTER CPX

- Continuous purification on heated Calcium
- Safety- and isolating rings made of quartz
- Beryllium counting window
- Resolution: 15 to 25% at 6 KV
- With internal source: detection starts from 0.1 KV

OTHER PRODUCTS:

Single-channel kicksorters
Scalers
Scintillation spectrometers
50-Channel Kicksorter "SA 50"
Circulation counters
Pressurised ionisation chambers
Linear amplifiers
Vibrating condensator type D.C. amplifiers
Automatic sampling dispensers.

AGENTS:

BELGIUM:	DRUA, 205 Avenue Van Volxem, BRUSSELS
DENMARK:	LANGEBAEK & SON, Trondhjemsgade 9, COPENHAGEN
NETHERLANDS:	ENRAF-EVERSHED, Van Leeuwenhoeksingel 69, DELFT
ITALY:	AMPERE, Via Felice Casati 8, MILAN
FINLAND:	ISOTEKNO, 13 A Mikontaku, HELSINKI
JAPAN:	RIKEI TRADING C°, Kosato Building, 12-4 Chome Shiba Tamura-Cho Minato-Ku, TOKYO
SWITZERLAND:	A. MAGAT, 28, rue de Vermont, GENEVA
U.S.A.:	LEVIANT, 239 Broadway, N.Y. 7., NEW YORK

Two New TMC Spectrometers

combining • Precise Operation • Moderate Cost • "Add-on" Flexibility

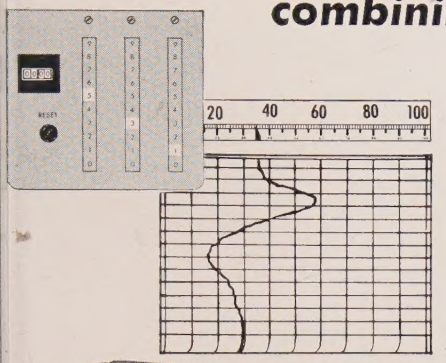

These newest TMC instruments—the Model S-11 Scanning and Recording Spectrometer and the S-12 Manual Spectrometer Assembly—incorporate all the design features and quality components necessary for accurate, stable operation, reliability, and versatility. They are the ideal choice for schools, smaller laboratories and other applications where flexibility is a major requirement. Both are housed in rugged, standard width mobile cabinets, with ample space for future addition of other units.

Individual, basic units used in both Spectrometers include the Model 111 Preamplifier, Model PA-2A combination Linear Amplifier and Single-Channel Analyzer, and Model HV-4A Ultra-Stable Power Supply. In addition, the S-11 has a strip-chart recording system and a RM-1B Rate Meter.

Model S-12
$2300
f. o. b. New Haven

Model S-11
$3900
f. o. b. New Haven

PRIMARY FEATURES — MODEL S-11

- **Continuous scanning between base line settings of 0 to 100 volts with 0.1% linearity (span represented by 18 inches of paper travel).**
- **Scanning speed range 7.5" — 240"/hour (complete scan 2½ hours to 5 minutes). Scanning speed can be instantly changed.**
- **Display size unchanged by change in scanning speed—greatly simplifying data comparison.**
- **Non-overloading Linear Amplifier and Window Amplifier type Single-Channel Analyzer.**
- **Counts per minute (full scale): 300—1,000—3,000—10,000—30,000—100,000.**
- **Selection of probable error—1%, 3%, 10%.**
- **Pre-charged capacitors in time constant network minimize transients when switching probable error range.**
- **Forced filtered air cooling for increased stability and reliability.**

The Model S-12 Manual Spectrometer is the most economical TMC Spectrometer. This basic laboratory instrument utilizes (in addition to the preamplifier, amplifier-analyzer and power supply mentioned above) and SG-3A scaler which features a resolving time of 2.5 us., precision mechanical register and a scale of 1000 using three plug-in etch wired decade units. These features allow a counting rate of 240,000 CPM with less than 1% coincidence loss. Extra space permits adding the necessary units for future conversion to a Model S-11, or to a Model S-13 Dual Peak Spectrometer.

TMC accessories available for use with the "S" series spectrometers include Scintillation Detectors, Sodium Iodide Crystals, Lead Shields and SG-series scalers.

Write for detailed information concerning the new TMC spectrometers, or the new catalog "C" which includes data on all individual units and accessories.

TMC **TECHNICAL MEASUREMENT CORPORATION**

441 WASHINGTON AVENUE, NORTH HAVEN, CONNECTICUT

These names make NUCLEAR POWER

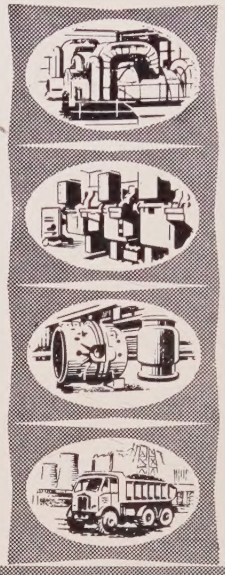

C. A. PARSONS & COMPANY LTD.

A. REYROLLE & COMPANY LTD.

HEAD, WRIGHTSON & COMPANY LTD.

SIR ROBERT McALPINE & SONS LTD.

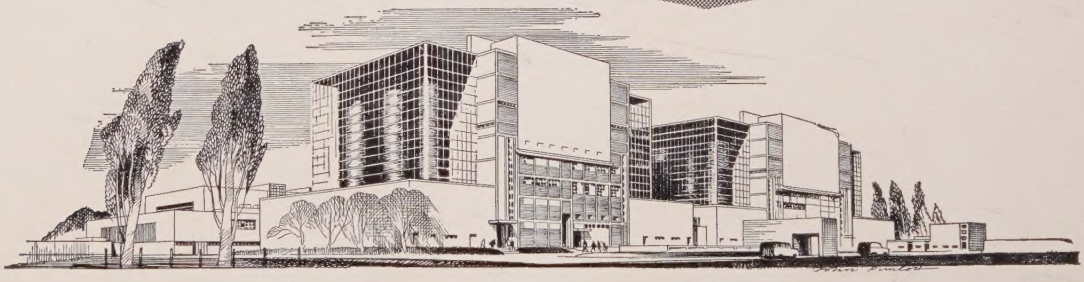

Bradwell, Essex, has leapt into fame as the site of the first commercial nuclear power station in the world to be built by N.P.P.C. Eight names make The Nuclear Power Plant Company Limited. N.P.P.C. thus combines the resources of eight specialist companies whose individual skills are co-ordinated to form a unified team capable of undertaking the construction of complete nuclear power stations throughout the world.

Bradwell nuclear power station will have a guaranteed output of 300 Megawatts. It is being built by The Nuclear Power Plant Co. Ltd. for the Central Electricity Generating Board.

WHESSOE LTD.

STRACHAN & HENSHAW LTD.

ALEX. FINDLAY & COMPANY LTD.

CLARKE, CHAPMAN & COMPANY LTD.

A Greater Britain through Nuclear Power

NPPC

THE NUCLEAR POWER PLANT COMPANY LIMITED · BOOTHS HALL · KNUTSFORD · CHESHIRE · ENGLAND

TGA NP.A.

Announcing the Eldorado 4100

A Fast, Stable Pulse Height Analyzer

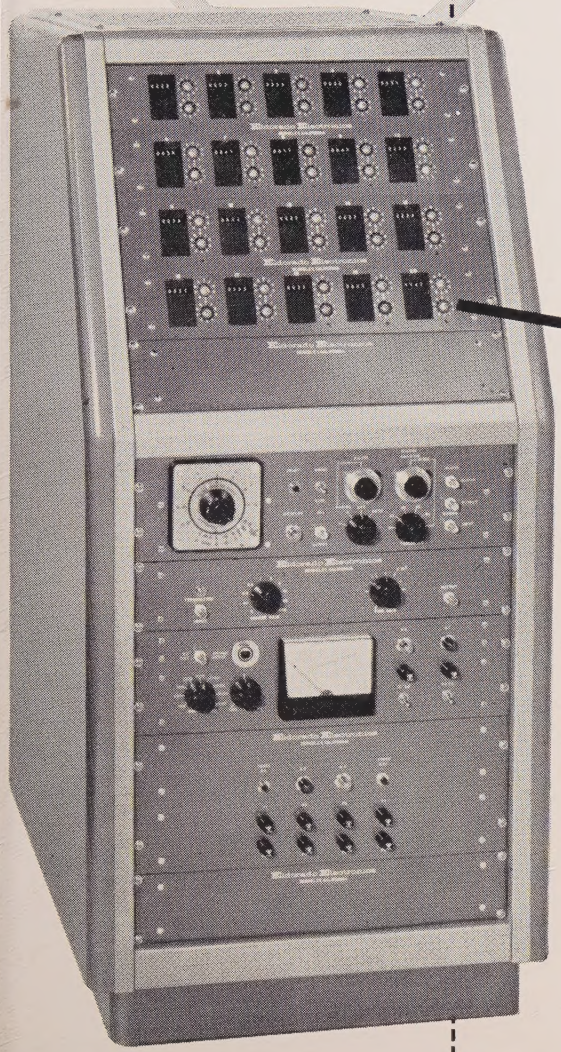

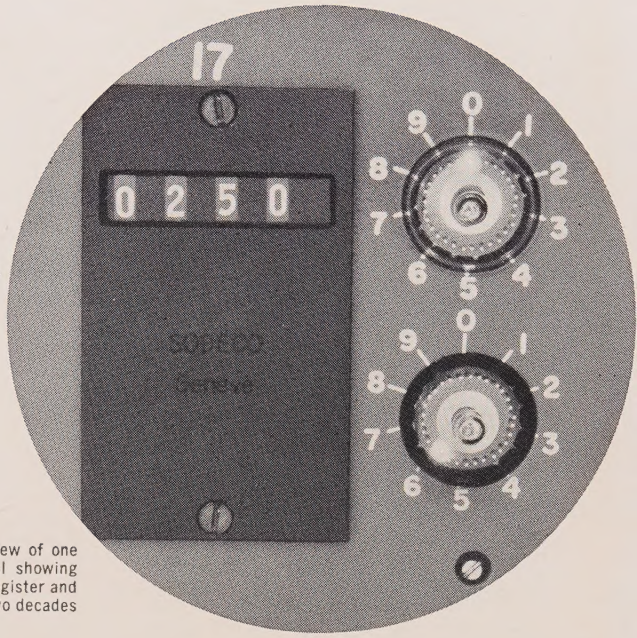

Full size view of one channel showing register and two decades

How Fast?

- ✻ Double pulse resolution better than 0.5 microseconds
- ✻ Dead time less than 0.1 microseconds
- ✻ Average counting rates greater than 10^5 counts per second without baseline distortion or use of temporary storage

How Stable?

- ✻ Channel width less than 1% drift per week
- ✻ Baseline less than 0.1% shift per week
- ✻ Channel triggering level unaffected by changes in input pulse width

Now in production, with 30 day delivery, the 4100 is priced at $8950 f.o.b. Berkeley, California. Shown with optional LA-600 Linear Amplifier and optional High Voltage Power Supply PS-530

BRIEF SPECIFICATIONS

NUMBER OF CHANNELS	20
CHANNEL WIDTH	1.0V NOMINAL
SCALER CAPACITY	10^6 COUNTS/CHANNEL
WINDOW AMPLIFIER INPUT	20V NOMINAL
WINDOW POSITION RANGE	5-105V

For complete details, call your nearby Eldorado Engineering representative or write

See the 4100 at Booth 811, Atom Fair, Cleveland, April 5-10

Eldorado Electronics

2821 TENTH STREET · BERKELEY 10, CALIFORNIA

Phone THornwall 1-4613

Elcor inc.
1225 W. BROAD ST.,
FALLS CHURCH, VA.

MODEL A 309
CURRENT INDICATOR AND INTEGRATOR

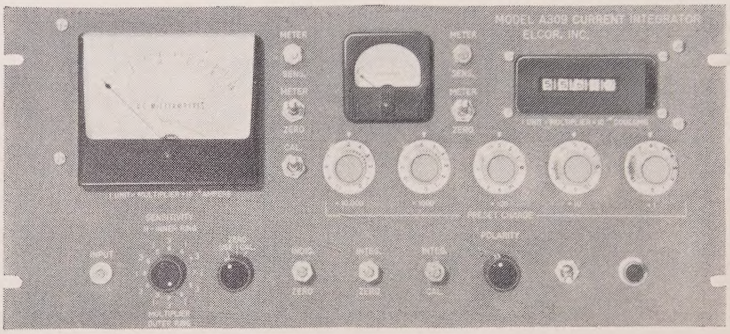

MODEL A 309 A

FEATURES

- Wide current range: 1 x 10^{-3} to 3 x 10^{-9} amp. in 12 switch settings.
- High accuracy: 1% of full scale.
- Internal calibrating current source to check proper operation.
- Front panel switch allows instrument to be used with current of either polarity.
- Pre-setting feature provides means of safeguarding against over-exposure.
- Developed especially for use with Van de Graaff and other high-voltage accelerators.
- Permits many experiments with particle accelerators that would otherwise be difficult or impossible.
- Register readout gives digital accuracy on charge measurement.

The versatility and accuracy of two instruments in one!

1. Measures currents from 1 milliampere to 3 milli-microamperes.
2. Integrates input current and registers accumulated charge.

GENERAL DESCRIPTION—The Model A309 Current Indicator and Integrator is a sensitive current indicator that also measures the total charge collected in a given length of time. Developed especially for use with high-voltage particle accelerators such as the Van de Graaff generator, the instrument is also ideally suited for other applications requiring the measurement of accumulated charge or the integration of a variable current.

The full-scale sensitivity of the instrument can be varied from 1 milliampere to 3 milli-microamperes in twelve ranges. For convenience in checking the performance and accuracy of the instrument, an internal calibrating current source is provided for each range. The accumulated charge is indicated on a 5-decimal digit register. Any number up to 99,999 can be preset into the instrument, and upon reaching the corresponding charge a relay closes to actuate a warning device or control auxiliary equipment. In applications where X-rays are being generated, this feature affords protection against accidental over-exposure.

Input current of either polarity can be measured and integrated, and a front panel switch enables the instrument to be immediately changed from one polarity to the other. Advanced circuit techniques have been employed to achieve low input impedance, negligible drift, and a high overall accuracy and reliability.

Two models are available with the same specifications except for the method of presetting. In the Model A309A the presetting means consists of five front-panel switches. Presetting in the Model A309B is accomplished by manual adjustment of five presetting wheels that are accessible through the hinged cover of the register used in this model.

SPECIFICATIONS

1. Input current for full-scale meter deflection — 1 x 10^{-3} to 3 x 10^{-9} ampere in twelve switch settings.
2. Polarity of input current — positive or negative, controlled by front-panel switch.
3. Current indicating means — 4½" meter.
4. Charge indicating means — 5-decimal-digit register and 2½" meter.
5. Maximum charge indicating capacity — 99,999 units.
   Note: Each unit is equal to one coulomb multiplied by the numerical value of the full-scale current.
6. Maximum integrating time — 28 hours.
7. Integrating rate for full-scale current — 1 unit per second.
8. Method of presetting:
   Model A309A — five front-panel switches.
   Model A309B — five presetting wheels in register.
9. Accuracy (Indicating and integrating accuracy, based on full-scale current) — 1%.
10. Maximum drift — .01% per hour.
11. Maximum input voltage for full-scale current — 2 millivolts.
12. Minimum signal-source impedance for 1% accuracy — 1 ohm divided by numerical value of full-scale current.
13. Calibration — Internal reference current provided for each current range.
14. Power Input — 110–125 volts, 50-60 cps.
15. Dimensions — 19" wide x 8¾" high x 13¼" deep.
16. Mounting — standard 19" relay rack.
17. Weight — approximately 25 lbs.
18. Price: Model A309A — $1674.00.
    Model A309B — $1524.00.

ELCOR,—INC. • 1225 W. BROAD STREET • FALLS CHURCH, VA.

Telephone JEfferson 2-7718

A subsidiary of Fairfax Manufacturing Co., Inc.

Bulletin No. 24-1258

Nuclear Instruments by RCL

for TRAINING • MEDICINE • REACTORS INDUSTRY • MONITORING • RESEARCH

FOR THE FINEST IN EQUIPMENT AND SERVICE, WRITE RCL OR YOUR NEAREST RCL REPRESENTATIVE TODAY.

AUSTRIA
H. & M. Frankel, O.H.G.
Rennegasse 14, Vienna

DENMARK
A. B. C. Hansen Co.
Copenhagen

ENGLAND
Leland Instruments, Ltd.
22–23 Millbank, Westminster
London, S.W.I.

FINLAND
A. B. Wilh, Bensow O.Y.
S. Esplanade 22, Helsingfors

FRANCE, SWEDEN, SWITZERLAND, BELGIUM, NORWAY and ITALY
Estabts. H. V. L.
1026 Chaussee de Louvain
Brussels 14, Belgium

GERMANY
Bureau Technical Medicine
Pfahlplatzchen 5, Bamberg

GREECE
Ph. Georgakis
15 Amerikis St., Athens (K)

NETHERLANDS
HVL (Nederland) N.V., i.o.
33, Wassenaarseweg,
The Hague

PORTUGAL
Soquimica
Rua Dos Correeiros, 113.3. o,
Lisbon

SPAIN
Carlos Rafael Mares, S.L.,
Calle de Valencia, 333,
Barcelona

Pulse Height Analyzers. The most revolutionary instrument in the analyzer field today is the completely new, all transistorized RCLiac 128 Scaler-Analyzer. The RCLiac 128, shown second from the top, performs every operation from gross counting through scintillation-spectroscopy.

RCL's 256-Channel Pulse Height Analyzer, (top right), is *The Analyzer* of proven reliability — from 10 seconds to 27 hours of preset time, background subtraction, automatic programming, split memory, decimal and logarithmic readout, and many other new features. RCL also offers 1024-Channel Neutron Time-of-Flight Analyzers, Single Channel Differential Analyzers, and both Recording and Medical Spectrogammeometers.

Instruments. RCL instruments are of the finest design, construction and workmanship in the nuclear field. Among the many instruments manufactured by RCL are Linear Amplifiers, Scalers, Linear and Logarithmic Count Rate Meters, Precision High Voltage Power Supplies, and Precision Pulse Generators. All instruments suitable for standard 19" rack mounting. Cabinet supplied, if desired.

Health Protection. The protection of personnel is of prime importance in the nuclear world. To aid in this task RCL offers equipment such as Alpha Hand Monitors, Beta-Gamma Hand and Shoe Monitors, Area Monitrons, Neutron Survey Meters and "Quintectors," five detector portal or critical area monitors.

Reactor Controls. The first nuclear reactor controls manufactured by a non-AEC facility were supplied by RCL. Today, RCL reactor control instrumentation — such as Log N, Period, Sigma, Magnetic and Composite Safety Amplifiers, Log Count Rate Meters, and Power Supplies — can be found in reactor installations throughout the world.

Detectors. Among the many different types of detectors produced by RCL are Alpha-Beta, Gas Flow, Beta-Gamma Thin Wall, Gamma, Fast or Slow Neutron, Gas Sample, Cosmic Ray, Scintillation, Halogen Quenched Beta-Gamma, and Ionization Chambers.

Accessories. RCL can fill almost every accessory need immediately. For your convenience RCL keeps a constant supply of items such as radiation shields, sample holders, sources, safety equipment and clothing, timers, glassware, scintillation crystals, sample preparation and handling equipment, etc.

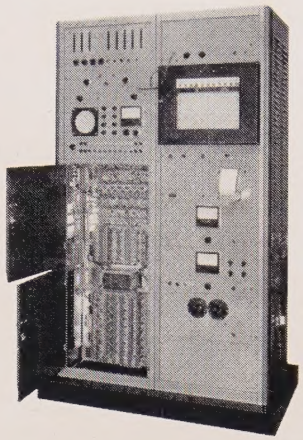

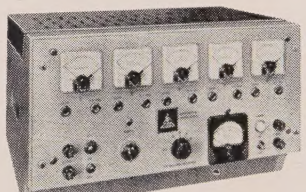

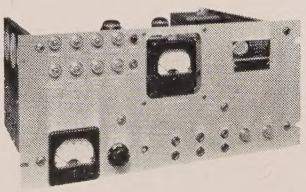

RCL

RADIATION COUNTER LABORATORIES Inc.

NUCLEONIC PARK • SKOKIE, ILLINOIS
ORchard 3-8700

INTERNATIONAL

advertise

YOUR NUCLEAR PRODUCTS IN

sell

YOUR NUCLEAR PRODUCTS

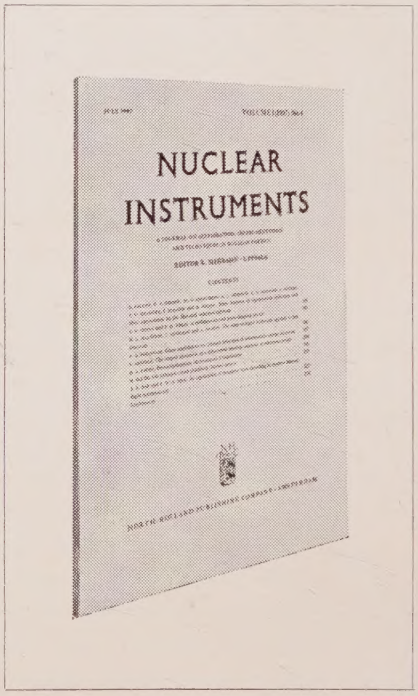

reap

YOUR NUCLEAR SALES
REWARDS

world wide

KEY NUCLEAR MANAGEMENT
NUCLEAR SCIENTISTS
NUCLEAR ENGINEERS
NUCLEAR PRODUCTION
PERSONNEL

SUBSCRIBE TO

you reach

THE WHOLE
NUCLEAR SALES WORLD IN

Entirely international in scope Nuclear Instruments and Methods is the one nuclear scientific journal that has an established subscription clientele throughout the whole world-where-ever nuclear men are at work—they want your nuclear products—they need your nuclear products—advertise in Nuclear Instruments and tell them WHAT – HOW – WHERE they can get your nuclear products

GO INTERNATIONAL WITH YOUR SALES PROGRAM TODAY WRITE

WILLIAM F. BAARS - ADVERTISING MANAGER NORTH-HOLLAND PUBLISHING COMPANY

P.O. BOX 103 – AMSTERDAM, HOLLAND

INTERNATIONAL

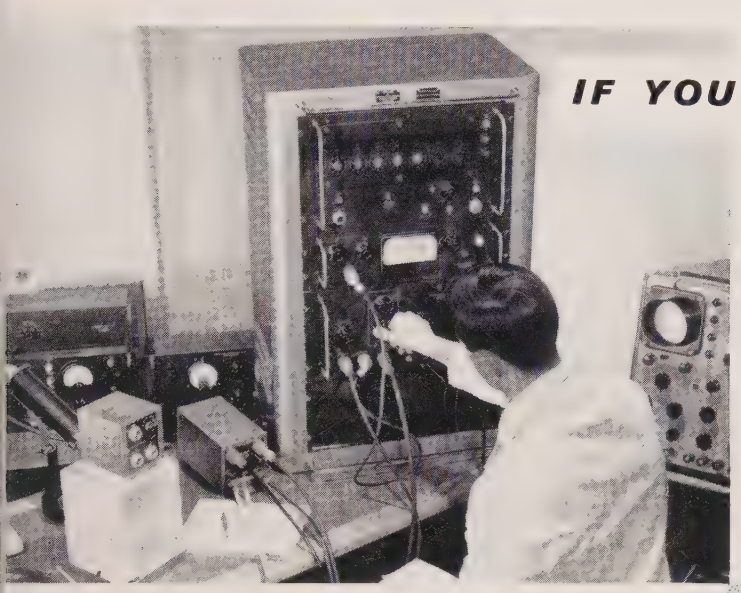

IF YOU ARE INTERESTED IN

NUCLEONIC COUNTING

Nucleonic Counting Equipment Type 127A.
Designed specifically for use in the nucleonic field where accurate, high speed counting is essential. This range of equipment comprises Scaling Unit, Amplifier-Discriminator, E.H.T. Unit, Head Amplifier, Quench Unit, Ratemeters and Timing Unit.

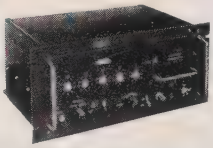

Scaling Unit Type 1221C.
A reliable general purpose Scaling Unit with a resolving time of 500μ secs. and a maximum count of 10^5.

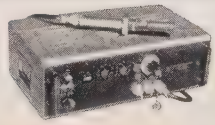

G.M. Counter Type 121A.
An inexpensive and reliable low-speed counting equipment for use in schools and technical colleges.

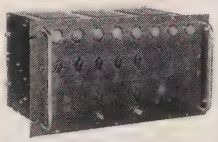

Timing Unit Type 146A.
An advanced design in Timing Units, this instrument employs high speed relay start/stop control.

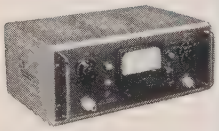

E.H.T. Power Unit Type 105A
Designed for nucleonic work—this gives continuously variable stabilized voltages from 300 - 3,300 volts d.c.

YOU NEED THIS NEW CATALOGUE!

If your interest lies in fact, in any aspect of Nuclear Physics, Radiation Monitoring, Radio-active Ore Surveying and Industrial Control and Measurement, then this new comprehensive catalogue should have a place in your library.

Here at Etelco, research and development are proceeding continuously to widen the range of counting, measuring and control instruments, and we invite you to examine our progress.

Cut out and mail today

ETELCO
INSTRUMENT DIVISION
HIGH CHURCH STREET, NEW BASFORD, NOTTINGHAM.
Please send copy of your catalogue **ELECTRONIC & NUCLEONIC INSTRUMENTS**

NAME_____

ADDRESS_____

POSITION _____

ETELCO
INSTRUMENT DIVISION
HIGH CHURCH STREET, NEW BASFORD, NOTTINGHAM
The Authority on Electronic & Nucleonic Counting

ETELCO LIMITED, HEAD OFFICE: 22 LINCOLN'S INN FIELDS, LONDON, W.C.2 Tel: HOLborn 6936

E106A-84A(R)

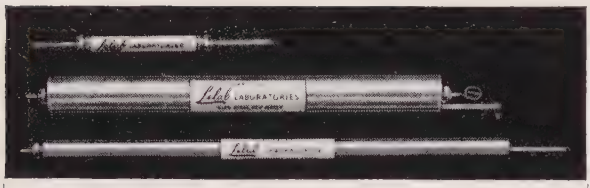

LELAB METAL-WALLED G-M TUBES

for anti-coincidence applications where uniformity counts !

Lelab Counter Tubes are individually constructed, filled, and tested. Each is fabricated almost entirely of metal. All components are confined within the diameter of the tube shell to permit close stacking.

Compare our low prices on these superior tubes!

(Makers of Lelab [Robinson-Selverstone Type] Probe Counters for neurosurgery and where a fine needle-like probe for highly localized measurements is useful.)

Write for complete information

H. W. Leighton Laboratories

York & Sunset Lane-Hatboro, Pa. U.S.A.

MODEL 412 MERCURY RELAY

PRECISION SLIDING PULSER

for Precise Calibration of Single & Multi-Channel Pulse Height Analyzers

Determines Window Widths Using Principle of *Constant Angular Velocity*

AUTOMATICALLY
10 × more accurately
40 × faster than conventional pulsers

Incorporates Both Manual Control and Precision Motor Drive

Simulates Pulses from Scintillation, Proportional or Geiger Counters

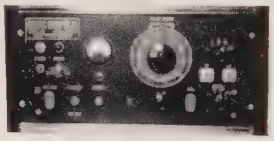

MERCURY PULSER, Model 401

Featuring Versatility and Precision

Specifically designed for the Nuclear Physics Laboratory

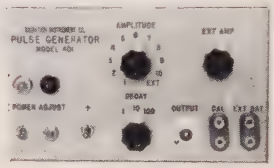

Fast rise and exponential decay simulates scintillation, proportional or geiger counter pulses for test and calibration of amplifiers, pulse height analyzers, scalers, etc.

MODEL 412 . . . $ 450.00 — MODEL 401 . . . $ 125.00

RADIATION INSTRUMENT CO.

P. O. BOX 733, SILVER SPRING, MARYLAND, U.S.A.

NORTH-HOLLAND BOOKS

just out

Internal Conversion Coefficients

by

M. E. ROSE

Chief Physicist, Oak Ridge National Laboratory

9 × 12½″ XXII + 176 pages 40 s.

THE CONTENTS

I INTRODUCTION

1. Definition of the Internal Conversion Process
2. The Selection Rules, Mixtures of Multipoles
3. Theoretical Considerations
4. Method of Calculation and Explanation of the "Tables"

II NUMERICAL RESULTS

K shell Internal Conversion Coefficients; L_I, L_{II}, L_{III}, subshell Internal Conversion Coefficients; Total M shell Internal Conversion Coefficients, $Z \geqslant 65$; M_I, M_{II}, M_{III}, M_{IV}, M_V, subshell Internal Conversion Coefficients, $Z \geqslant 65$; Radial Integrals for K Conversion

Sole Agency for U.S.A.: Interscience Publishers Inc. – New York

NORTH-HOLLAND PUBLISHING COMPANY — AMSTERDAM

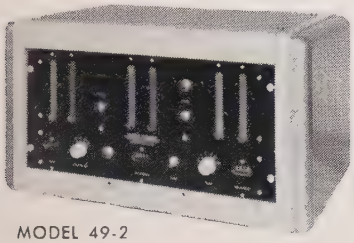
MODEL 49-2

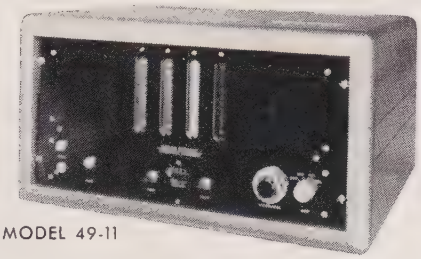
MODEL 49-11

MODEL 49-15

SCALERS

Now – the most complete line of scalers ever offered by any manufacturer. The units shown are just a few of the more than thirty *different* scalers manufactured by RIDL. From conventional vacuum tube units to completely transistorized models – from simple utility scalers to fuliy automated printing scaler systems, these are all STANDARD items, available in most cases from stock.

- **Preset Count Scalers**
- **Preset Time Scalers**
- **Time Scalers**
- **Printing Scalers**
- **Dual Scalers**
- **Triple Scalers**
- **1 Millivolt Sensitivity Scalers**
- **Scalers with High Voltage Supplies**

These are just some of the features available in RIDL Scalers.

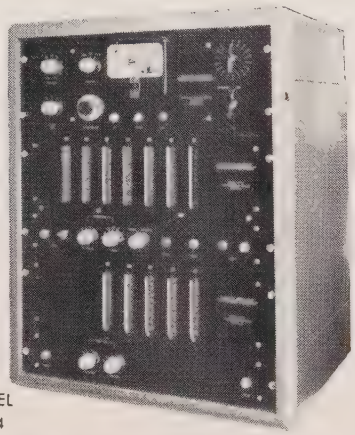
MODEL 49-4

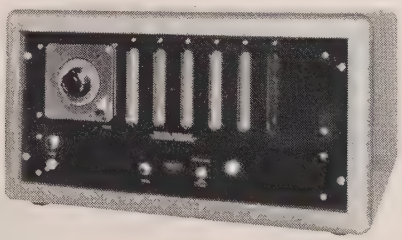
MODEL 49-10

MODEL 49-54

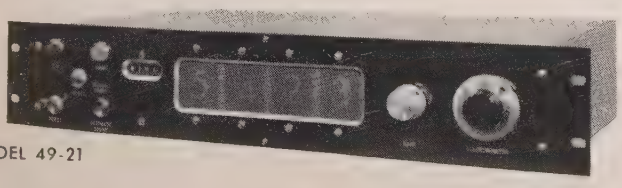
MODEL 49-21

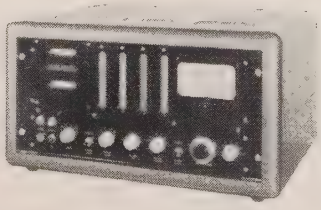
MODEL 49-19

REMEMBER, whatever your scaler requirements may be, RIDL has the solution. Our staff is always available to answer your inquiries. Write today for complete information.

RIDL **Radiation Instrument Development Laboratory, Inc.**

5737 South Halsted Street, Chicago 21, Illinois • TRiangle 3-2345

a Complete Scintillation Service

phosphors and counters

PLASTIC LIQUID & PHOSPHORS

* PLASTIC PHOSPHOR NE 102, light output 65% anthracene, available in all sizes and shapes up to one ton, in thin sheet form, in fine tubes for the construction of scintillation flow counters, or as filaments for the construction of scintillation nuclear track chambers. (Bulletin 11).
* BORON POLYESTER PLASTIC PHOSPHOR NE 400 and NE 401(88% B^{10}) for neutron detection. Standard size from 0.5 to 5.0 inches diameter. (Bulletin 13).
* LOADED LIQUID SCINTILLATORS in bulk or encapsulated, containing Pb for extreme X-ray sensitivity, and Gd, B, Cd, and Sm for neutron detection. (Bulletins 9 and 9a).
* SCINTILLATING GELS for efficient internal counting of suspended materials. (Bulletin 9).
* SCINTILLATION CHEMICALS of highest purity P.B.D., POPOP, T.P.B., p-terphenyl, PPO, D.P.H., alpha-N.P.O., D.M.C., B.B.O., B.P.O., D.P.A., D.P.S., vinyltoluene, styrene, xylene, toluene, methyl borate, phenylcyclohexane, monoisopropylbiphenyl
* LIGHT PIPES of polyvinyltoluene and polystyrene.
* PLASTIC PHOSPHOR SPIRAL FLOW CELL NE 801 for beta and alpha emitters.

Nuclear Enterprises (G.B.) Ltd

NEW LINE OF PRECISION NUCLEAR INSTRUMENTS

* Non-overloading Linear Pulse Amplifier NE 5202 of the Fairstein type (Bulletin 14).
* Pre-Amplifier and Cathode Follower NE 5202A.
* Single Channel Pulse Height Selectors NE 5102 and NE 5103.
* Shielded Scintillation Head Units NE 5501-3.
* Highly Stabilised EHT Supplies NE 5302 (1.8 kV) and NE 5303 (5kV).
* Complete assembly for C14 and tritium counting NE 8301.
* Complete Human Body Counter Installations NE 8101–3.
* Ratemeter NE 5401 with eight ranges and six time constants.
* Scanning scintillation spectrometer NE 8601.

Bankhead Medway,
Sighthill, Edinburgh, 11, Scotland — Tel. CRA 4513

OF SPECIAL NOTE

* SCINTILLATION CRYSTALS by Harshaw. Exclusive concessionaire in Great Britain for NaI(Tl), CsI(Tl), LiI(Eu), and Li^6I(Eu). NaI(Tl) available in sizes up to 9″ diameter x 9″ thick, and down to 0.015″ thick with 0.005″ Be windows for X-ray counting and spectrometry. Resolution with standard sizes 7–8% on Cs^{137} line. CsI(Tl) down to 0.005″ thick for alpha and proton studies. Li^6I(Eu) in special low temperature mounts for fast neutron spectrometry.
* NEW! Photomultiplier-NaI(Tl) combinations with direct coupling of crystal to photomultiplier and giving improved resolution.
* C.D.C. 100-CHANNEL TRANSISTORISED KICK-SORTER at new *low* price for 1959 and with short delivery. Full range of accessories to provide automated assembly.
* MULTI-CHANNEL SCINTILLATION SPECTROMETER NE 8201 for industrial tracer investigations. (Bulletin 15).

Write now for Bulletins and Price List ndh 707

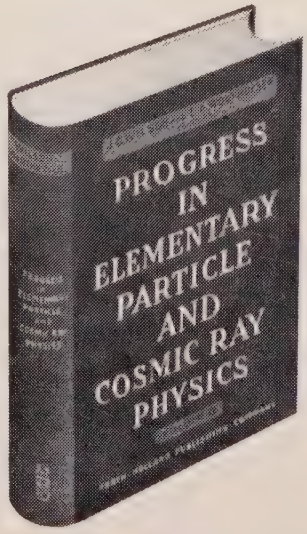

PROGRESS IN ELEMENTARY PARTICLE AND COSMIC RAY PHYSICS VOL. IV

Editors

J. G. WILSON, *Professor of Physics, University of Leeds*

and

S. A. WOUTHUYSEN, *Professor of Physics, University of Amsterdam*

6 × 9″ XII + 482 p. 110 illus. Guilders 45.00 (90 s)

CONTENTS

1. *Some Theoretical Aspects of the Strong Interactions of the New Particles* (B. D'Espagnat and J. Prentki). 2. *The Properties and Production of K-mesons* (W. D. Walker). 3. *The Interaction of μ-Mesons with Matter* (G. N. Fowler and A. W. Wolfendale). 4. *The Primary Cosmic Radiation and its Time Variations* (S. F. Singer). 5. *The Origin of Cosmic Radiation* (V. L. Ginzburg).

Sole Agency for U.S.A.: Interscience Publishers, Inc. — New York

NORTH-HOLLAND PUBLISHING COMPANY - AMSTERDAM

Send your order to your bookseller or directly to us

MARSHALL

PULSE HEIGHT ANALYSER

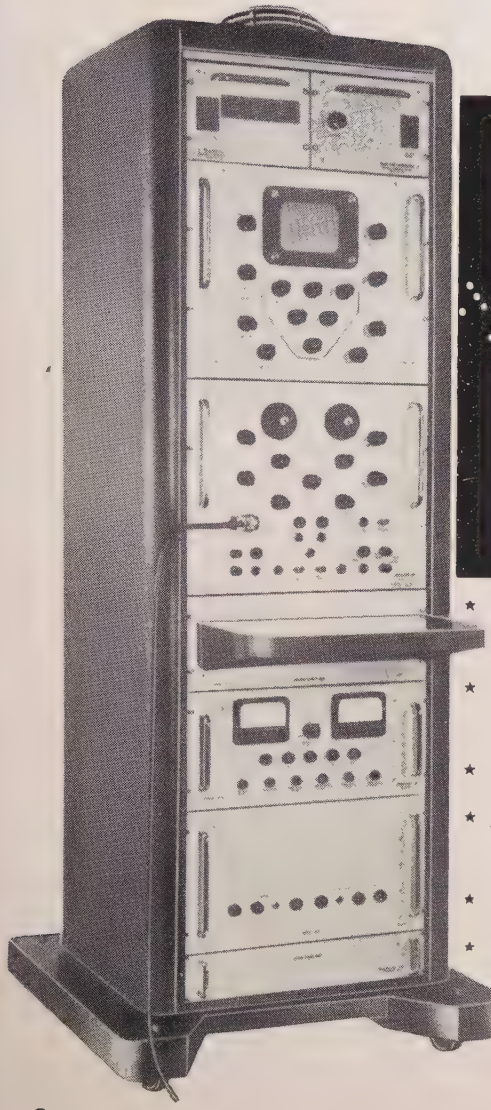

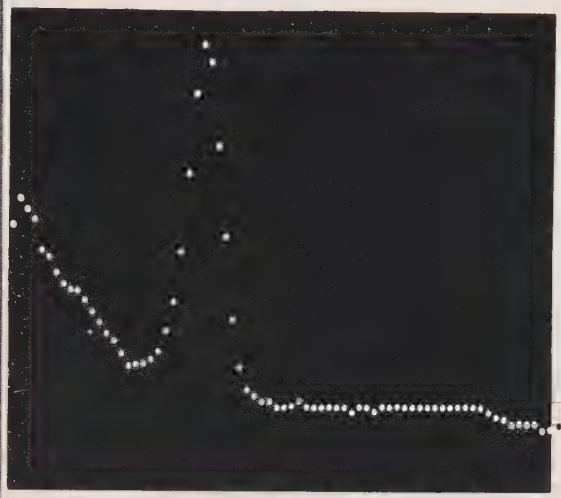

* Torsional delay line data storage with computor reliability.
* Resolution constant or proportional to amplitude.
* Background subtraction.
* Analysis of pulses of either sign from 1 mV to 50 V.
* Binary and decimal storage.
* Both digital and analogue display.

* Storage capacity 2400 digits.
* Analogue readout and automatic printout using either adding machine or electric typewriter.
* High stability and linearity.

* Total count scaler.
* Accurate live time integrator.
* Built-in precision test pulse generator.

MARSHALL
THE AIRPORT CAMBRIDGE, ENGLAND
TELEPHONE: CAMBRIDGE 58291 TELEGRAMS AND CABLES: MARFLY, CAMBRIDGE

Powerful Low-cost

NEUTRON SOURCE

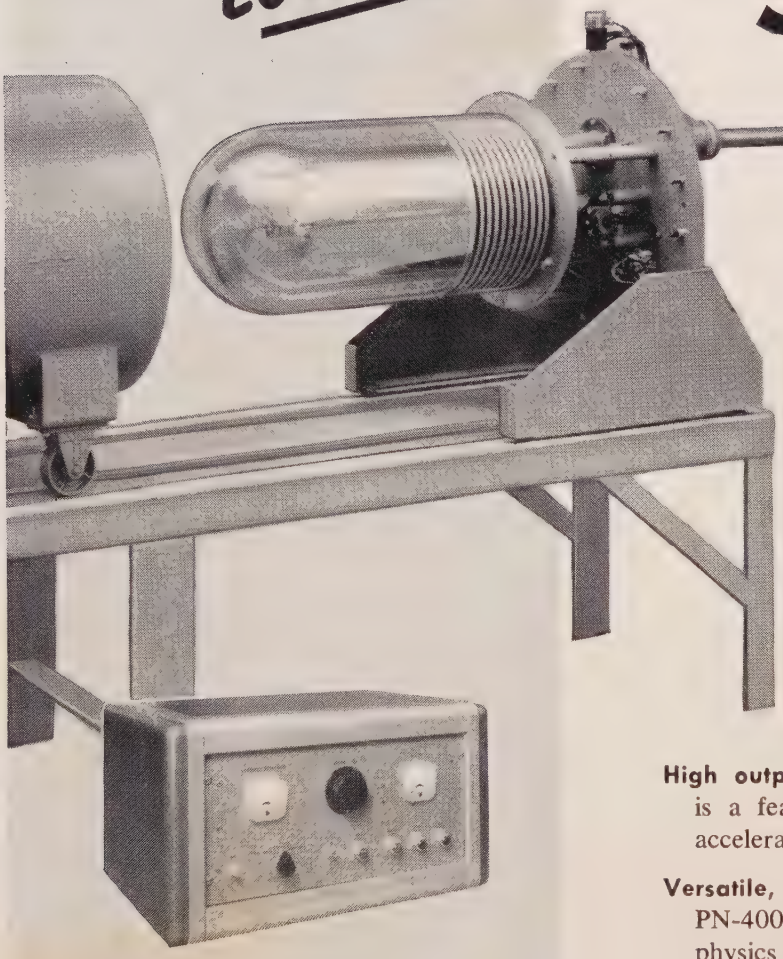

THE MODEL PN-400

400,000-VOLT *Van de Graaff*® POSITIVE-ION ACCELERATOR

yields 10^{10} neutrons per second in continuous operation with new tritium target (D–T reaction).

High output, in pulsed and continuous operation, is a feature of the Model PN-400 positive-ion accelerator.

Versatile, low-cost, and safe in operation, the Model PN-400 is especially useful in teaching nuclear physics and reactor engineering.

Useful applications include: studies of neutron scattering, neutron-induced nuclear reactions, transient and steady-state effects in subcritical reactor assemblies, radiation damage, activation analysis, and biological effects of neutrons.

Advantages

High output
400,000 volts; continuous beam current controllable from 10 to 150 μa; pulsed current, 100 μa.

Small size
111 inches overall, including 48-inch tube extension.

Safety
Entire high-potential system enclosed; target at ground.

Proved design
Based on 12 years experience in building Van de Graaff particle accelerators.

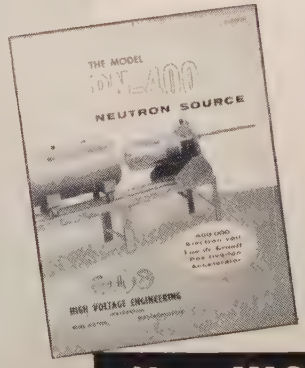

Bulletin PN *gives details of performance.*
Write our Technical Sales Department for your copy.

HIGH VOLTAGE SERVICING CO. LTD.
60 Carpenter's Wood Drive
Chorley Wood
Rickmansworth, Herts, England
Telephone Field End 7431

HIGH VOLTAGE ENGINEERING CORPORATION
BURLINGTON MASSACHUSETTS

NUCLEAR INSTRUMENTS AND METHODS 4 (1959) 53–66; NORTH-HOLLAND PUBLISHING CO.

CALCULATION OF THE *G* FACTOR FOR GAS SCATTERING EXPERIMENTS†

EDWARD A. SILVERSTEIN

University of Wisconsin, Madison, Wisconsin

Received 15 January 1959

In gas scattering experiments a beam traverses the target gas and scattered particles enter the detector through a system consisting of two apertures in parallel planes. The "*G* factor", *G*, relating the yield to the beam intensity, target density, and scattering cross section is calculated for several types of aperture boundaries. (Geometrical effects only are considered; slit edge and multiple scattering are ignored.)

The case of a front aperture composed of two parallel edges of infinite height with a rear (detector) aperture of any shape is calculated up to terms in the fourth derivative of the cross section. Effects of the finite diameter of the beam are also included.

For a circular front and rear aperture the *G* factor involves elliptic integrals. The extra calculation in design of such a system is considered worthwhile, since a pair of circular apertures should be simpler to make and align.

List of Symbols (see figs. 1, 2, 3)

A — $\dfrac{(1-\omega)\,r_2}{r_1}$.

$\mathscr{A}$ — denotes rear aperture. It also stands for the area of the rear aperture.

c, s — $\cos\theta_0$, $\sin\theta_0$.

$d\boldsymbol{A}$ — area element of the rear aperture.

$d\Omega$ — solid angle subtended by an area element of the rear aperture at a point on the beam.

h — distance between front and rear apertures.

n — total number of bombarding particles in the beam.

N — number of target nuclei per unit volume.

r_1, r_2 — radii of the front and rear circular aperture, respectively.

$\boldsymbol{R}$ — vector from the z axis to the rear aperture plane.

$\boldsymbol{R}_0$ — vector along the centerline of the aperture system from the z axis to the rear aperture plane.

Y — the yield of scattered particles collected by the detector aperture system.

z — coordinate along beam axis with origin where $\boldsymbol{R}_0$ intersects beam axis. The positive direction is taken in the direction of the beam.

$\in$ — $1/R_0$.

θ — angle between $\boldsymbol{R}$ and the z axis. This is the actual scattering angle for particles scattered along $\boldsymbol{R}$.

θ_0 — angle between $\boldsymbol{R}_0$ and the z axis.

ξ, η — rectangular coordinates in the rear aperture plane with origin at the termination of $\boldsymbol{R}_0$. The ξ axis is $\perp$ to the scattering plane (plane of $\boldsymbol{R}_0$ and the z axis) while the η axis lies in it.

ξ', η' — coordinate system in front aperture plane parallel to ξ, η system.

$\boldsymbol{\xi}, \boldsymbol{\eta}, \mathbf{z}$ — unit vectors associated with $\boldsymbol{\xi}$, $\boldsymbol{\eta}$, and z axes.

ξ'_b, η'_b — values of ξ' and η' on the boundary of the front aperture.

σ' — $[d\sigma(\theta)/d\theta]_{\theta_0}$. Similarly $\sigma^{(n)}$ is the n-th derivative of σ at θ_0. $\sigma^{(0)} = \sigma$.

$\sigma(\theta)$ — differential scattering cross section at θ. (We assume that the cross section is independent of the azimuthal angle.) $\sigma(\theta_0) = \sigma$.

ω — h/R_0.

† Work supported by the U.S. Atomic Energy Commission and by the Graduate School from funds supplied by the Wisconsin Alumni Research Foundation.

1. Introduction

In nuclear scattering experiments with gas targets, particles scattered from an incident beam, or reaction products, enter a detector through a system consisting of two defining apertures (see fig. 1). These determine the target thickness, the yield, and the angular resolution of the system.

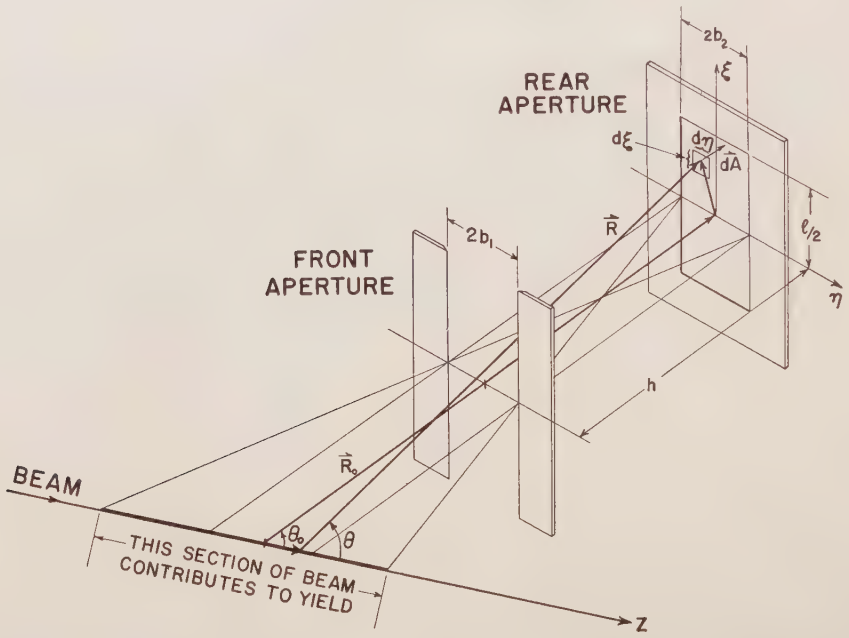

Fig. 1. Schematic diagram showing the case of a vertical front slit and rectangular rear aperture. The vector diagram, however, applies to all cases. It shows the geometric relations between a point on the beam axis from which scattered particles originate,and an area element $d\xi\, d\eta$ of the rear aperture, through which they pass after being scattered through an angle θ.

The yield in such an arrangement is given by

$$Y = \frac{nNG\sigma}{\sin\theta_0}. \qquad (1)$$

When G is known, we can express σ in terms of n, N, and Y which are experimentally determined. The factor G will depend on the particular geometry of the detecting system and on the derivatives of the cross section with respect to angle, since the effect of the variation of cross section over the small angular range accepted by the rear aperture cannot always be neglected. The present calculations were initiated by the design of a new scattering chamber, which required a detailed consideration of the G factor. In attempting to reproduce earlier results[1]) an error (apparently due to neglect of certain second order terms) in the cross section independent part of G was discovered. Since accurate ($\approx 0.1\%$) p–p scattering cross section data[2]) were currently being obtained in this laboratory it was felt worthwhile to redo the G factor calculations.

Furthermore, use of the correct G factor expressions increased the magnitude of inconsistencies† in the p–p data taken with different size slits. Higher derivative terms in the cross section were therefore investigated and are here reported. While carrying out the above calculations, it appeared feasible to treat also the case of the circular front aperture.

The types of aperture boundaries treated here are: a front aperture composed of two parallel

† The inconsistencies were subsequently attributed to errors in slit size measurement and beam current integration[2]).

[1]) Breit, Thaxton and Eisenbud, Phys. Rev. **55** (1939) 1018.

[2]) David J. Knecht, S. Messelt, E. D. Berners and L. C. Northcliffe, to be published in the Phys. Rev.

edges of infinite height (hereafter referred to as a vertical front slit) with a rear aperture of arbitrary shape (see fig. 1); a circular front and rear aperture (see fig. 2).

It is more difficult to calculate G for the case of a circular front and rear aperture than for the other geometries treated here. However, a system of this kind has several experimental

$$d\Omega = \frac{\boldsymbol{R}\cdot d\boldsymbol{A}}{R^3} = \frac{\boldsymbol{R}\cdot\boldsymbol{R}_0}{R^3 R_0}\, d\xi d\eta .$$

We define $\mathscr{I}$ by

$$\frac{\mathscr{I}}{R_0^2} = \frac{\boldsymbol{R}\cdot\boldsymbol{R}_0}{R^3 R_0}, \tag{2.2}$$

and (2.1) becomes

$$d^3Y = nN\sigma(\theta)\frac{\mathscr{I}}{R_0^2}\, d\xi d\eta dz . \tag{2.3}$$

To find Y, we take for each element of rear

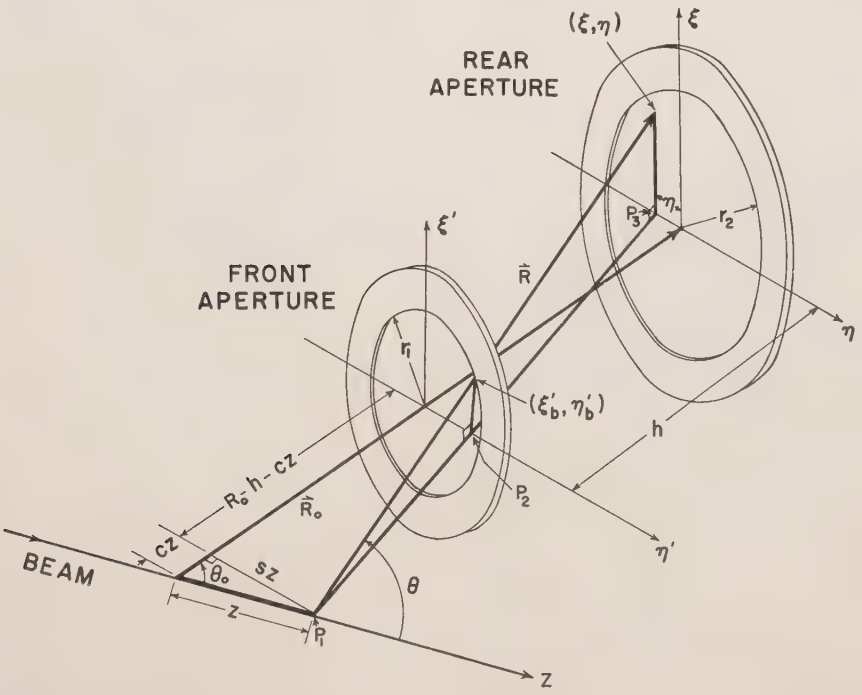

Fig. 2. Schematic diagram showing the case of circular front and rear apertures. The heavy lines show the geometric relations between a point (ξ,η) in the rear aperture plane and the endpoint P_1 of that part of the beam which can contribute scattered particles to an area element at the point (ξ,η).

advantages; is is much easier to machine and align accurately, and in certain types of scattering chambers the fact that it possesses rotational symmetry about the centerline will simplify mechanical construction.

No account is taken here of effects due to slit edge or multiple scattering.

2. General Expression for G for a Line Beam

By a line beam we mean that we neglect effects arising from the finite diameter of a real beam. In this limiting case we have

$$d^3Y = nN\sigma(\theta)d\Omega dz , \tag{2.1}$$

following immediately from the definition of $\sigma(\theta)$, with

aperture area, $d\xi d\eta$, the contribution from the total length of beam seen by that element, i.e., we first integrate over z. Since the length of beam visible from a point on the rear aperture depends in general on ξ and η, we denote the upper and lower limits respectively by $z_2(\xi,\eta)$ and $z_1(\xi,\eta)$. These will be written z_2 and z_1. (Hereafter we will not indicate functional dependence of quantities unless necessary for clarity or emphasis.) Integration of (2.3) over the rear aperture gives

$$Y = \frac{nN}{R_0^2}\iint_{\mathscr{A}} d\xi d\eta \int_{z_1}^{z_2} \mathscr{I}\sigma(\theta)dz . \tag{2.4}$$

In order to take into account the dependence

of the cross section on angle, we expand $\sigma(\theta)$ in a power series in $\Delta\theta = \theta - \theta_0$ giving

$$\sigma(\theta) = \sigma \sum_{n=0}^{\infty} \frac{1}{n!} \frac{\sigma^{(n)}}{\sigma} (\Delta\theta)^n . \tag{2.5}$$

Replacing $\sigma(\theta)$ in (2.4) by its expansion and using (1) we obtain:

$$G = \frac{s}{R_0^2} \iint_{\mathscr{A}} \mathrm{d}\xi \mathrm{d}\eta \int_{z_1}^{z_2} \mathrm{d}z \, \mathscr{J} \left[\sum_{n=0}^{\infty} \frac{1}{n!} \frac{\sigma^{(n)}}{\sigma} (\Delta\theta)^n \right] . \tag{2.6}$$

We write this as

$$G = \sum_{n=0}^{\infty} G_n , \qquad \text{where} \tag{2.7}$$

$$G_n = \frac{\sigma^{(n)}}{\sigma} \frac{1}{n!} \frac{s}{R_0^2} \iint_{\mathscr{A}} \mathrm{d}\xi \mathrm{d}\eta \int_{z_1}^{z_2} \mathscr{J} (\Delta\theta)^n \mathrm{d}z . \tag{2.8}$$

The expressions which we will obtain below for a line beam will suffice for most uses. If we wish to consider the effects of finite beam diameter, we can do so by averaging over a suitable set of line beam forming the elements of the actual beam. This is done in section 6 for a non-divergent beam. In ref.[3]) the case of a diverging beam is treated. This treatment reduces to ours in the limit of a non-diverging beam.

In the next section we find expressions for $\Delta\theta$ and $\mathscr{J}$ by expansion in powers of $1/R_0$. These expressions apply to any geometry. A particular geometry is described by z_1, z_2, and $\mathscr{A}$. These will be discussed in each case.

3. Calculation of $\mathscr{J}$ and $\Delta\Theta$

From fig. 1 we see that

$$\boldsymbol{R}_0 + \xi \boldsymbol{\xi} + \eta \boldsymbol{\eta} - \boldsymbol{R} - z \mathbf{z} = 0 . \tag{3.1}$$

The relations below follow immediately from the geometry:

$$\boldsymbol{R}_0 \cdot \boldsymbol{\xi} = 0 , \tag{3.2}$$

$$\boldsymbol{R}_0 \cdot \boldsymbol{\eta} = 0 , \tag{3.3}$$

$$\boldsymbol{\xi} \cdot \mathbf{z} = 0 , \tag{3.4}$$

$$\boldsymbol{R}_0 \cdot \mathbf{z} = R_0 c , \tag{3.5}$$

$$\boldsymbol{\eta} \cdot \mathbf{z} = s . \tag{3.6}$$

Relations (3.1) through (3.6) will suffice to calculate $\mathscr{J}$ and $\Delta\theta$.

From (3.1) we have

$$\boldsymbol{R} = \boldsymbol{R}_0 + \xi \boldsymbol{\xi} + \eta \boldsymbol{\eta} - z \mathbf{z} .$$

[3]) Critchfield and Dodder, Phys. Rev. **75** (1949) 419.

Squaring both sides and using (3.2)–(3.6) we get

$$R^2 = R_0^2 + \xi^2 + \eta^2 + z^2 - 2cR_0 z - 2s\eta z . \tag{3.7}$$

We take the scaler product of $\boldsymbol{R}_0$ and (3.1) and with the use of (3.2)–(3.6) obtain:

$$\boldsymbol{R}_0 \cdot \boldsymbol{R} = R_0^2 - cR_0 z . \tag{3.8}$$

We set $\epsilon = 1/R_0$ and (2.2) becomes

$$\mathscr{J} = \frac{[1 - cz\epsilon]}{[1 - 2cz\epsilon + \xi^2\epsilon^2 + \eta^2\epsilon^2 + z^2\epsilon^2 - 2s\eta z\epsilon^2]^{\frac{3}{2}}} . \tag{3.9}$$

The expansion to second order in ϵ follows immediately:

$$\mathscr{J} = 1 + 2cz\epsilon + \tfrac{3}{2}(3c^2 - 1) z^2\epsilon^2 + 3s\eta z\epsilon^2 - \tfrac{3}{2} \xi^2\epsilon^2 - \tfrac{3}{2} \eta^2\epsilon^2 . \tag{3.10}$$

We now calculate $\Delta\theta$. By definition of θ we have

$$\cos\theta = \cos(\theta_0 + \Delta\theta) = \frac{\boldsymbol{R} \cdot \mathbf{z}}{R} . \tag{3.11}$$

Taking the scaler product of $\mathbf{z}$ and (3.1) and using (3.2)–(3.6) we get

$$\cos(\theta_0 + \Delta\theta) = \frac{cR_0 + s\eta - z}{R} . \tag{3.12}$$

Use of the cosine addition formula on (3.11) gives

$$c \cos\Delta\theta - s \sin\Delta\theta = \frac{\boldsymbol{R} \cdot \mathbf{z}}{R} . \tag{3.13}$$

Since $\sin\Delta\theta = \Delta\theta - \frac{1}{3}(\Delta\theta)^3 + \cdots$, we can put $\sin\Delta\theta = \Delta\theta$ without affecting second order terms. However, we must take $\cos\Delta\theta = 1 - \frac{1}{2}(\Delta\theta)^2$. We set $\Delta\theta = \alpha\epsilon + \beta\epsilon^2$ and (3.13) becomes

$$c[1 - \tfrac{1}{2}(\alpha\epsilon + \beta\epsilon^2)^2] - s(\alpha\epsilon + \beta\epsilon^2) = \left[\frac{\boldsymbol{R} \cdot \mathbf{z}}{R}\right]_{\text{to second order}} . \tag{3.14}$$

Expansion of (3.12) in powers of ϵ gives

$$\left[\frac{\boldsymbol{R} \cdot \mathbf{z}}{R}\right]_{\text{to second order}} = c - s^2 z\epsilon + s\eta\epsilon - \tfrac{3}{2} s^2 c z^2 \epsilon^2 + 2sc\eta z\epsilon^2 - \tfrac{1}{2} c\eta^2\epsilon^2 - \tfrac{1}{2} c\xi^2\epsilon^2 . \tag{3.15}$$

By equating coefficients of ϵ and ϵ^2 in (3.14) and (3.15) we find that

$$\alpha = sz - \eta$$

and

$$\beta = scz^2 - cz\eta + \tfrac{1}{2}\frac{c}{s}\xi^2 .$$

Then to second order in ϵ we have

$$\Delta\theta = (sz - \eta)\epsilon + \left(scz^2 - cz\eta + \tfrac{1}{2}\frac{c}{s}\xi^2\right)\epsilon^2 . \tag{3.16}$$

4. Calculation of the Limits of Integration, z_1 and z_2

4a. VERTICAL FRONT SLIT

It is apparent in this case (see fig. 1) that z_1 and z_2 are independent of ξ.

The following equation holds for the projection of **R** on the (η,z) plane (see fig. 2):

$$\frac{\eta'_b - \eta}{h} = \frac{sz - \eta}{R_0 - cz}. \tag{4a.1}$$

Solving for z, we get

$$z = \frac{R_0\eta'_b - \eta(R_0 - h)}{sh - c(\eta - \eta'_b)}. \tag{4a.2}$$

The limits z_1 and z_2 are obtained by setting $\eta'_b = -b_1$ and $\eta'_b = b_1$ respectively. We also set $h/R_0 = \omega$ and obtain

$$z_1 = -\frac{R_0 b_1}{hs}\frac{\left[1 + (1-\omega)\frac{\eta}{b_1}\right]}{\left[1 - \frac{c}{s}\frac{1}{\omega}(\eta + b_1)\epsilon\right]} \tag{4a.3}$$

and

$$z_2 = \frac{R_0 b_1}{hs}\frac{\left[1 - (1-\omega)\frac{\eta}{b_1}\right]}{\left[1 - \frac{c}{s}\frac{1}{\omega}(\eta - b_1)\epsilon\right]}. \tag{4a.4}$$

We must have $$\frac{\epsilon}{\omega}\left|\frac{c}{s}\right|(b_1 + b_2) < 1 \tag{4a.5}$$

in order for z_1 and z_2 to be finite, that is, for the rear aperture to view a finite length of beam.

4b. CIRCULAR FRONT APERTURE

On the boundary of the front aperture (see fig. 2)

$$(\xi'_b)^2 + (\eta'_b)^2 = r_1^2. \tag{4b.1}$$

From the similarity of the triangle formed by ξ'_b and the line P_1P_2 (see fig. 2) to that formed by ξ and the line P_1P_3 we obtain

$$\frac{(\xi'_b)^2}{\xi^2} = \frac{(sz - \eta'_b)^2 + (R_0 - h - cz)^2}{(R_0 - cz)^2 + (sz - \eta)^2}. \tag{4b.2}$$

We use (4b.1) to eliminate ξ'_b. We then use (4a.1) and (4b.2) to eliminate η'_b, thus obtaining a quadratic equation for z having the solution

$$z = \frac{R_0 r_1}{hs}\left\{\frac{\left[\frac{c}{s}\frac{(1-\omega)}{\omega}\frac{(\eta^2+\xi^2)}{r_1}\epsilon - \frac{c}{s}\frac{r_1}{\omega}\epsilon - (1-\omega)\frac{\eta}{r_1}\right] \pm \sqrt{1 - (1-\omega)^2\frac{\xi^2}{r_1^2} - 2\frac{c}{s}\eta\epsilon + \frac{c^2}{s^2}(\eta^2+\xi^2)\epsilon^2}}{\left[1 - 2\frac{c}{s}\frac{\eta}{\omega}\epsilon - \frac{c^2}{s^2}\frac{r_1^2}{\omega^2}\epsilon^2 + \frac{c^2}{s^2}\frac{(\eta^2+\xi^2)}{\omega^2}\epsilon^2\right]}\right\}. \tag{4b.3}$$

(The minus sign corresponds to z_1, the plus to z_2.)

The condition for viewing a finite beam length is obtained by evaluating the denominator at $\xi = 0$, where the rear aperture is widest. We obtain:

$$\frac{\epsilon}{\omega}\left|\frac{c}{s}\right|(r_1 + r_2) < 1. \tag{4b.4}$$

The quantity in (4b.3) under the square root sign must of course be non-negative. It is easily shown that this is so when the quantity

$$A = \frac{(1-\omega)r_2}{r_1}$$

satisfies

$$A < 1. \tag{4b.5}$$

From simple geometry it is also evident that this condition insures that every point on the rear aperture can see at least some part of the beam (in fact, a segment containing $z = 0$). The quantity A is the modulus of the complete elliptic integrals $E(A)$ and $K(A)$ occurring in the expressions for G in section 8, and (4b.5) is necessary for the validity of these expressions. If $A > 1$, we cannot keep the expression under the square root sign non-negative without violating (4b.4), i.e., without viewing an infinite length of the beam.

5. Calculation of G for Vertical Front Slit

5a. GENERAL CONSIDERATIONS

We change the z variable in our expression (2.8) for G_n by setting

$$t = \left[\frac{R_0 b_1}{hs}\right]^{-1} z \tag{5a.1}$$

so that (2.8) becomes

$$G_n = \frac{\sigma^{(n)}}{\sigma}\frac{1}{n!}\frac{b_1}{R_0 h}\iint_{\mathscr{A}} d\xi d\eta \int_{g_1(\epsilon)}^{g_2(\epsilon)} (\Delta\theta)^n \mathscr{I}(\epsilon,t)dt \tag{5a.2}$$

where $$g_1(\epsilon) = \left[\frac{R_0 b_1}{hs}\right]^{-1} z_1 \tag{5a.3}$$

and $$g_2(\epsilon) = \left[\frac{R_0 b_1}{hs}\right]^{-1} z_2. \tag{5a.4}$$

The use of (5a.1) in (3.10) and (3.16) gives

$$\mathscr{J}(\epsilon,t) = 1 + 2\frac{c}{s}\frac{b_1 t}{\omega}\epsilon + \tfrac{3}{2}\left(2\frac{c^2}{s^2} - 1\right)\frac{b_1^2 t^2}{\omega^2}\epsilon^2 + \\ + \frac{3b_1\eta t}{\omega}\epsilon^2 - \tfrac{3}{2}\xi^2\epsilon^2 - \tfrac{3}{2}\eta^2\epsilon^2 \qquad (5a.5)$$

and

$$\Delta\theta = \frac{b_1 t}{\omega}\epsilon - \eta\epsilon + \frac{c}{s}\frac{b_1^2 t^2}{\omega^2}\epsilon^2 - \frac{c}{s}\frac{b_1\eta t}{\omega}\epsilon^2 + \tfrac{1}{2}\frac{c}{s}\xi^2\epsilon^2 . \qquad (5a.6)$$

We define $I_n(\epsilon)$ by

$$I_n(\epsilon) = \int_{g_1(\epsilon)}^{g_2(\epsilon)} (\Delta\theta)^n \mathscr{J}(\epsilon,t)\,dt \qquad (5a.7)$$

and $< f(\xi,\eta) >$, where $f(\xi,\eta)$ is any function, by

$$< f(\xi,\eta) > = \frac{1}{\mathscr{A}}\iint_{\mathscr{A}} f(\xi,\eta)\,d\xi\,d\eta . \qquad (5a.8)$$

With these definitions, (5a.2) becomes

$$G_n = \frac{\sigma^{(n)}}{\sigma}\frac{1}{n!}\frac{\mathscr{A}b_1}{R_0 h} < I_n(\epsilon) > . \qquad (5a.9)$$

We will calculate G_n by expansion of $I_n(\epsilon)$ in powers of ϵ about $\epsilon = 0$, i.e.,

$$I_n(\epsilon) = I_n(0) + I_n^{(1)}(0)\epsilon + \tfrac{1}{2} I_n^{(2)}(0)\epsilon^2 + \cdots , \qquad (5a.10)$$

where $$I_n^{(m)}(0) = \left[\frac{\partial^m I_n(\epsilon)}{\partial\epsilon^m}\right]_{\epsilon=0} .$$

We can also express G in the form

$$G = G_{00}\left[1 + \Delta_0 + \frac{\sigma^{(1)}}{\sigma}\Delta_1 + \frac{\sigma^{(2)}}{\sigma}\Delta_2 + \cdots\right], \qquad (5a.11)$$

where $$G_{00} = \frac{2\mathscr{A}b_1}{R_0 h} \qquad (5a.12)$$

and $$\Delta_n = \frac{1}{n!}\tfrac{1}{2} < I_n(\epsilon) > - \delta_{0n} . \qquad (5a.13)$$

The factor 2 arises in (5a.12) because $I_0(0) = 2$, and δ_{0n} is the Kronecker delta ($\delta_{00} = 1$, $\delta_{0n} = 0$ for $n \neq 0$).

We note that as the rear aperture is moved farther from the beam ($\epsilon \to 0$) and ω is held constant, (ω will have a finite value < 1 even in the limiting case for any reasonable aperture system) the G factor will approach G_{00}, which can be thought of as an uncorrected G factor. The Δ_n represent the "poorness" of the geometry. All $\Delta_n \to 0$ as $\epsilon \to 0$ which is why ϵ is a good expansion parameter. We will find below that it is sufficient to take Δ_0, Δ_1, and Δ_2 to second order in ϵ, but that Δ_3 and Δ_4 must be taken to fourth order. By comparing Δ_0, $[(\sigma^{(1)}/\sigma)\Delta_1]$, etc. with the "1" in (5a.11) we can decide whether we have taken enough terms. For very "poor" geometry, (large apertures close to beam) we could conceivably need Δ_0, etc. to higher than second order in ϵ. Similarly, the value of $\sigma^{(n)}/\sigma$ and Δ_n indicates whether or not the corresponding Δ_n must be calculated.

5b. CALCULATION OF Δ_0 to Δ_4

We will show the calculation of Δ_0 in detail. From (5a.7) we have

$$I_0(\epsilon) = \int_{g_1(\epsilon)}^{g_2(\epsilon)} \mathscr{J}(\epsilon,t)\,dt .$$

Putting in (5a.5) and integrating we get

$$I_0(\epsilon) = [g_2 - g_1] + \frac{c}{s}\frac{b_1}{\omega}[g_2^2 - g_1^2]\epsilon + \tfrac{1}{2}\left(2\frac{c^2}{s^2} - 1\right)\frac{b_1^2}{\omega^2}[g_2^3 - g_1^3]\epsilon^2 + \\ + \tfrac{3}{2}\frac{b_1\eta}{\omega}[g_2^2 - g_1^2]\epsilon^2 - \tfrac{3}{2}(\xi^2 + \eta^2)[g_2 - g_1]\epsilon^2 . \qquad (5b.1)$$

Then $$I_0(0) = [(g_2 - g_1)]_0 , \qquad (5b.2)$$

$$I_0^{(1)}(0) = [g'_2 - g'_1]_0 + \frac{c}{s}\frac{b_1}{\omega}[g_2^2 - g_1^2]_0 , \qquad (5b.3)$$

and $$I_0^{(2)} = [g''_2 - g''_1]_0 + 4\frac{c}{s}\frac{b_1}{\omega}[g_2 g'_2 - g_1 g'_1]_0 + \left(2\frac{c^2}{s^2} - 1\right)\frac{b_1^2}{\omega^2}[g_2^3 - g_1^3]_0 + \\ + \frac{3b_1\eta}{\omega}[g_2^2 - g_1^2]_0 - 3(\xi^2 + \eta^2)[g_2 - g_1]_0 . \qquad (5b.4)$$

The quantity $$[g'_2 - g'_1]_0 = \left[\frac{\partial g_2}{\partial \epsilon} - \frac{\partial g_1}{\partial \epsilon}\right]_{\epsilon=0}, \text{ etc.}$$

The expressions $[g_2 - g_1]_0$ etc. are obtained in a straightforward manner from (5a.3) and (5a.4) and are listed in appendix A. Substitution of these into (5b.2)–(5b.4), and use of (5a.10) gives

$$I_0(\epsilon) = 2 + 2\frac{c}{s}\eta\epsilon - \frac{b_1^2}{\omega^2}\epsilon^2 + \left[2\frac{c^2}{s^2} - \frac{3}{\omega^2}\right]\eta^2\epsilon^2 - 3\xi^2\epsilon^2 . \tag{5b.5}$$

Then, from (5a.13)

$$\Delta_0 = \frac{c}{s}<\eta>\epsilon - \tfrac{1}{2}\frac{b_1^2}{\omega^2}\epsilon^2 + \left[\frac{c^2}{s^2} - \tfrac{3}{2}\frac{1}{\omega^2}\right]<\eta^2>\epsilon^2 - \tfrac{3}{2}<\xi^2>\epsilon^2 . \tag{5b.6}$$

We list in appendix B all quantities used to calculate Δ_1 to Δ_4. The calculation proceeds exactly as above giving

$$\Delta_1 = -\frac{1}{\omega}<\eta>\epsilon + \frac{c}{s}\left[\tfrac{1}{2}<\xi^2> - \frac{1}{\omega}<\eta^2>\right]\epsilon^2 , \tag{5b.7}$$

$$\Delta_2 = \frac{1}{6\omega^2}\left\{b_1^2 + 3<\eta^2>\right\}\epsilon^2 , \tag{5b.8}$$

$$\Delta_3 = \tfrac{1}{6}\left\{-\frac{1}{\omega^3}\left[<\eta^3> + b_1^2<\eta>\right]\epsilon^3 + \frac{c}{s}\left[-\frac{1}{\omega^3}\left(<\eta^4> + b_1^2<\eta^2>\right) + \frac{1}{2\omega^2}\left(b_1^2<\xi^2> + 3<\eta^2\xi^2>\right)\right]\epsilon^4\right\} \tag{5b.9}$$

and $$\Delta_4 = \frac{1}{24}\frac{1}{\omega^4}\left\{<\eta^4> + 2b_1^2<\eta^2> + \tfrac{1}{5}b_1^4\right\}\epsilon^4 . \tag{5b.10}$$

We note in the above expressions that all terms containing odd powers of ϵ also contain odd powers of η or ξ and thus vanish for a rear aperture symmetric about the η and ξ axes. In general all terms containing odd powers of ϵ vanish for such a rear aperture. We can see this by noting that expression (5a.7) for $I_n(\epsilon)$ remains the same when we replace b_1 by $-b_1$ and t by $-t$. $\mathscr{I}$ and $\Delta\theta$ remain the same, but (4a.3) and (4a.4) give $g_1 \to g_2$ and $g_2 \to g_1$. Thus

$$I_n(\epsilon) \to \int_{g_2}^{g_1}(\Delta\theta)^n\mathscr{I}\,\mathrm{d}(-t) = \int_{g_1}^{g_2}(\Delta\theta)^n\mathscr{I}\,\mathrm{d}t$$

and I_n is unaffected. Then when $I_n(\epsilon)$ is expanded in powers of ϵ it can contain only even powers of b_1. Each term in any Δ_n will then be a dimensionless product of the form

$$b_1^{2v}<\xi^p\eta^q>\epsilon^m .$$

Then if m is odd, p or q must be odd and the average will vanish for a symmetric aperture. In particular, this means that for a symmetric rear aperture our expressions for Δ_0, Δ_1 and Δ_2 are correct to third order in ϵ, while those for Δ_3 and Δ_4 are correct to fifth order.

5c. SPECIAL REAR APERTURE SHAPES

(i) *Rectangular Rear Aperture*

For a rectangular rear aperture (see fig. 1) of halfwidth b_2 and height l, the averages (5a.8) become ($\mathscr{A} = 2b_2l$)

$$<\eta> = 0 \qquad <\eta^3> = 0$$
$$<\eta^2> = \tfrac{1}{3}b_2^2 \qquad <\xi^2> = \tfrac{1}{12}l^2$$
$$<\eta^2\xi^2> = \tfrac{1}{36}b_2^2l^2 \qquad <\eta^4> = \tfrac{1}{5}b_2^4 .$$

The use of the above expressions in (5a.12), (5b.6)–(5b.10) gives

$$G_{00} = \frac{4b_1b_2l}{R_0h}, \tag{5c.1}$$

$$\Delta_0 = \tfrac{1}{3}\frac{c^2}{s^2}\frac{b_2^2}{R_0^2} - \frac{1}{2h^2}(b_1^2 + b_2^2) - \tfrac{1}{8}\frac{l^2}{R_0^2} \tag{5c.2}$$

$$\Delta_1 = \tfrac{1}{3}\frac{c}{s}\left\{\frac{l^2}{8R_0^2} - \frac{b_2^2}{R_0h}\right\} \tag{5c.3}$$

$$\Delta_2 = \tfrac{1}{6}\frac{(b_1^2 + b_2^2)}{h^2} \tag{5c.4}$$

$$\Delta_3 = \tfrac{1}{6}\frac{c}{s}\left\{\frac{l^2}{24R_0^2h^2}(b_1^2 + b_2^2) - \frac{1}{R_0h^3}(\tfrac{1}{5}b_2^4 + \tfrac{1}{3}b_1^2b_2^2)\right\} \tag{5c.5}$$

$$\Delta_4 = \tfrac{1}{24}\frac{1}{h^4}\left\{\tfrac{1}{5}(b_1^4 + b_2^4) + \tfrac{2}{3}b_1^2b_2^2\right\}. \tag{5c.6}$$

(ii) *Circular Rear Aperture*

For a circular rear aperture of radius a, the averages (5a.8) become ($\mathscr{A} = \pi a^2$)

$$<\eta> = <\eta^3> = 0 \qquad <\eta^2> = <\xi^2 < = \tfrac{1}{4}a^2$$

$$<\eta^2\xi^2> = \tfrac{1}{24}a^4, \qquad <\eta^4> = \tfrac{1}{8}a^4.$$

We then obtain

$$G_{00} = \frac{2\pi a^2 b_1}{R_0h} \tag{5c.7}$$

$$\Delta_0 = \tfrac{1}{4}\frac{c^2}{s^2}\frac{a^2}{R_0^2} - \tfrac{1}{2}\frac{1}{h^2}(b_1^2 + \tfrac{3}{4}a^2) - \tfrac{3}{8}\frac{a^2}{R_0^2} \tag{5c.8}$$

$$\Delta_1 = \tfrac{1}{4}\frac{c}{s}\left\{\frac{a^2}{2R_0^2} - \frac{a^2}{R_0h}\right\} \tag{5c.9}$$

$$\Delta_2 = \tfrac{1}{6}\frac{(b_1^2 + \tfrac{3}{4}a^2)}{h^2} \tag{5c.10}$$

$$\Delta_3 = \tfrac{1}{24}\frac{c}{s}\left\{\frac{1}{R_0^2h^2}(\tfrac{1}{2}b_1^2a^2 + \tfrac{1}{4}a^4) - \frac{1}{R_0h^3}(\tfrac{1}{2}a^4 + b_1^2a^2)\right\} \tag{5c.11}$$

$$\Delta_4 = \tfrac{1}{24}\frac{1}{h^4}(\tfrac{1}{8}a^4 + \tfrac{1}{2}b_1^2a^2 + \tfrac{1}{5}b_1^4). \tag{5c.12}$$

6. Finite Beam Diameter Corrections

Finite beam corrections to G are derived below for the case of the vertical front slit treated in section 5. These corrections are not discussed for the circular front aperture case.

We consider the beam to be a cylinder of diameter D with the z axis as axis. We will average over the line beams that form this cylinder, giving each line beam the same weight, i.e., we assume the beam density is uniform.

A particular line beam will be described by the cylindrical coordinates q and γ (see fig. 3). We define $G(q,\gamma)$ as the value of G for the line beam described by q and γ. For this beam, $G(q,\gamma)$ is given by the usual expressions (5a.11) and (5b.6)–(5b.10) with two changes:

From fig. 3 we see that R_0 is replaced by

$$R_0(q,\gamma) = R_0\left(1 - \frac{1}{s}\frac{q}{R_0}\sin\gamma\right), \tag{6.1}$$

i.e., $R_0(q,\gamma)$ is a new, "effective" value of R_0.

With this new R_0 ,the rear aperture appears to be lower by $q\cos\gamma$, i.e.,

$$\xi(q,\gamma) = \xi - q\cos\gamma\,. \tag{6.2}$$

Then

$$<\xi^2(q,\gamma)> = <\xi^2> - 2q\cos\gamma<\xi> + q^2\cos^2\gamma\,. \tag{6.3}$$

All other quantities remain the same, i.e., $h(q,\gamma) = h$ and $\eta(q,\gamma) = \eta$, etc. as is immediately apparent.

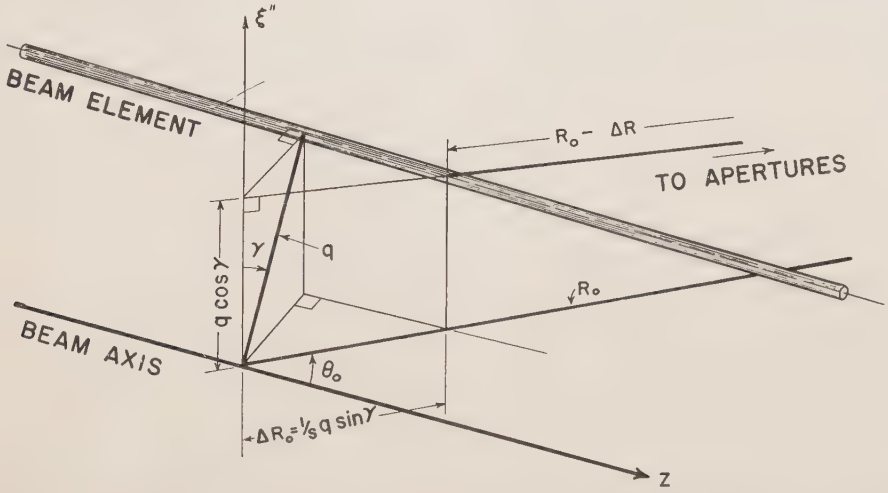

Fig. 3. The effects of finite beam diameter are treated by averaging over the beam elements shown in the figure, each of which is located by the cylindrical coordinates q and γ. To each such beam element the rear aperture appears to be closer by ΔR and lower by $q\cos\gamma$. These considerations apply only to the case of the vertical front slit.

We defined $f(q,\gamma)$ as

$$f(q,\gamma) = \left(1 - \frac{1}{s}\frac{q}{R_0}\sin\gamma\right)^{-1}, \tag{6.4}$$

so that

$$\frac{1}{R_0(q,\gamma)} = \frac{1}{R_0}f(q,\gamma)\,, \tag{6.5}$$

and

$$G_{00}(q,\gamma) = G_{00}f(q,\gamma)\,, \tag{6.6}$$

The symbol * will denote an average over q and γ, thus

$$G_{\text{finite beam}} = G_{\text{fb}} = [G(q,\gamma)]^* = \frac{\int_0^{\frac{1}{2}D}\int_0^{2\pi} q\,dq\,d\gamma\,G(q,\gamma)}{(\frac{1}{4}\pi D^2)}\,. \tag{6.7}$$

Then we have, using (5a.11)

$$G^* = G_{00}\left\{[f(q,\gamma)]^* + [f(q,\gamma)\Delta_0(q,\gamma)]^* + \cdots\right\}. \tag{6.8}$$

We use (6.1) and (6.2) to obtain $\Delta_0(q,\gamma)$, $\Delta_1(q,\gamma)$ etc. Straightforward expansion of f in a power series and use of the definition of * gives:

$$f^* = 1 + \tfrac{1}{16}\frac{1}{s^2}\frac{D^2}{R_0^2} + \cdots$$

$$(f^2)^* = 1 + \tfrac{3}{16}\frac{1}{s^2}\frac{D^2}{R_0^2} + \cdots$$

$$(f^3)^* = 1 + \tfrac{3}{8}\frac{1}{s^2}\frac{D^2}{R_0^2} + \cdots$$

$$(q\cos\gamma f^3)^* = 0$$

$$(q^2\cos^2\gamma f^3)^* = \tfrac{1}{16}D^2 + \cdots .$$

The above relations suffice to evaluate G^* up to terms in D^2/R_0^2. We express the effect of a finite beam in terms of corrections added to Δ_0, Δ_1 etc., so that (5a.11) still holds with the Δ's replaced by the modified finite beam Δ's. Thus

$$(\Delta_0)_{\text{fb}} = \Delta_0 + \tfrac{1}{16}\frac{D^2}{R_0^2}\left[\frac{1}{s^2} - \tfrac{3}{2}\right], \tag{6.9}$$

$$(\Delta_1)_{\text{fb}} = \Delta_1 + \tfrac{1}{32}\frac{c}{s}\frac{D^2}{R_0^2}, \tag{6.10}$$

$$(\Delta_2)_{\text{fb}} = \Delta_2, \tag{6.11}$$

$$(\Delta_3)_{\text{fb}} = \Delta_3 + \tfrac{1}{64}\frac{c}{s}\frac{D^2}{R_0^2}\left[\tfrac{1}{3}\frac{b_1^2}{h^2} + \frac{<\eta^2>}{h^2}\right], \tag{6.12}$$

and

$$(\Delta_4)_{\text{fb}} = \Delta_4. \tag{6.13}$$

7. Comparison with Other Results

Critchfield and Dodder[3]) calculated G for the case of a vertical front slit and a circular rear aperture up to terms in $\sigma^{(2)}/\sigma$. Their result includes finite beam effects, including those arising from a divergent beam. If their result is adjusted for a non-diverging beam it is in agreement with our expressions (5c.7)–(5c.10) and (6.9)–(6.11).

Breit, Thaxton and Eisenbud[1]) calculated G for the case of a vertical front slit and an arbitrary rear aperture up to terms in $\sigma^{(2)}/\sigma$, including finite beam effects. Their Δ_0 differed from ours because of their neglect of certain second order terms. Their expression (in our notation) is

$$\Delta_0 = \frac{c}{s}<\eta>\epsilon - \tfrac{1}{6}\frac{b_1^2}{\omega^2}\epsilon^2 + \left[\frac{c^2}{s^2} + \tfrac{1}{2}\frac{1}{\omega^2}\right]<\eta^2>\epsilon^2 + \frac{(c^2-2)}{2s^2}<\xi^2>\epsilon^2 . \tag{7.1}$$

This expression leads to a difference in the finite beam corrections. As far as is known, the case of the circular front aperture (see section 8) is not treated elsewhere.

8. Calculation of G for Circular Front and Rear Aperture

We will consider terms only up to those in σ''/σ. Starting with (2.8), we obtain exactly as in section 5a

$$G_n = \frac{\sigma^{(n)}}{\sigma}\frac{1}{n!}\frac{r_1}{R_0 h}\iint_{\mathscr{A}} \mathrm{d}\xi\mathrm{d}\eta \int_{g_1(\epsilon)}^{g_2(\epsilon)} (\Delta\theta)^n \mathscr{I}(\epsilon,t)\mathrm{d}t \tag{8.1}$$

by setting $t = [R_0 r_1/hs]^{-1} z$. The expressions for $\mathscr{I}$ and $\Delta\theta$ are the same as (5a.5) and (5a.6) with b_1 replaced by r_1. We have $g_1(\epsilon)$ and $g_2(\epsilon)$ given by

$$g_2(\epsilon) = \left[\frac{R_0 r_1}{hs}\right]^{-1} z_2 \qquad \text{and} \qquad g_1(\epsilon) = \left[\frac{R_0 r_1}{hs}\right]^{-1} z_1, \tag{8.2}$$

where z_1 and z_2 are now given by (4b.3).

We define $I_n(\in)$ the same as in (5a.7) and use the expansion formula (5a.10). All expressions (with b_1 replaced by r_1) for $I_0(\in)$, $I_1(\in)$, $I_2(\in)$, $I_0(0)$, $I_0^{(1)}(0)$ etc. appearing in section 5 and appendix B are still valid, except those making use of the particular g_1 and g_2 appropriate to the vertical front slit case.

We introduce polar coordinates in the rear aperture plane by

$$\xi = \frac{r_2 k}{A} \sin\varphi \tag{8.3}$$

$$\eta = \frac{r_2 k}{A} \cos\varphi \tag{8.4}$$

where $0 \leq k \leq A$ and $0 \leq \varphi \leq 2\pi$.

Equation (8.1) now becomes

$$G_n = \frac{\sigma^{(n)}}{\sigma} \frac{1}{n!} \frac{r_1}{R_0 h} \left(\frac{r_2}{A}\right)^2 \int_0^A \int_0^{2\pi} k \mathrm{d}k \mathrm{d}\varphi I_n(\in) . \tag{8.5}$$

8a. CALCULATION OF G_0

The calculation of G_0 will be done in some detail. From (8.5) we have

$$G_0 = \frac{r_1 r_2^2}{R_0 h} \frac{1}{A^2} \int_0^A \int_0^{2\pi} k \mathrm{d}k \mathrm{d}\varphi I_0(\in) , \tag{8a.1}$$

The expressions $[g_2 - g_1]_0$ etc. are calculated from (4b.3) and (8.2) and are listed in appendix C.

We note that $I_0^{(1)}(0)$ vanishes on integration over a circular rear aperture. We will in general drop such terms, though we will then be unable to estimate errors due to imperfections in the aperture system.

Then, in terms of $T = 1 - k^2 \sin^2\varphi$, we have

$$G_0 = \frac{r_1 r_2^2}{R_0 h} \frac{8}{A^2} \int_0^A \mathrm{d}k \int_0^{\frac{1}{2}\pi} \mathrm{d}\varphi \left\{ kT^{\frac{1}{2}} + \tfrac{1}{2}\in^2 \left[-\frac{r_1^2}{\omega^2} kT^{\frac{3}{2}} - \frac{3}{\omega^2}\frac{r_2^2}{A^2} k^3 \cos^2\varphi T^{\frac{1}{2}} - \frac{3r_1^2}{A^2} k^3 \sin^2\varphi T^{\frac{1}{2}} \right.\right.$$

$$\left.\left. + \frac{c^2}{s^2}\frac{r_2^2}{A^2} (6\, k^3 \cos^2\varphi T^{\frac{1}{2}} - 2\, k^3 \sin^2\varphi T^{\frac{1}{2}} - 3\, k^3 \cos^2\varphi T^{-\frac{1}{2}} + k^3 \sin^2\varphi T^{-\frac{1}{2}} - k^3 \cos^2\varphi T^{-\frac{3}{2}}) \right] \right\} . \tag{8a.2}$$

We define the following functions[4]) in terms of which we can express G_0, G_1, and G_2.

$$F_1(A) = \int_0^A \int_0^{\frac{1}{2}\pi} k \mathrm{d}k \mathrm{d}\varphi T^{\frac{1}{2}} = \tfrac{1}{3} [(1 + A^2) E(A) - (1 - A^2) K(A)] \tag{8a.3}$$

$$F_2(A) = \int_0^A \int_0^{\frac{1}{2}\pi} k^3 \mathrm{d}k \mathrm{d}\varphi \cos^2\varphi T^{\frac{1}{2}} = \tfrac{1}{45} [(-2 + 7A^2 + 3A^4) E(A) - (1 - A^2)(-2 + 6A^2) K(A)] \tag{8a.4}$$

$$F_3(A) = \int_0^A \int_0^{\frac{1}{2}\pi} k^3 \mathrm{d}k \mathrm{d}\varphi \sin^2\varphi T^{\frac{1}{2}} = \tfrac{2}{15} [(1 - A^2 + A^4) E(A) - (1 - A^2)(1 - \tfrac{1}{2}A^2) K(A)] \tag{8a.5}$$

and $$F_4(A) = \int_0^A \int_0^{\frac{1}{2}\pi} k^3 \mathrm{d}k \mathrm{d}\varphi \cos^2\varphi T^{-\frac{1}{2}} = \tfrac{1}{9} [(-2 + 4A^2) E(A) - (1 - A^2)(-2 + 3A^2) K(A)] . \tag{8a.6}$$

The functions $E(A)$ and $K(A)$ are complete elliptic integrals with modulus A.

It follows immediately from the above that

$$\int_0^A \int_0^{\frac{1}{2}\pi} k \mathrm{d}k \mathrm{d}\varphi T^{\frac{3}{2}} = F_1 - F_3 .$$

[4]) The integrals were evaluated using the "Handbook of Elliptic Integrals for Engineers and Physicists" by Paul F. Byrd and Morris D. Friedman (Springer-Verlag, Berlin, 1954).

We can also show by partial integration that the last two integrals in (8a.2) cancel. Then (8a.2) becomes

$$G_0 = \frac{8r_1r_2^2}{R_0h}\frac{1}{A^2}\left\{F_1 + \tfrac{1}{2}r_2^2\epsilon^2\left[-\frac{1}{\omega^2}\left(\frac{r_1}{r_2}\right)^2(F_1 - F_3) - \frac{3}{\omega^2}\frac{1}{A^2}F_2 - \frac{3}{A^2}F_3 + \frac{c^2}{s^2}\frac{1}{A^2}(6F_2 - 2F_3 - 3F_4)\right]\right\}. \quad (8a.7)$$

8b. CALCULATION OF G_0 AND G_1

We find that $I_1(0) = I_2(0) = 0$ and that $I_1^{(1)}(0)$ and $I_2^{(1)}(0)$ vanish on integration. We obtain

$$G_1 = \left(\frac{\sigma'}{\sigma}\right)\frac{8r_1r_2^2}{R_0h}\frac{1}{A^2}\frac{c}{s}\frac{r_2^2\epsilon^2}{2A^2}\left\{-F_3 + \frac{2}{\omega}[F_3 + F_4 - 2F_2]\right\} \quad (8b.1)$$

and

$$G_2 = \left(\frac{\sigma''}{\sigma}\right)\frac{8r_1r_2^2}{R_0h}\frac{1}{A^2}\frac{r_2^2\epsilon^2}{2\omega^2}\left\{\frac{F_2}{A^2} + \tfrac{1}{3}\left(\frac{r_1}{r_2}\right)^2[F_1 - F_3]\right\}. \quad (8b.2)$$

Acknowledgment

The writer wishes to express his gratitude to Professor H. T. Richards for advice and encouragement. Thanks are due to Dr. W. R. Phillips and Dr. E. M. Bernstein for helpful discussions and checking parts of the calculations, and to S. Salisbury, J. Bishop, W. Campbell, and R. Brown for help in checking the calculations.

Appendix A

Listing of $[g_2 - g_1]_0$ etc. for straight-edge front aperture.

$$[g_2 - g_1]_0 = 2 \quad (A1)$$

$$[g_2^2 - g_1^2]_0 = -4(1-\omega)\frac{\eta}{b_1} \quad (A2)$$

$$[g_2^3 - g_1^3]_0 = 2 + 6(1-\omega)^2\frac{\eta^2}{b_1^2} \quad (A3)$$

$$[g_2^4 - g_1^4]_0 = -8(1-\omega)\frac{\eta}{b_1} - 8(1-\omega)^3\frac{\eta^3}{b_1^3} \quad (A4)$$

$$[g_2^5 - g_1^5]_0 = 2 + 20(1-\omega)^2\frac{\eta^2}{b_1^2} + 10(1-\omega)^4\frac{\eta^4}{b_1^4} \quad (A5)$$

$$[g'_2 - g'_1]_0 = \frac{1}{\omega}\frac{c}{s}[4\eta - 2\omega\eta] \quad (A6)$$

$$[g_2g'_2 - g_1g'_1]_0 = -\frac{1}{\omega}\frac{c}{s}\left[4(1-\omega)\frac{\eta^2}{b_1} + 2b_1 + 2(1-\omega)^2\frac{\eta^2}{b_1}\right] \quad (A7)$$

$$[g''_2 - g''_1]_0 = 2\frac{c^2}{s^2}\frac{1}{\omega^2}[2\eta^2 + 2b_1^2 + 4(1-\omega)\eta^2] \quad (A8)$$

$$[g_2^2g'_2 - g_1^2g'_1]_0 = \frac{1}{\omega}\frac{c}{s}\left[2\eta + 6(1-\omega)^2\frac{\eta^3}{b_1^2} + 6(1-\omega)\eta + 2(1-\omega)^3\frac{\eta^3}{b_1^2}\right] \quad (A9)$$

$$[g_2^3g'_2 - g_1^3g'_1]_0 = -\frac{1}{\omega}\frac{c}{s}\left[8(1-\omega)^3\frac{\eta^4}{b_1^3} + 8(1-\omega)\frac{\eta^2}{b_1} + 2(1-\omega)^4\frac{\eta^4}{b_1^3} + 12(1-\omega)^2\frac{\eta^2}{b_1} + 2b_1\right]. \quad (A10)$$

Appendix B

B1. QUANTITIES USED IN G_1

To get a result correct to second order in ϵ, we need only use the zero and first order terms in $\mathscr{I}$, since $\Delta\theta$ has no zero order terms.

(5a.5) and (5a.6) give

$$\mathscr{I}\Delta\theta = \frac{b_1}{\omega} t\epsilon - \eta\epsilon + 3\frac{c}{s}\frac{b_1^2}{\omega^2} t^2\epsilon^2 - 3\frac{c}{s}\frac{b_1}{\omega}\eta t\epsilon^2 + \tfrac{1}{2}\frac{c}{s}\xi^2\epsilon^2 . \tag{B1.1}$$

Integration of (5a.7) gives

$$I_1(\epsilon) = \tfrac{1}{2}\frac{b_1}{\omega}[g_2^2 - g_1^2]\epsilon - \eta[g_2 - g_1]\epsilon + \frac{c}{s}\frac{b_1^2}{\omega^2}[g_2^3 - g_1^3]\epsilon^2 - \tfrac{3}{2}\frac{c}{s}\frac{b_1}{\omega}\eta[g_2^2 - g_1^2]\epsilon^2 + \tfrac{1}{2}\frac{c}{s}\xi^2[g_2 - g_1]\epsilon^2 \tag{B1.2}$$

$$I_1(0) = 0 \tag{B1.3}$$

$$I_1^{(1)}(0) = \tfrac{1}{2}\frac{b_1}{\omega}[g_1^2 - g_1^2]_0 - \eta[g_2 - g_1]_0 \tag{B1.4}$$

$$I_1^{(2)}(0) = \frac{2b_1}{\omega}[g_2 g'_2 - g_1 g'_1]_0 - 2\eta[g'_2 - g'_1]_0 + 2\frac{c}{s}\frac{b_1^2}{\omega^2}[g_2^3 - g_1^3]_0 - 3\frac{c}{s}\frac{b_1}{\omega}\eta[g_2^2 - g_1^2]_0 + \frac{c}{s}\xi^2[g_2 - g_1]_0 . \tag{B1.5}$$

The use of (5a.10) and appendix A gives

$$I_1(\epsilon) = -\frac{2}{\omega}\eta\epsilon + \frac{c}{s}\left[\xi^2 - 2\frac{\eta^2}{\omega}\right]\epsilon^2 \tag{B1.6}$$

B2. QUANTITIES USED IN G_2

Since $(\Delta\theta)^2$ is second order at lowest, we take

$$\mathscr{I} = 1.$$

$$\mathscr{I}(\Delta\theta)^2 = \frac{b_1^2}{\omega^2} t^2\epsilon^2 - \frac{2b_1}{\omega}\eta t\epsilon^2 + \eta^2\epsilon^2 \tag{B2.1}$$

$$I_2(\epsilon) = \tfrac{1}{3}\frac{b_1^2}{\omega^2}[g_2^3 - g_1^3]\epsilon^2 - \frac{b_1}{\omega}\eta[g_2^2 - g_1^2]\epsilon^2 + \eta^2[g_2 - g_1]\epsilon^2 \tag{B2.2}$$

$$I_2(0) = 0 \tag{B2.3}$$

$$I_2^{(1)}(0) = 0 \tag{B2.4}$$

$$I_2^{(2)}(0) = \tfrac{2}{3}\frac{b_1^2}{\omega^2}[g_2^3 - g_1^3]_0 - \frac{2b_1}{\omega}\eta[g_2^2 - g_1^2]_0 + 2\eta^2[g_2 - g_1]_0 . \tag{B2.5}$$

B3. QUANTITIES USED IN G_3

The lowest order terms in $\mathscr{I}(\Delta\theta)^3$ are third and fourth order.

$$\mathscr{I}(\Delta\theta)^3 = \left(\frac{b_1 t}{\omega} - \eta\right)^3\epsilon^3 + 2\frac{c}{s}\frac{b_1}{\omega}t\left(\frac{b_1 t}{\omega} - \eta\right)^3\epsilon^4 + 3\frac{c}{s}\left(\frac{b_1 t}{\omega} - \eta\right)^2\left(\frac{b_1^2}{\omega^2}t^2 - \frac{b_1}{\omega}\eta t + \tfrac{1}{2}\xi^2\right)\epsilon^4 \tag{B3.1}$$

$$I_3(\epsilon) = \epsilon^3\left\{\tfrac{1}{4}\frac{b_1^3}{\omega^3}[g_2^4 - g_1^4] - \frac{b_1^2}{\omega^2}\eta[g_2^3 - g_1^3] + \tfrac{3}{2}\frac{b_1}{\omega}\eta^2[g_2^2 - g_1^2] - \eta^3[g_2 - g_1]\right\}$$
$$+ \epsilon^4\frac{c}{s}\left\{\frac{b_1^4}{\omega^4}[g_2^5 - g_1^5] - \tfrac{15}{4}\frac{b_1^3}{\omega^3}\eta[g_2^4 - g_1^4] + 5\frac{b_1^2}{\omega^2}\eta^2[g_2^3 - g_1^3] - \tfrac{5}{2}\frac{b_1}{\omega}\eta^3[g_2^2 - g_1^2]\right.$$
$$\left. + \tfrac{1}{2}\frac{b_1^2}{\omega^2}\xi^2[g_2^3 - g_1^3] - \tfrac{3}{2}\frac{b_1}{\omega}\xi^2\eta[g_2^2 - g_1^2] + \tfrac{3}{2}\xi^2\eta^2[g_2 - g_1]\right\} . \tag{B3.2}$$

$$I_3(0) = 0 \tag{B3.3}$$

$$I_3^{(1)}(0) = 0 \tag{B3.4}$$

$$I_3^{(2)}(0) = 0 \tag{B3.5}$$

$$I_3^{(3)}(0) = 6\left\{\tfrac{1}{4}\frac{b_1^3}{\omega^3}[g_2^4 - g_1^4]_0 - \frac{b_1^2}{\omega^2}\eta\,[g_2^3 - g_1^3]_0 + \tfrac{3}{2}\frac{b_1}{\omega}\eta^2\,[g_2^2 - g_1^2]_0 - \eta^3\,[g_2 - g_1]_0\right\} \tag{B3.6}$$

$$\begin{aligned} I_3^{(4)}(0) = {} & 24\left\{\frac{b_1^3}{\omega^3}[g_2^3 g'_2 - g_1^3 g'_1]_0 - \frac{3b_1^2}{\omega^2}\eta\,[g_2^2 g'_2 - g_1^2 g'_1]_0 + \frac{3b_1}{\omega}\eta^2\,[g_2 g'_2 - g_1 g'_1]_0 - \eta^3\,[g'_2 - g'_1]_0\right\} \\ & + 24\frac{c}{s}\left\{\frac{b_1^4}{\omega^4}[g_2^5 - g_1^5]_0 - \tfrac{15}{4}\frac{b_1^3}{\omega^3}\eta\,[g_2^4 - g_1^4]_0 + 5\frac{b_1^2}{\omega^2}\eta^2\,[g_2^3 - g_1^3]_0 - \tfrac{5}{2}\frac{b_1}{\omega}\eta^3\,[g_2^2 - g_1^2]_0\right. \\ & \left. + \tfrac{1}{2}\frac{b_1^2}{\omega^2}\xi^2\,[g_2^3 - g_1^3]_0 - \tfrac{3}{2}\frac{b_1}{\omega}\xi^2\eta\,[g_2^2 - g_1^2]_0 + \tfrac{3}{2}\xi^2\eta^2\,[g_2 - g_1]_0\right\} \end{aligned} \tag{B3.7}$$

$$I_3(\epsilon) = -\left[\frac{2}{\omega^3}\eta^3 + \frac{2}{\omega^3}b_1^2\eta\right]\epsilon^3 + \frac{c}{s}\left[-\frac{2}{\omega^3}\eta^4 - \frac{2}{\omega^3}b_1^2\eta^2 + \frac{b_1^2}{\omega^2}\xi^2 + \frac{3}{\omega^2}\eta^2\xi^2\right]\epsilon^4. \tag{B3.8}$$

B4. QUANTITIES USED IN CALCULATING G_4

$$\mathscr{I}(\Delta\theta)^4 = \left(\frac{b_1 t}{\omega} - \eta\right)^4 \epsilon^4 \tag{B4.1}$$

$$I_4(\epsilon) = \frac{\epsilon^4}{5}\frac{\omega}{b_1}\left\{\left(\frac{b_1}{\omega}g_2 - \eta\right)^5 - \left(\frac{b_1}{\omega}g_1 - \eta\right)^5\right\} \tag{B4.2}$$

$$I_4(0)\,,\ I_4^{(1)}(0) \cdots I_4^{(3)}(0) = 0 \tag{B4.3}$$

$$I_4^{(4)}(0) = \tfrac{24}{5}\frac{\omega}{b_1}\left\{\left(\frac{b_1}{\omega}g_2(0) - \eta\right)^5 - \left(\frac{b_1}{\omega}g_1(0) - \eta\right)^5\right\}. \tag{B4.4}$$

Appendix C

Listing of $[g_2 - g_1]_0$, etc. for circular front aperture.

$$[g_2 - g_1]_0 = 2T^{\frac{1}{2}} \tag{C.1}$$

$$[g_2^2 - g_1^2]_0 = -4k\cos\varphi\,T^{\frac{1}{2}} \tag{C.2}$$

$$[g_2^3 - g_1^3]_0 = 2T^{\frac{1}{2}}[3k^2\cos^2\varphi + T] \tag{C.3}$$

$$[g'_2 - g'_1]_0 = 2\frac{c}{s}\frac{r_2 k}{A}\cos\varphi\,T^{\frac{1}{2}}\left[\frac{2}{\omega} - \frac{1}{T}\right] \tag{C.4}$$

$$[g_2 g'_2 - g_1 g'_1]_0 = 2\frac{c}{s}T^{\frac{1}{2}}\left[\frac{r_2 k^2}{\omega A} - \frac{r_1}{\omega} + \frac{r_2 k^2}{A}\frac{\cos^2\varphi}{T} - \frac{4r_2 k^2}{\omega A}\cos^2\varphi\right] \tag{C.5}$$

$$[g''_2 - g''_1]_0 = 2\frac{c^2}{s^2}T^{\frac{1}{2}}\left[\frac{r_2^2 k^2}{A^2 T} + \frac{2r_1^2}{\omega^2} - \frac{2r_2^2 k^2}{\omega^2 A^2} - \frac{r_2^2 k^2\cos^2\varphi}{A^2 T^2} + \frac{8}{\omega^2}\frac{r_2^2}{A^2}k^2\cos^2\varphi - \frac{4}{\omega}\frac{r_2^2}{A^2}\frac{k^2\cos^2\varphi}{T}\right]. \tag{C.6}$$

NUCLEAR INSTRUMENTS AND METHODS 4 (1959) 67–78; NORTH-HOLLAND PUBLISHING CO.

MAGNETIC MEASUREMENTS ON THE CORNELL ALTERNATE GRADIENT SYNCHROTRON†

E. MALAMUD and A. SILVERMAN††

Cornell University, Ithaca, New York

Received 5 January 1959

A brief description of the synchrotron magnet is followed by a summary of the factors leading to a choice of field gradient, and a description of the pole tip design. Measurements of the synchrotron field gradients at low, medium and high fields are described. The medium and high field gradients are measured using a rotating coil magnetometer. The gradients at injection time have been determined by two independent methods: (1) using the electron beam itself to find the radial and vertical focal points; and (2) using peaking strips to make zero time measurements. The results of these measurements and also the determination of the magnetic lens boundaries are summarized.

1. Introduction

The publication of the Alternate Gradient focusing principle of Courant, Livingston, and Snyder[1]) in 1952 coincided with design studies starting at Cornell for the construction of a conventional weak focusing ($n = 0.6$) electron synchrotron capable of reaching an energy of approximately 1.5 GeV. Alternate gradient focusing, while obviously finding its greatest usefulness at somewhat higher energies than 1.5 GeV, seemed to have significant advantages over the weak focusing design even at this modest energy, and so late in 1952 attention was shifted to the design of an alternate gradient synchrotron. Construction was completed in 1954. Since 1956 the synchrotron has been operating at moderate beam intensities (2×10^{13} MeV/minute) and with reasonable stability and has accelerated electrons to a peak energy of 1.2 GeV[2,3]).

In this paper we will first describe the magnet and some of the design features which it incorporates. This will be followed by a description of magnetic measurements. Other workers[4]) have described magnetic measurements on a weak focusing synchrotron; this paper will describe similar measurements applied to a strong focusing synchrotron.

2. Magnet Construction

The magnet is of the racetrack type with four 90° quadrants and four straight sections. A cross section of the magnet is shown in fig. 1. The C's are 0.014″ laminations punched out of Armco 52 silicon steel. The pole tips are also 0.014″ thick, punched from Armco 3X silicon steel. This is an oriented steel and the poles are punched so that the axis of large permeability is radial. The poles are held in place by air pressure at about 600 psi introduced into the pressure tubing shown in fig. 7. The pole separation is determined to an accuracy of about ± 0.002″ by the machined bakelite spacer on the inside and the homolite spacers on the outside.

Some of the relevant statistics concerning the synchrotron are shown in table 1.

† Supported in part by the joint program of the Office of Naval Research and the U. S. Atomic Energy Commission.

†† Presently at Istituto Nazionale di Fisica Nucleare, Laboratori di Frascati, Casella Postale 15, Roma, Italy.

[1]) E. Courant, M. Livingston and H. Snyder, Phys. Rev. 88 (1952) 1190.

[2]) A. Silverman, D. Corson, J. DeWire, D. Luckey, R. Martin, B. McDaniel, R. Wilson and W. Woodward, Bull. Am Phys. Soc. 1 (1956) 59.

[3]) R. R. Wilson, The Cornell BeV Synchrotron, Office of Naval Research Report (1956) unpublished.

[4]) G. K. Green, R. R. Kassner, W. H. Moore and L. W. Smith, Rev. of Sci. Instr. 24 (1953) 743.

TABLE 1

General Data on the Cornell Alternate Gradient Synchrotron

Radius of the Central Orbit	150″
Length of Straight Section	36″
Pole Tip Aperture	about 1.6″ × 5.0″
Donut Aperture	about 1.0″ × 2.6″
Total Weight of Iron	25 tons
Total Weight of Copper	3.5 tons
Total D.C. Resistance of Magnet Coils	16 mΩ
Number of Turns/Quadrant	12
Total Inductance of Magnet	16 mH
Excitation Frequency	30 cps
Field on Central Orbit (1.5 GeV Excitation)	13.5 kG
Peak Magnet Current (1.5 GeV Exitation)	about 3000 A
Power Dissipated at 1.5 GeV Excitation	about 250 kW

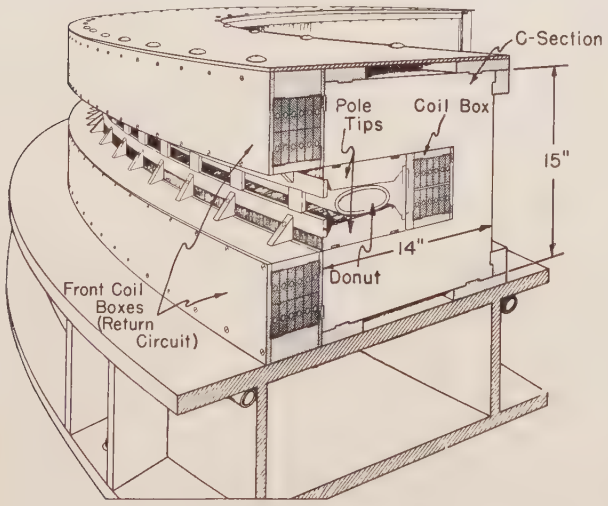

Fig. 1. Magnet cross section.

3. Magnet Excitation

The magnet is excited with a mixture of A.C. and D.C. currents. The exciting current is shown in fig. 2. The magnet inductance, plus the condenser C_1 are resonant at 30 cps with a Q of about 40. The choke and the condenser bank C_2 are also resonant at 30 cps and provide a high impedance to keep A.C. out of the D.C. generator. The use of D.C. biasing has a number of significant advantages: (1) It decreases the maximum voltage across the magnet by a factor of almost two. (2) The A.C. dissipation in the magnet is decreased by a factor of about four. (3) By controlling the ratio of the A.C. to D.C. currents, the initial rate of rise of magnetic field can be varied over a large range. This can be very useful either in matching the R.F. voltage available at injection or in making use of the fact that the magnetic field at injection time is a sensitive function of the precise mixture of A.C. and D.C. currents.

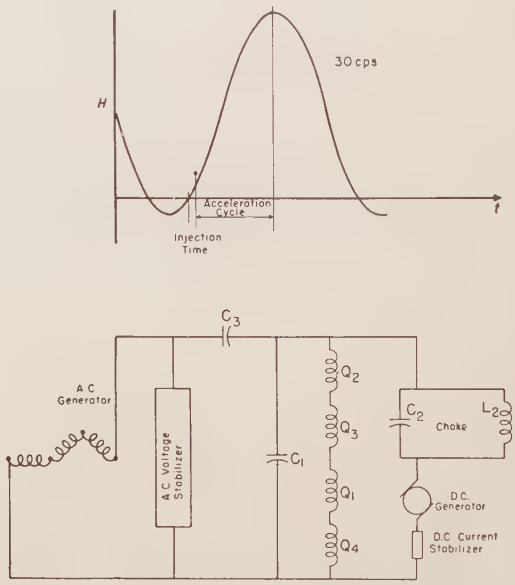

Fig. 2. Magnetic field vs. time and magnet excitation circuit. Q_1 through Q_4 are the four quadrants of the magnet, C_1 resonates the magnet to 30 cps, and C_2 resonates the choke to 30 cps.

4. Choice of "Operating Point"

The most important question to be answered in designing the magnet is what "operating point" to use—that is, what field gradient and what lattice structure. It is not our intention to discuss the theory of alternate gradient focusing in detail since there is much literature on the subject[5,6]). However, we would like to point out some of the considerations that went into the choice of the present "operating point". Many of the choices were based on calculations performed by J. M. Sellen, Jr.,[7]) and E. Bodenstedt[8]).

[5]) S. Lundquist, Phys. Rev. **91** (1953) 981.

[6]) E. D. Courant and H. S. Synder, Annals of Physics **3** (1958) 1.

[7]) J. M. Sellen, Jr., Private Communication.

[8]) E. Bodenstedt, Rev. of Sci. Instr. **27** (1956) 218.

The usual representation for field gradient is n, which we define by:

$$n = -\frac{dH}{dr}\frac{r_0}{H_0} \tag{1}$$

where r_0 is the central orbit radius (150″) and H_0 is the magnitude of the field at the central orbit. Fig. 3 shows the operating point chosen and fig. 4 shows the magnetic lattice. The lattice has quasi-octagonal symmetry inasmuch as

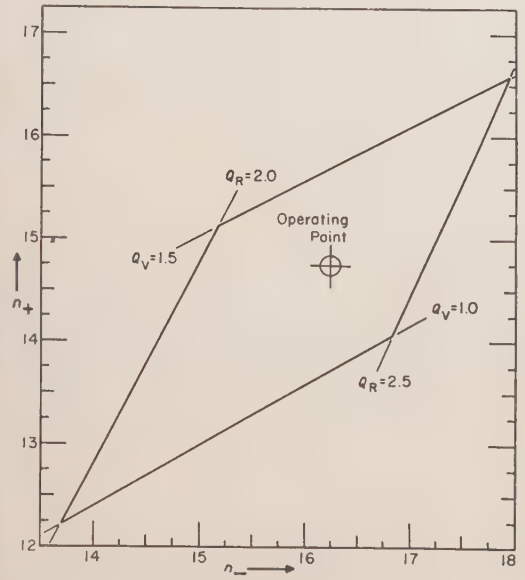

Fig. 3. Stability diamond and operating point. Q_V and Q_r are the frequencies of the betatron oscillations in terms of the frequency of revolution. The lines shown are resonances along which operation is unstable.

pseudo-straight sections are placed in the central region of each quadrant. This is done by making $n = +1$ in this region for a distance of 36″, the same length as the straight sections. Making $n = +1$ balances out the centrifugal force and makes the horizontal motion about the

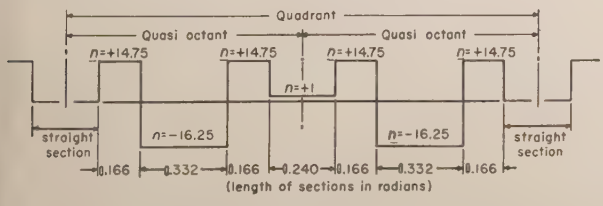

Fig. 4. Magnetic lattice. Radial octant stacking.

central orbit exactly the same as in a straight section. This type of symmetry removes one of the large forbidden regions down the center of the stability pattern and hence increases the size of adjoining stability diamonds. The choice of $n = +1$ in the center of each quadrant together with the particular symmetry of the positive and negative lenses used (see fig. 4) results in a lattice that is called the "radial octant". The choice of the positive n value adjoining the straight sections was made because calculations[8]) indicated that such a "positive radial octant" would minimize the radial spread of orbits in the straight sections.

With the choice of a "positive radial octant" stacking, a stability diagram was calculated[7]). The main region of stability lies between the lines $Q_V = 0$ and 4, and $Q_r = 0$ and 4, where Q_V and Q_r are the vertical and radial betatron oscillation frequencies measured in terms of the frequency of revolution.

A particular "diamond" in the stability diagram was chosen using the following criteria: (1) The $Q_V = Q_r$ line should not lie in the diamond. (2) The diamond can contain an integral difference line ($Q_r - Q_V$ = integer) and a half integral sum line, but should not contain an integral sum line. (3) The diamond should not border on the $Q_V = 2.0$ band or on the forbidden regions outside the lines $Q_V = 0$ and 4, $Q_r = 0$ and 4. These criteria eliminate all but a few possible diamonds. The one chosen, shown in fig. 3, has a large width in n-value and thus makes the pole tip design less critical.

5. Pole Tip Design

The pole pieces were designed to give the maximum radial extent of the desired uniform gradient at intermediate magnetic fields, i.e., 500 gauss $< H <$ 9000 gauss. The field at injection time ($H = 20$ G) is very largely determined by the residual fields and eddy currents and one has to reconcile himself to providing field correcting coils to take care of field distortions at low magnetic fields. No attempt has been made to date to do any correcting for saturation effects.

As is well known, a hyperbolic pole tip of infinite length will produce a magnetic field

having a constant gradient. With a finite pole, flux leakage produces deviations from a constant gradient and it is necessary to provide magnetic shims[9]) if the gradient is to be kept constant over as large a radial aperture as possible. The central 3″ of the 5″ wide poles is a four chord approximation to the theoretical hyperbola (except for the $n = 1.0$ pole where a one chord approximation is sufficient). The shims were then adjusted empirically by successive approximations to give the maximum radial aperture.

In order to do the design work, a one foot long, full scale model of the magnet was constructed. The C's were made of laminated iron, but the initial design was done with solid poles and D.C. excitation of the model. It is, of course, much less expensive and time consuming to be able to make model measurements with solid poles since many small changes have to be made before the final design is chosen, and to do this with laminations punched to the required accuracy is very inconvenient. It is expected that the results obtained with the solid poles will be very close to those obtained with laminated ones at intermediate fields where the residual fields, eddy currents, and saturation effects are negligible.

in the contact resistance between the rotating brushes and the stationary contact. To obtain the accuracy desired (1 part in 10^5 in the ratio of the signals from the two coils), it was necessary to keep the variation in contact resistance to the order of 1 ohm. The brush arrangement shown in fig. 5 proved to be completely satisfactory. The three independent wires of the two coils (one wire is common) run down the center

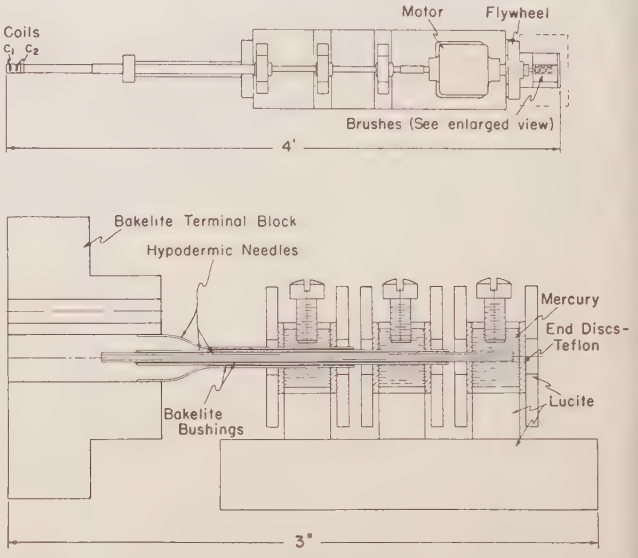

Fig. 5. Top view of rotating coil magnetometer and side view of brush arrangement details.

6. Rotating Coil Magnetometer

In order to make the measurements under D.C. conditions, a rotating coil magnetometer was constructed as shown in fig. 5. The magnetometer consists of two coils, C_1 and C_2, mounted with their axes parallel on the same rotating shaft. The coils are $\frac{3}{16}$″ diameter and spaced 0.380″ apart and are constructed to be as nearly identical as possible. Each coil is wound with No. 42 copper wire and has a turns-area of about 1000 cm². The shaft is driven by a 30 cps synchronous motor. The signals from the two rotating coils are compared by a null method and the comparison determines the field gradient.

The accuracy with which the measurement can be made depends primarily on the noise input to the amplifier and by far the worst source of noise is "brush noise", i.e. fluctuation of the rotating shaft and terminate in 3 coaxial hypodermic needles insulated from each other by thin bakelite bushings. Each hypodermic needle is imbedded in a pool of mercury from which the signal is taken. The small size of the brushes (i.e. the hypodermic needles) keeps the peripheral velocity small and consequently the cavitation of the mercury, the primary source of noise, small. This arrangement provides a sufficiently small noise level so that the ultimate limitation in the accuracy of the measurement proved to be elsewhere.

The signals from the two coils (C_1 and C_2) were fed into the circuit shown in fig. 6, and were arranged to be out of phase with each other so that the input to the amplifier is a known fraction of the voltage induced in C_1 subtracted from the voltage induced in C_2. If the axes of

[9]) M. E. Rose, Phys. Rev. **53** (1938) 715.

the two coils are not precisely parallel an out of phase component is introduced which cannot be balanced out by the resistance bridge. The condenser, C, in series with one of the coils is used to balance out this out of phase component. The impedance of this condenser at 30 cps is $\approx 100\ \Omega$. This makes a correction in the balance resistance of the order of $\frac{1}{2}\,(100/75\,000)^2$ which can be neglected.

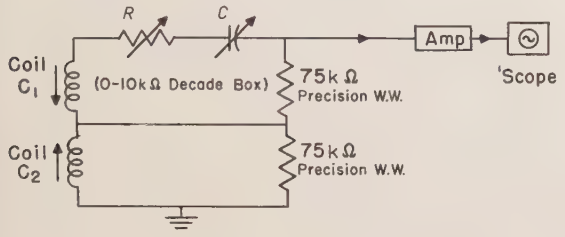

Fig. 6. Bridge circuit for rotating coil measurements. Input to the amplifier is the difference between a known fraction of the signal induced in C_1 and the signal induced in C_2. Amplifier has a gain of about 1000.

To calculate n we first expand H in a Taylor series about r_0:

$$\left(H = H_0 + \frac{\mathrm{d}H}{\mathrm{d}r}\right)_{r_0} (r - r_0) \qquad (2)$$

$$+ \cdots \simeq H_0 \left[1 - \frac{n_0}{r_0}(r - r_0)\right].$$

Substituting this into expression (1) we get:

$$n = -\frac{\Delta H}{H}\frac{1}{\Delta r}\left[r_0 - n_0 (r - r_0)\right] \qquad (3)$$

where Δr is the coil spacing and n_0 is n measured on the central orbit. In terms of the circuit parameters:

$$\begin{aligned} V_1 &= kH_1 \\ V_2 &= k'H_2 \end{aligned} \qquad (4)$$

where V_1, V_2, H_1, H_2 are the voltages and fields at coils 1 and 2. If for now we assume that $k = k'$, i.e. the turns-area of the two coils are equal then we get

$$n = -2\frac{V_2 - V_1}{V_2 + V_1}\frac{1}{\Delta r}\left[r_0 - n_0 (r - r_0)\right] \qquad (5)$$

and finally arrive at

$$n = -\frac{R}{75\ \mathrm{k}\,\Omega + \frac{1}{2}R}\frac{1}{\Delta r}\left[r_0 - n_0 (r - r_0)\right]. \qquad (6)$$

In using eq. (6) it is assumed that the turns-area of the two coils C_1 and C_2 are identical. This is of course not true and in order to obtain the gradient the relative turns-area of the coils must be determined. The coils were placed in a field used for magnetic resonance experiments which had been determined to be uniform over the relevant region to about 1 part in 10^5 [10]). The signals from the two coils were then compared. If the field is truly uniform, then the ratio of the turns-area of the two coils is determined with the same precision with which we can determine the ratio of the voltages. In fact, one doesn't require a very highly uniform field for the calibration since the positions of the two coils can be reversed and the measurement repeated. The ratio of the turns-area is then known independently to first order of the uniformity of the magnetic field.

The accuracy of the measurement was such that a balance could be determined with an accuracy of 1 ohm in R. This corresponds to an accuracy of about 1 in 10^5 for the ratio of the two voltages and this was the relative accuracy of the various measurements. This accuracy is sufficient to determine relative gradients to about 0.1%. The absolute accuracy of the gradient is not as well known since it depends on the coil spacing, the positioning of the probe in the synchrotron gap, and the various resistances in the bridge circuit, as well as the relative measurement of the two signals. The absolute value of the gradient could be determined to about 0.4%. This corresponds to an error in n of $\Delta n = 0.06$.

The rotating coil magnetometer is also used to measure A.C. field gradients with comparable accuracy by properly phasing the motor.

7. Gradient Measurements at Intermediate and High Fields Saturation Effects

Once the proper pole shape had been determined for the D.C. poles, laminated poles were punched with the same profile. It was found that the assumption that the laminated poles would give

[10]) We are grateful to Professor D. F. Holcomb for the use of this magnet.

the same result as the solid poles at intermediate field strengths was correct. The measurements with laminated poles were made with both A.C. and D.C. excitation and were found to give the same value of the gradient at intermediate field strength as determined by the solid poles under D.C. conditions.

The final pole shape is shown in fig. 7. Fig. 8 shows gradient measurements for both the

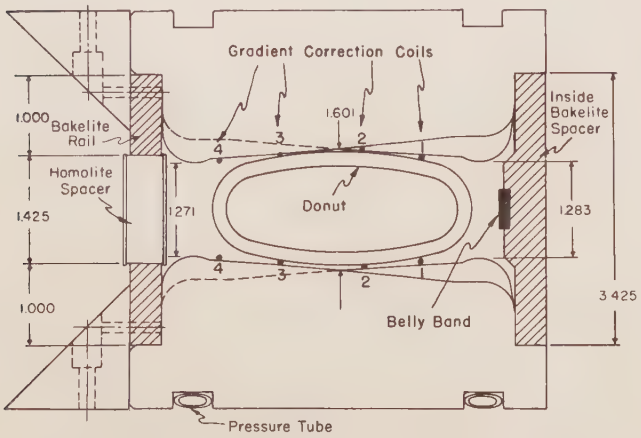

Fig. 7. Pole piece assembly showing shape of positive and negative poles and location of correction coils. (Dimensions in inches.)

positive and negative lenses. The horizontal lines at approximately $n = -16.25$ and $n = +14.75$ are the design values. One sees that at intermediate fields the n value is quite com-

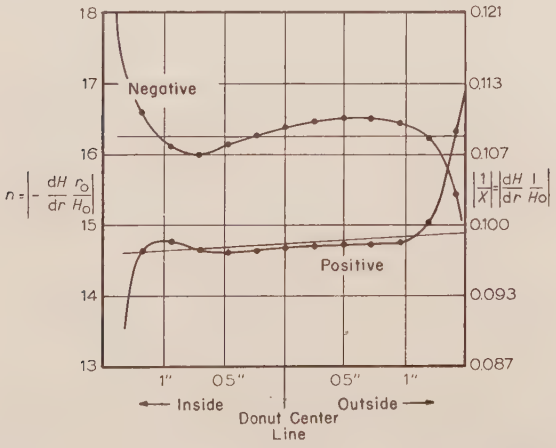

Fig. 8. Gradient measurements at intermediate fields, $H_0 \approx 1000$ gauss. No significant variation in the shape of the gradient can be detected in either lens from $H \approx 500$ gauss to $H \approx 8000$ gauss.

fortably within the chosen diamond (see fig. 3) for a radial aperture of at least $2\frac{1}{2}''$. This provides

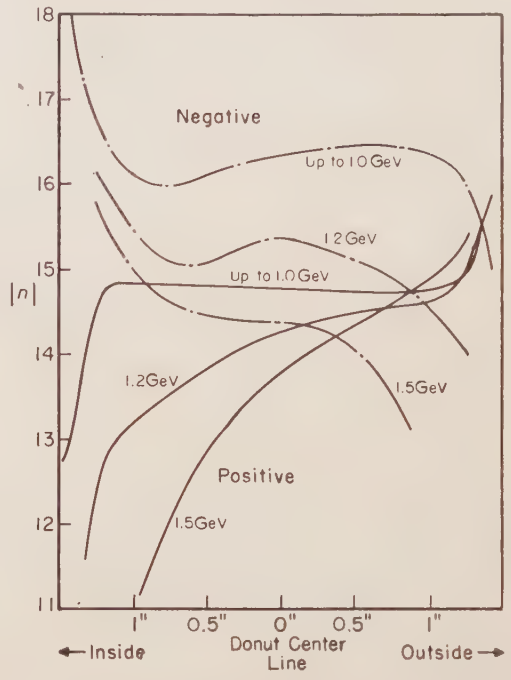

Fig. 9. Gradient measurements at high fields showing effect of saturation.

a good match to the glass donut which has a radial aperture of about $2\frac{3}{4}''$.

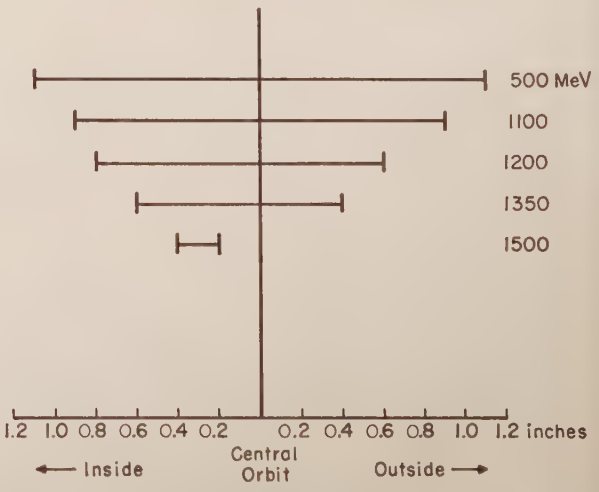

Fig. 10. Effective radial aperture for various magnet excitations.

The peak excitation of the magnet is designed to give 13.5 kg at the equilibrium orbit which

corresponds to 1.5 GeV. However, at an energy considerably below this (1.1–1.2 GeV) saturation effects begin to limit the useful aperture. The measurements of the gradient made on the model at energies from 1.0 GeV to 1.5 GeV are shown in fig. 9. One sees that even at 1.2 GeV, the gradient has changed considerably from the intermediate field values. The effect of the change can be seen more graphically if one plots the effective radial aperture as a function of excitation. The aperture is defined by the region within which the gradient is in the same diamond as the normal operating point. The effective aperture vs. excitation is plotted in fig. 10. One sees that the radial aperture is reduced above 1.0 GeV, but remains finite up to 1.5 GeV. Whether this aperture will be sufficient to enable acceleration up to this energy is not known at present. The peak energy to which electrons have been accelerated to date is 1.2 GeV.

8. Gradient Measurements at Low Fields Injection Conditions

A Van de Graaff generator injects 2 MeV electrons into the synchrotron at a field of 20 gauss. It is, of course, very important to have the field gradients correct (i.e., such that the operating point falls in the same diamond as at intermediate fields) over as large a region as possible at injection time since both the betatron oscillations and the phase oscillations are maximum at this time. Also, at such low fields the residual fields and eddy current fields have very great influence on the field gradients and one must expect significant differences from what is measured in the intermediate field region. To correct for these effects a set of 4 gradient correction coils are placed on the top and bottom pole faces, located as shown in fig. 7. The coils are made of copper clad bakelite similar to the material used in printed circuits. The bakelite backing is $\frac{1}{64}''$ thick and the copper strips are $\frac{1}{16}''$ wide and 0.002″ thick. Because of the large surface from which heat can be carried (i.e., the bakelite backing), the correction coils can carry up to 15 A without overheating although the corrections used are only about 1 A.

The gradient correction coils are separate for negative and positive lenses. All the correction coils are A.C. excited with the phase adjusted to give maximum correction at zero time. Corrections are necessary only at injection time and shortly thereafter.

In general, to make a change in the gradient, the same current is set in the top and bottom coils located at the same radius. The symmetrical arrangement prevents any distortion of the median plane of the magnet; conversely, by unbalancing the currents in the top and bottom coils a correction can be applied for any median plane distortions that may be built into the magnet. In order to adjust the currents in the coils some information must be obtained about the gradients at injection time. Such measurements were made in two independent ways: (1) by measuring the frequency of the vertical and horizontal betatron oscillations and thus measuring Q_v and Q_r directly, and (2) by making zero time measurements with peaking strips.

9. Measurements of Q_v and Q_r at Injection Time

These measurements were carried out as follows. The 2 MeV beam is first well collimated and then injected on the center line of the magnet. The first turn can be made to stay on the center line to within a few millimeters. The input beam is then "wiggled" both radially and vertically and the radial and vertical foci on the first turn observed. The foci can be located with an accuracy of about 5 cm and so the Q's can be determined with good accuracy ($\Delta Q < 0.1$). The correction currents are then adjusted so that Q_v and Q_r are equal to the design figures, i.e. 1.25 and 2.25 respectively. This method works very well for measurements made near the center of the donut.

In principle one might hope to repeat the same procedure throughout all sections of the donut and so explore the complete aperture. However, when this same technique was tried when the beam was injected $\frac{1}{2}''$ towards the outside of the donut a number of dfficulties

were encountered. The first problem is that the equilibrium orbit is no longer circular but scallopped. The amplitude of the scallops is about equal to the radial displacement from the centers. This means that the beam is not confined to a small region of the donut but probes a significant fraction of it. Also, it becomes quite difficult to find the equilibrium orbit about which to induce oscillations. And finally towards the outside of the donut there are significant median plane distortions which cause serious coupling between vertical and radial motions.

This coupling between the vertical and radial motion was minimized by unbalancing the correcting currents in the top and bottom gradient coils. For the central region of the donut ($\approx \frac{3}{4}''$) the measurement of the frequency of the betatron oscillations provides a very sensitive measure of the operating point. We have found that adjusting the corrections by this technique has always made it possible to find an accelerated beam.

We have since checked the operating point experimentally by the technique of shaking out the beam by applying an R.F. field of frequency equal to the betatron frequency[11,12]). We have found that the actual operating point from 4 MeV to 1000 MeV is very close to the design value.

10. Peaking Strip Measurements

In addition to the "integral" information obtained from the electron beam itself, one would also like to have some differential information on the behavior of the magnet. This was obtained by measuring the time at which the magnetic field passes through zero at various radii. The assumption is made that the variation in zero time is caused by eddy current fields and residual fields and that if all parts of the magnet were to pass through zero field simultaneously the n-value would remain constant throughout the acceleration cycle and be equal to the value measured for intermediate fields.

The zero time measurements were made with "peaking strips"[13]) made out of 0.001″ diameter Mo-Permalloy wire[14]). The strips were 1″ long. Around the center $\frac{1}{4}''$ a pickup coil of about 80 turns of No. 36 Formex wire was wound. A larger concentric coil of 500 turns of No. 36 wire was added to bias the strip. The strips were prepared by gluing them into a glass capillary tube with an epoxy resin while they were under tension[15]). This technique appreciably shortens the pulse duration from the strip. The pulses were about 1 μsec wide for a rate of rise of field of 0.3 gauss/μsec. The zero time measurements were then made as follows. Three peaking strips were placed in the A.C. field of the synchrotron. One of them is used to trigger a dual trace oscilloscope. The signals from the other two strips, one of which is kept fixed in position, and one of which is movable, are differentiated, amplified, and then displayed on alternate traces of the oscilloscope. These two signals are then brought into coincidence by varying the bias on the fixed strip. The bias current on the fixed strip can be calibrated in terms of a time delay. Thus by comparing the biases necessary to bring the two signals into coincidence as the radial position of the movable strip is changed one measures dt/dr, the rate of change of zero time with radius when the average field is zero. The correction currents are adjusted to make dt/dr minimum over as large a region of the donut as possible.

There are a number of precautions which must be observed in making this measurement. Because of residual fields (and possibly eddy currents) in the peaking strips themselves the peaking strip pulses do not necessarily occur at zero field. In fact, for the peaking strips prepared as described above, the residual fields were of the order of 1–2 gauss. Thus, unless this is compensated for we are adjusting the

[11]) C. L. Hammer, R. W. Pidd and K. M. Terwilliger, Rev. of Sci. Instr. **26** (1955) 555.

[12]) Professor J. W. DeWire performed the measurement in this laboratory.

[13]) J. M. Kelly, Rev. of Sci. Instr. **22** (1951) 256.

[14]) We are greatly indebted to Dr. G. K. Green of Brookhaven National Laboratory for very kindly supplying us with this rare material.

[15]) Technique suggested to us by G. Sacerdoti, private communication.

correction currents to make the time at which the field goes through 1–2 gauss uniform throughout the magnet. This, of course, introduces an error in n at injection time of

$$\frac{\Delta n}{n} = \frac{H \text{ residual in peaker}}{H \text{ injection}} = 0.1 .$$

This error is sufficient to throw the operating point into a completely different diamond and make it necessary to cross a resonance line sometime during the acceleration cycle. The compensation for this residual field was done as follows. An air core solenoid was constructed with a rate of rise of field at zero field equal to that of the synchrotron at injection time. The solenoid was excited by 60 cycle line current. The strip whose residual field is to be determined is placed inside the solenoid and the signal placed on the vertical plates of an oscilloscope. A signal in phase with the current to the solenoid is used to provide the sweep for the oscilloscope. The strip will provide a signal each half cycle of the 60 cycles and so each sweep two pulses occur on the oscilloscope. The two pulses will appear superimposed only if the peaking strip signals appear at zero field in the solenoid. At any other value of the field the signals will appear displaced from each other, and the displacement time is a measure of field in the solenoid at which the peaking strip signal appears. The current in the bias coil surrounding the strip is then adjusted so that the two signals appear superimposed. This could be done to about an accuracy of 0.2 μsec which corresponds to an error in the zero field signal of about 0.05 gauss. It was also found that the bias necessary to superimpose the two signals was essentially constant with variation of the rate of rise of field of the order of 30%. We take this to mean that the residual fields in the strips are essentially independent of the peak field to which they are exposed and that the eddy current effects were small. The bias current settings found in the solenoid were used in all the synchrotron field measurements.

Let us consider the sensitivity of the method as applied to the Cornell synchrotron. The design rate of rise of field at injection time is 0.3 gauss/μsec. For $r_0 = 150''$ and $H = 20$ gauss (injection field) $\Delta n \simeq 2.25$ (dt/dr) where dt/dr is expressed in μsec/inch. A change of 0.1 μsec could easily be detected. This results in an uncertainty in n of about 0.25. For n-values of ≈ 15 this sensitivity is adequate to tell if the operating point at injection lies within the chosen diamond in the stability diagram. The measurements can be done to this accuracy only in the central 2–3″ of the pole tip where the gradient is reasonably constant. Where the gradient is changing rapidly the peaking strip measurement is difficult to make because the pulse shape as well as the time are changing with radial position.

The solid curves in fig. 11 show zero time measurements for the uncorrected field at

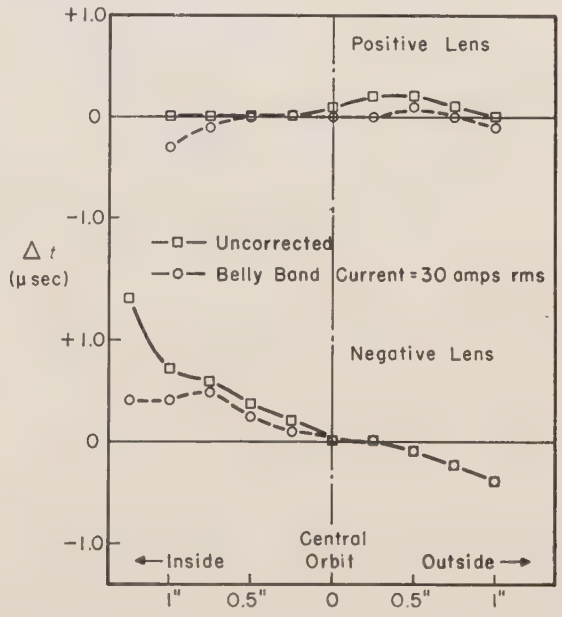

Fig. 11. Zero time measurements at 750 MeV.

750 MeV excitation. Extensive measurements were taken at 750 MeV excitation since the beam hunting was first done at that energy. The large phase shift inside the central orbit observed in the negative lens is believed due to eddy currents in the inner synchrotron coil. The negative lens will be affected more than the positive because the aperture in the negative lens opens up towards the inside. To offset this a

correction coil called the belly band was installed. Its position with respect to the pole tips can be seen in fig. 7. It is a single turn around the synchrotron and is near the inner coil. The dashed curves in fig. 11 show zero time measurements with 30 A rms flowing in the belly band.

The procedure now is to vary the gradient correction coils until dt/dr is as close to zero as

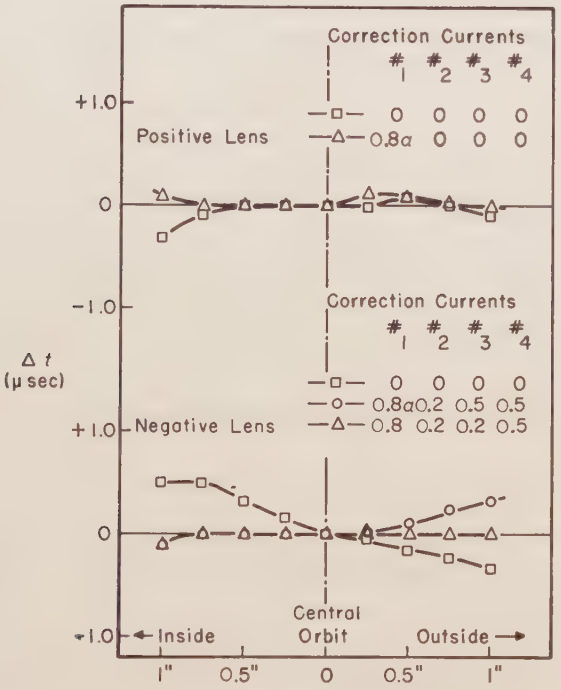

Fig. 12. Zero time measurements at 750 MeV with various correction coil currents.

possible over the region of the aperture in which the donut is situated. Fig. 12 shows zero time measurements at 750 MeV excitation for various gradient correction coil currents, the belly band current being kept fixed at 30 A. The curves with the triangle points correspond to the best set of correction currents. It is seen that $\Delta t \lesssim 0.1$ μsec over the central two inches of the donut.

The gradient at injection time, affected as it is by residual and eddy current effects will depend on the magnet excitation. Thus in going to 1 GeV operation with the same injection rate of rise of field as before (0.3 g/μsec) a new set of correction currents must be found. The dotted curve in fig. 13 is a measurement at 1 GeV with the optimum correction currents for 750 MeV operation. The solid curve shows zero time measurements with the optimum correction currents for 1 GeV operation. One sees that the best corrections at 750 MeV excitation are no longer best at 1 GeV. From a long series of such measurements, it has become clear that the shape of the field at injection time is very

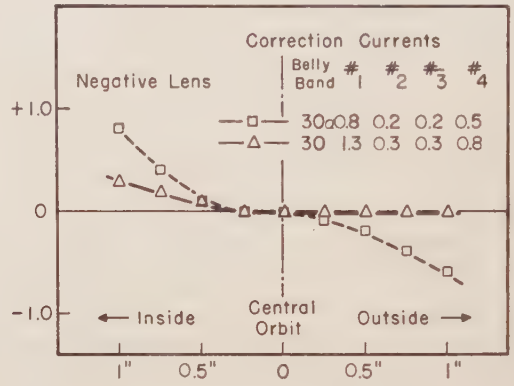

Fig. 13. Zero time measurements at 1 GeV. □'s are correction currents which make field best at 750 MeV. △'s are corrections required at 1 GeV.

sensitive to the precise ratio of A.C. and D.C. currents. In fact for $I_{A.C.}/I_{D.C.} \simeq 1.4$ the field is remarkably good. This is also approximately the ratio at which the residual field is minimum.

When the optimum correction currents are found, zero time measurements are repeated in various positive and negative lenses around the synchrotron. With this given set of correction currents the variations in dt/dr from lens to lens are not more than 0.1 to 0.2 μsec in two inches.

An azimuthal variation in zero time at fixed radius is found, probably due to variations in the tightness of stacking the pole tip laminations. This has an rms-value of about 1 μsec at 1 GeV excitation. Its periodicity is very high and no systematic variation from quadrant to quadrant is seen. No attempt is made to correct for this variation since it should have no deleterious effects.

Professor B. McDaniel has constructed an electron gun that fits in the synchrotron gap which can also be used to make zero time

measurements. It is less convenient to use than peaking strips but it has provided a valuable check on the peaking strip measurements. A series of measurements made with the gun agreed with the peaking strip measurements and confirmed that the method of compensating for residual field in the peaking strip was correct.

11. Lens Boundaries

One of the peculiarities of the strong focusing magnet is the abrupt gradient changes at the lens boundaries within the quadrant. In the synchrotron the boundaries are bevelled to reduce eddy currents. The exact shape of the bevel was determined by measurements in the model magnet. The radial variation of n was measured at various azimuths and the transition pieces were made so that the mean n-value between the two sectors was reached at about the same azimuthal position in all radii within the donut. Fig. 14 shows medium field measurements for the $+-$ transition. The solid

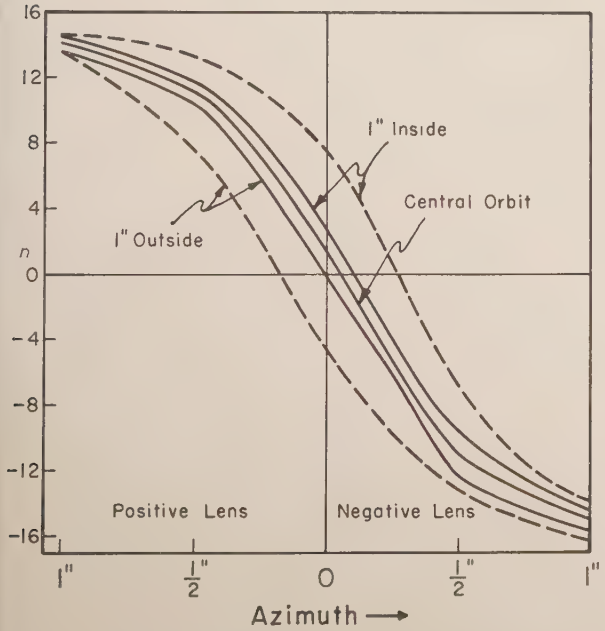

Fig. 14. Azimuthal variation of gradient in the $+-$ transition. Dotted curves are for abrupt transitions; solid curves are obtained with bevelled transitions.

curves are for transition pieces bevelled at 50° and the dotted curves are for an abrupt change from $+$ to $-$.

The C-section is stacked in a 90° sector, but due to the fringe fields at the ends of the quadrant the pole tips must occupy less than 90° of azimuth. A simple measurement in the synchrotron with A.C. excitation that can determine the place to end the pole tip stacking is shown in fig. 15. Two long, thin pickup coils

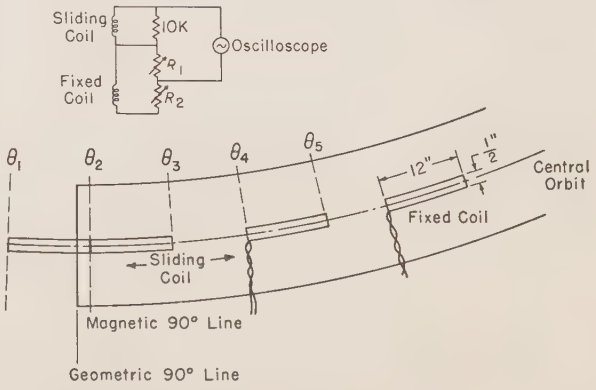

Fig. 15. Measurement of magnetic 90° azimuth.

are placed in the synchrotron gap at the same radius, one fixed and the other movable azimuthally. They measure $\int H\mathrm{d}\theta$, where θ is the azimuthal coordinate. Their signals are balanced in a bridge circuit and the ratio of the voltages induced in the two coils is measured. An azimuth θ_2 is determined such that

$$\int_{\theta_1}^{\theta_2} H\mathrm{d}\theta + \int_{\theta_2}^{\theta_3} H\mathrm{d}\theta = \int_{\theta_4}^{\theta_5} H\mathrm{d}\theta\,.$$

Position θ_4–θ_5 of the movable coil is well within the synchrotron gap where the field is constant with azimuth. θ_2 is then the magnetic 90° line. It is found that with the bevelled pieces used (bevelled to reduce eddy currents) the geometrical end of the quadrant comes at about 89° 20′.

The lens boundaries and the quadrant ends have all been measured and stacked in the synchrotron to an accuracy of about $\pm\frac{1}{32}''$ (two lamination thicknesses). Sellen[7]) has calculated that if all the quadrant ends were in error in the same direction by $\frac{1}{32}''$, this would result in the radial Q-value changing by 0.0006 and Q_v changing by 0.0022. The same error in the $+$ to $-$ transition would result in $\Delta Q_r = \Delta Q_v = 0.0066$. Referring back to fig. 3 it is clear that these errors are negligible.

12. Conclusion

The satisfactory design of the synchrotron magnet has been demonstrated by the acceleration of a stable beam of about 5×10^8 electrons per pulse to an energy of 1.2 GeV. The successful operation of the Cornell synchrotron testifies to the usefulness and convenience of alternate gradient focusing.

13. Acknowledgments

The Cornell Alternate Gradient Synchrotron and most of its principle design features were conceived by Professor R. R. Wilson. His advice and encouragement throughout the course of the pole tip design and magnetic measurements were invaluable.

Dr. H. Davis, Mr. D. Edwards, and Mr. D. Olsen worked on the pole tip design. We are indebted to them and to the late Mr. C. F. Van Amber and many members of his shop for their expert work on the various models and the synchrotron itself. We are grateful to Professor B. D. McDaniel, Dr. F. Amman, and Mr. G. Sacerdoti for their clever ideas and contributions to the success of this work.

NUCLEAR INSTRUMENTS AND METHODS 4 (1959) 79–89; NORTH-HOLLAND PUBLISHING CO.

EINE APPARATUR ZUR MESSUNG DER LONGITUDINALEN ELEKTRONENPOLARISATION DURCH MOTT-STREUUNG

H. BIENLEIN, K. GÜTHNER, H. VON ISSENDORFF und H. WEGENER

Physikalisches Institut der Universität Erlangen

Received 5 October 1958

The design of an apparatus for measuring the longitudinal electron polarization by Mott-scattering is described. Especially the following influences are pointed out: electron optical properties, depolarization by self-scattering in the source, passing through magnetic fields, perturbations by scattering from the walls, plural scattering in the scattering foil. The influences of asymmetries of the electron distribution and of finite spherical angles are discussed. As an example measurements with Co-60 are reported. The result is: full polarization — v/c within 2%.

1. Die grundsätzliche Versuchsanordnung

Die beim β-Zerfall auftretenden Elektronen sind wegen der Nichterhaltung der Parität[1,2]) longitudinal polarisiert[3]). Die Messung dieses Polarisationsgrades erlaubt Schlüsse auf die Kopplungskonstanten des β-Zerfalls und eventuell auf Matrixelemente. Insbesondere ist eine genaue Messung der Abhängigkeit des Polarisationsgrades P von der Elektronengeschwindigkeit v interessant. Von allen Methoden, die zur Messung der longitudinalen Elektronenpolarisation vorgeschlagen wurden (Mott-Streuung, Moeller-Streuung, Zirkularpolarisation der Bremsstrahlung, spezielle Methoden für Positronen durch Messung ihrer Vernichtungsstrahlung), ist wohl nur die Mott-Streuung geeignet, eine Präzisionsmessung der v/c-Abhängigkeit durchzuführen, da nur sie in dem Bereich, in dem sich v/c stark ändert, einen grossen polarisationsabhängigen Effekt zeigt.

Die Mott-Streuung[4,5]) zeigt für transversal polarisierte Elektronen eine azimutale Asymmetrie der Streuintensität. Will man den Polarisationsgrad longitudinal polarisierter Elektronen messen, so muss man zuerst die longitudinale Polarisation in eine transversale umwandeln. Eine Apparatur zur Messung der longitudinalen Elektronenpolarisation durch Mott-Streuung besteht somit aus drei wesentlichen Teilen:

(1) Der Quelle,

(2) Der Spinumlenkung,

(3) Dem Streuteil mit Nachweis.

Die bisher gebräuchlichen Apparaturen unterscheiden sich insbesondere in der Ausführung der Spinumlenkung. Man kann unterscheiden:

(a) Ablenkung durch makroskopische elektrische Felder,

(b) Ablenkung durch Vielfachstreuung[6,7]).

Wenn man genaue Messung der v/c-Abhängigkeit wünscht, muss man (a) wählen, da nur dort die Elektronenenergie definiert und die Spinumlenkung durchsichtig ist. Innerhalb dieser Methode kann man wieder unterscheiden:

(a) (α) Reine elektrostatische Ablenkung[8–12]),

(β) Geradeaus-Apparatur (Wienfilter)[13,14]).

[1]) O. Frisch and T. Skyrme, Progr. Nucl. Phys. **6** (1957) 267, Zusammenfassender Bericht.

[2]) H. Schopper, Fortschr. d. Phys. **5** (1957) 581. Zusammenfassender Bericht.

[3]) K. Hoffmann, Naturwiss. **45** (1958) 377. Zusammenfassender Bericht.

[4]) N. Mott and H. Massey, Theory of Atomic Collisions (Oxford, 1949).

[5]) H. Tolhoek, Revs. Mod. Phys. **28** (1956) 277.

[6]) J. Heintze, Z. Phys. **148** (1957) 560; **150** (1958) 134.

[7]) A. de-Shalit, S. Kuperman, H. Lipkin and T. Rothem, Phys. Rev. **107** (1957) 1459.

[8]) H. Frauenfelder, R. Bobone, E. v. Goeler, N. Levine, H. Lewis, R. Peacock, A. Rossi and G. De Pasquali, Phys. Rev. **106** (1957) 386; **107** (1957) 909.

[9]) H. de Waard and O. Poppema, Physica **23** (1957) 597.

[10]) N. Marty and H. Langevin-Joliot, Journ. Phys. Rad. **19** (1958) 28.

Für β spricht, dass man stets eine vollständige transversale Elektronenpolarisation erreichen kann und dass man die Apparatesymmetrie leichter testen kann. Nun ist aber ein vollständig transversaler Elektronenspin kein echter Vorteil gegen α, wo z.B. im Energiebereich zwischen 127 keV und 207 keV die Winkel nicht mehr als 6° von 90° abweichen. Da ausserdem nur der cos der Abweichung eingeht, macht eine Korrektion nicht mehr als 0.5% aus. Für α spricht die bessere Möglichkeit der Abschirmung unerwünschter Strahlung und die Ausnutzung der Abbildungseigenschaften des Ablenkfeldes.

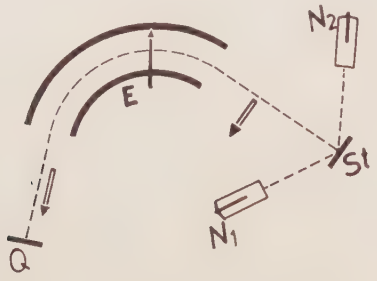

Fig. 1. Prinzip der Versuchsanordnung. Q = Quelle, $\boldsymbol{E}$ = elektrisches Ablenkfeld, St = Streufolie, N_1 und N_2 = Zähler, azimutal drehbar. Eingezeichnet ist die Bahn eines Sollelektrons mit Spinstellung. In der gezeichneten Zählerstellung verschwindet die Asymmetrie.

Im folgenden wird eine Apparatur nach (a) (α), also Spinumlenkung durch ein makroskopisches elektrisches Feld $\boldsymbol{E}$, beschrieben. Fig. 1 zeigt die prinzipiellen Teile dieser Apparatur. Es sind dies die Elektronenquelle Q, das elektrische Ablenkfeld $\boldsymbol{E}$, die Streufolie St mit den beiden Zählern N_1 und N_2, die starr verbunden sind und azimutal gedreht werden können. Eingezeichnet ist die Bahn eines "Sollelektrons" mit seinen Spinstellungen (wie sie bei Co-60 tatsächlich gefunden werden). Das Elektron verlässt das Präparat mit longitudinalem Spin. Im elektrischen Feld wird die Impulsrichtung des Elektrons gedreht, der Spin bleibt in klassischer Näherung erhalten, relativistisch erfolgt eine kleine Mitdrehung. Man findet[5])

$$\Delta\alpha = \Delta\gamma\, E_{\mathrm{kin}}/E \qquad (1)$$

$\Delta\alpha$ = Winkel der Spindrehung
$\Delta\gamma$ = Winkel der Impulsdrehung
E_{kin} = kinetische Elektronenenergie
E = Elektronengesamtenergie.

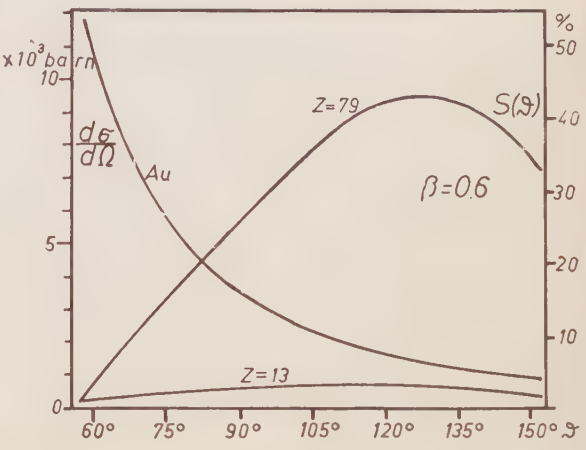

Fig. 2. Streuquerschnitt $d\sigma/d\Omega$ für Au und Asymmetriefunktion S für Au und Al der Mott-Streuung als Funktion des Streuwinkels für $v/c = 0.6$ (nach Sherman[15])).

Wird das Elektron um 120° umgelenkt, wird für Elektronen mit 170 keV kinetischer Energie der longitudinale Spin vollständig in einen transversalen verwandelt. Ferner wird durch das elektrische Feld die Elektronenenergie E_{kin} diskriminiert. Die nachfolgende Mott-Streuung erfolgt unter einem Streuwinkel von 120°. Bei Rückwärtsstreuung hat die Asymmetriefunktion S ein flaches Maximum (Fig. 2). Der grössere Wirkungsquerschnitt für Vorwärtsstreuung ist nur ein scheinbarer Vorteil, da dann sowohl S wie insbesondere $d\sigma_0/d\Omega$ stark vom Streuwinkel abhängen. Der differentielle Streuquerschnitt der Mott-Streuung ist[5]):

$$d\sigma/d\Omega = \{1 + S\,\boldsymbol{p}\cdot(\mathbf{t}_0 \times \mathbf{t}_1)/\sin\vartheta\}\, d\sigma_0/d\Omega \qquad (2)$$

[11]) M. Vishnevsky, V. Grigoriev, V. Ergakov, S. Nikitin, E. Pushkin and Y. Trebukosvsky, Nuclear Physics **4** (1957) 271.

[12]) H. Bienlein, R. Fleischmann and H. Wegener, Z. Phys. **150** (1958) 80.

[13]) P. Cavanagh, J. Turner, C. Coleman, G. Gard and B. Ridley, Phil. Mag. **2** (1957) 1105.

[14]) A. Alikhanov, G. Eliseiev, V. Liubimov and B. Ershler, Nuclear Physics **5** (1958) 588.

[15]) N. Sherman, Phys. Rev. **103** (1956) 1601.

$d\sigma_0/d\Omega$ = differentieller Streuquerschnitt
$S(\vartheta, Z, v/c)$ = Asymmetriefunktion
$\boldsymbol{p}$ = Vektor in Spinrichtung, Länge zwischen 0 und 1,
$\boldsymbol{t}_0, \boldsymbol{t}_1$ = Einheitsvektoren in Primär- und Sekundärrichtung,
$\boldsymbol{p}\cdot(\boldsymbol{t}_0 \times \boldsymbol{t}_1) = p \sin\vartheta \sin\varphi$,
φ = Azimut, gemessen von der Sollbahn-Ebene aus.

$$A = (1 + PS)/(1 - PS) \tag{4}$$

(sofern man den maximalen Effekt misst). Der Polarisationsgrad der Elektronen ist somit

$$P = \frac{1}{S}\frac{A-1}{A+1}. \tag{5}$$

Um keine falschen Streuasymmetrien zu bekommen, sollte die ganze Apparatur zu der Ebene senkrecht zur Streuebene des maximalen

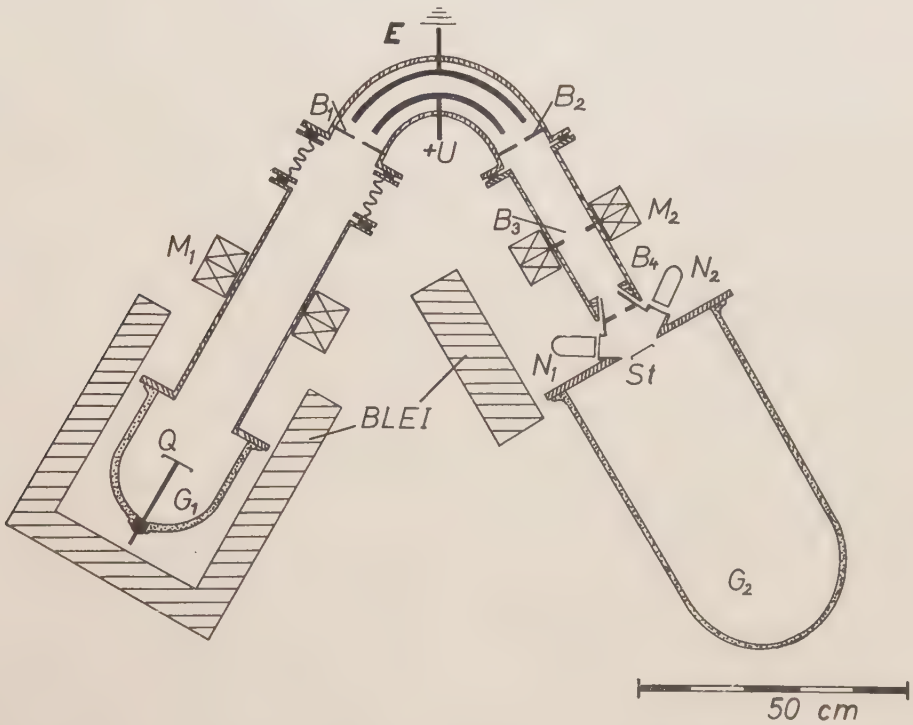

Fig. 3. Die Apparatur. Q = Quelle. $\boldsymbol{E}$ = elektrisches Feld, St = Streufolie, N_1, N_2 = Zähler, M_1, M_2 = magnetische Linsen, B_1 bis B_4 = Blenden. Die Apparatur ist aus Metall, G_1 und G_2 sind Glasglocken. Der Streu- und Nachweisteil ist azimutal drehbar.

Die Werte von $d\sigma_0/d\Omega$ und S entnimmt man den Tabellen von[15]) (Fig. 2). Man erkennt, dass der Wirkungsquerschnitt für transversal polarisierte Elektronen eine azimutale Asymmetrie zeigt. Sie verschwindet in der Zählerstellung der Fig. 1 und hat ihr Maximum, wenn die beiden Zähler senkrecht zur Papierebene stehen. Man misst die Zählraten N_1 und N_2, zieht den Nulleffekt ab und bildet daraus die Asymmetrie

$$A = \frac{N_2 - N_{2,0}}{N_1 - N_{1,0}}. \tag{3}$$

Der Formel für den Streuquerschnitt entnimmt man, dass andererseits gilt

Effektes symmetrisch sein, d.h. in Fig. 1 zur Ebene des Sollelektrons. Diese Ebene wird künftighin "Sollbahnebene" genannt werden.

Im folgenden werden Einzelheiten und Fehlerquellen der Versuchsanordnung diskutiert.

2. Beschreibung der Apparatur

2.1. PRINZIPIELLES

Fig. 3 zeigt die tatsächliche Anordnung. Die Quelle Q wird durch eine Magnetlinse M_1 in den Eingang des elektrischen Feldes abgebildet, gleichzeitig erfolgt eine Vordiskriminierung der Elektronenenergie E_{kin}. Das elektrische Feld $\boldsymbol{E}$

dreht den Spin (Formel (1)) und diskriminiert die Elektronenenergie. Die Magnetlinse M_2 bildet den Ausgang des elektrischen Feldes auf die Streufolie ab, diskriminiert E_{kin} nochmals und dreht den transversalen Elektronenspin. Sie wurde nicht stets verwendet. Die Blenden B_1 bis B_4 dienen der Begrenzung des Elektronenstrahls. Der mittlere Streuwinkel zu den beiden Zählern N_1 und N_2 beträgt 120°.

2.2. DAS ELEKTRISCHE FELD

Es wird ein 120°-Kugelfeld mit einem Plattenabstand $d = (15 \pm 0.1)$ mm, Radius der Sollbahn $R = (138 \pm 1)$ mm, Plattenhöhe $h = 70$ mm für die innere, 80 mm für die äussere Platte verwendet.

Energiediskriminierung des elektrischen Feldes: Die Energie der Teilchen auf der Sollbahn beträgt bei relativistischen Teilchenenergien

$$\varepsilon = \frac{eUR}{2d} + \left[(m_0c^2)^2 + \left(\frac{eUR}{2d}\right)^2\right]^{\frac{1}{2}} = m_0c^2 + E_{kin} \quad (6)$$

Wir haben die innere Feldplatte auf positive Hochspannung U gelegt, die äussere geerdet. Dadurch gewinnen die Sollelektronen der Quelle bis zum Feldeintritt noch $\frac{1}{2}eU$, sodass der Zusammenhang zwischen kinetischer Elektronenenergie und der angelegten (und gemessenen) Feldspannung U wird

$$E_{kin} = \frac{1}{2}eU\left(\frac{R}{d} - 1\right) + \left[(m_0c^2)^2 + \left(\frac{eUR}{2d}\right)^2\right]^{\frac{1}{2}} - m_0c^2 . \quad (7)$$

Dieser Energiewert ist auch bei Verwendung des Kugelfeldes in guter Näherung der Energie-Mittelwert der durchgelassenen Teilchen. Die Linienbreite beträgt $\Delta E_{kin}/E_{kin} = 4\%$, damit $\Delta\beta/\beta \approx 1\%$. Durch Streufelder an den Kondensatorrändern (oben und unten) können unerwünschte Linienverbreiterungen auftreten. Man vermeidet sie durch engen Plattenabstand und durch Anbringung der Blenden B_2 und B_1. Durch geeignete Anbringung von Elektroden könnte dieser Effekt sogar vollständig beseitigt werden[16]; es ist hier aber nicht von dringendem Bedürfnis.

[16]) R. Herzog, Z. Phys. **97** (1935) 596.

Durchlässigkeit des Feldes. Fig. 4 zeigt die Durchlässigkeit eines elektrischen Feldes in Abhängigkeit von der Feldform (Zylinder- oder Kugelfeld). Sie wurde durch Integration über alle zulässigen Elektronenbahnen gewonnen. Man erkennt daraus, dass der Kugelkondensator gegenüber dem Zylinderkondensator eine etwa 20% grössere Durchlässigkeit besitzt. Dies rührt her von den besseren (hier jedoch nicht

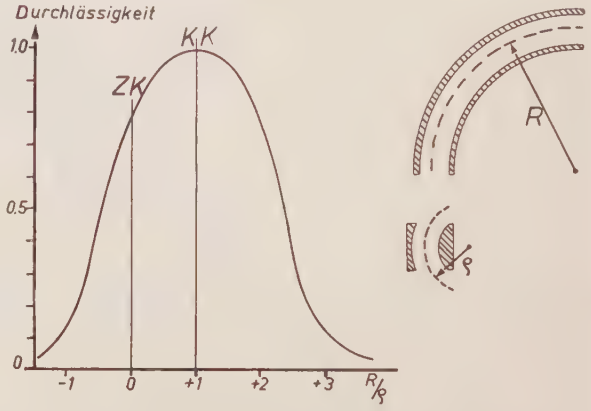

Fig. 4. Die Durchlässigkeit eines elektrischen Feldes in Abhängigkeit von der Feldform. $R/\sigma = 0$: Zylinderkondensator, $R/\sigma = 1$: Kugelkondensator.

voll ausgenutzten) Fokussierungseigenschaften des Kugelfeldes gegenüber dem Zylinderfeld.

Die Hochspannung wurde zur Vermeidung von Wanderwellen über einen Widerstand von 20 MOhm zugeführt. Es wurde mit Spannungen bis zu 50 kV gearbeitet. Um Feldemissionselektronen unschädlich zu machen, wurde nur positive Spannung angelegt, sodass die Feldemissionselektronen gegenüber dem Nachweisgerät keine Energie besitzen. Die Feldplatten wurden elektrolytisch vernickelt. Ein Vakuum von 10^{-4} Torr erwies sich als ausreichend (nach Einschalteffekten). Im allgemeinen betrug das Vakuum jedoch 10^{-5} Torr.

Bei Spannungen grösser 60 kV trat eine störende Röntgenstrahlung auf. Es wurde deshalb zunächst nur bei kleineren Spannungen gemessen.

2.3. MAGNETSPULE M_1

Es ist eine eisenfreie, wassergekühlte Magnetspule ohne Zentralblende. Sie bildet das Präparat

Q auf den Eingang des elektrischen Feldes 1:1 ab (Abstand Q/**E**: 61 cm). Damit wird Raum für die Unterbringung von Blei geschaffen. Man gewinnt durch die Linse einen Faktor 20 an Intensität. Es wurden die Elektronenbahnen berechnet und damit dann der Zusammenhang von der zur Abbildung gelangenden Elektronenenergie und dem Spulenstrom. Es ist wichtig, die Linse nach diesen berechneten Werten einzustellen, nicht nach dem Maximum der Durchlässigkeit der Kombination $M_1 + \boldsymbol{E}$. Grund: Wir befinden uns im abfallenden Ast des Spektrums. Die Linse kann eine grössere Zahl energieärmerer Elektronen in das Innere des **E**-Feldes abbilden. Dadurch wird die Linienbreite der durchgelassenen Elektronen in unerwünschter Weise vergrössert. Eine Beeinflussung des longitudinalen Spins erfolgt in M_1 nicht.

2.4. MAGNETSPULE M_2

Sie wurde nicht bei allen Messungen verwendet (der Abstand Ausgang des elektrischen Feldes–Streufolie betrug dann nur 26 cm). Sie ist prinzipiell gebaut wie M_1. Verwendet wurden zwei Typen, eine Einfachspule und eine Doppelspule mit gegensinnigen Stromrichtungen. Sie bildet den Feldausgang auf die Streufolie 1:1 ab (Abstand 41.5 cm) und bringt dabei einen Intensitätsgewinn um Faktor 4. Insbesondere verhindert sie das Auftreffen von Elektronen auf den Rahmen der Streufolie und setzt somit den Zähluntergrund herab. Die Elektronenbahnen wurden berechnet und die richtige Stromstärke danach eingestellt. Man bekommt noch eine empfindliche Diskriminierung der Elektronenenergie.

2.5. ZUSAMMENSETZUNG DER FELDER

Die Achsen der Magnetlinsen können durch Federkörper gegen die Eintritts- und Austrittsachsen des **E**-Feldes geneigt werden. Ferner kann das Präparat ($\varnothing = 25$ mm) in seiner Ebene bewegt werden. In Praxis erfolgt die Justierung so, dass man am Ausgang von **E** und am Ort der Streufolie bei ausgeschalteter M_2 ein mindestens zur Sollbahnebene symmetrische Elektronenverteilung hat. Die Verteilung wurde mit einem Zähler abgetastet. Aus den verschiedenen Messungen kann man schliessen, dass die Elektronenverteilung nach Ort und Geschwindigkeitsrichtung zur Sollbahnebene symmetrisch ist. Fig. 5 zeigt ein Beispiel, wo die Elektronenverteilung normal zur Sollbahnebene gemessen wurde (ohne M_2). Selbst bei idealer Justierung sind noch Unsymmetrien möglich. Wir verfolgen den Weg der kreisförmigen Elektronenverteilung

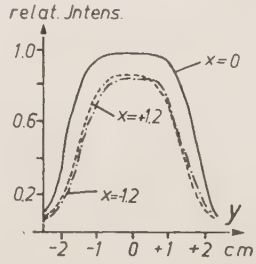

Fig. 5. Verteilung der Elektronenintensität am Ort der Streufolie ohne M_2. y = Koordinate seukrecht zur Sollbahnbene, x = Koordinate senkrecht zu y.

des Präparates. Im M_1 wird der Kreis in sich gedreht. In **E** wird die Elektronenverteilung deformiert, jedoch so, dass sie symmetrisch zur Sollbahnebene bleibt. Die Blende B_2 begrenzt das Bündel. Durch M_2 wird das Bild der Blende B_2 um

$$\varphi_0 = \frac{e}{2p} \int B \, dz \tag{8}$$

gedreht, die Drehung des transversalen Spins ist doppelt so gross wie die Bilddrehung. Deswegen wird die Symmetrieebene der Elektronenverteilung nicht mehr senkrecht auf der Streuebene des maximalen Effektes stehen. Das macht die Auswertung undurchsichtig. Man verwendet deshalb für M_2 Doppelspulen ohne resultierende Bild- und Spindrehung. Man braucht aber stärkere Felder, und bekommt dadurch Linsendrehfehler, die depolarisierend wirken können (§ 3. C).

2.6. STREUTEIL UND NACHWEIS

Dieser Teil besteht aus der Blende B_4, der Streufolie St, den beiden Zählern N_1 und N_2, sowie dem grossen Auslaufgefäss G_2 aus Glas. Er ist als ganzes azimutal drehbar. Als Streusubstanz diente meist Gold und Aluminium

(⌀ 45 mm). Die Streufolien sind spiegelglatt auf einem kreisrunden Aluminiumrahmen (⌀ 60 mm) gespannt. Sie wurden durch Aufdampfen auf 30 μg/cm²-Astralonfolien hergestellt, die vorher nach der üblichen Spreitungsmethode erzeugt und mit dem Al-Rahmen aus Wasser gezogen wurden. Es ist möglich, gleichzeitig vier Streufolien einzusetzen und sie nacheinander in den Strahlengang zu schwenken. Als Zähler dienen zwei 2 mg/cm²-Glimmer-Endfenster-Zählrohre. Vor den Zählern befinden sich zusätzlich 2–6 mg/cm² Al-Absorber, um die energetisch armen wandgestreuten Elektronen zu absorbieren. Folienwechsel und Teilchenzahlregistrierung erfolgten vollautomatisch. Messturnus 10 min.

2.7. AUSSCHALTUNG UNERWÜNSCHTER ELEKTRONEN

Sie wurden durch Blenden B_1 bis B_4 (Fig. 3) von der Streufolie ferngehalten. Man erreicht so, dass bei ausgeschaltetem Feld die Elektronenintensität auf 0.2% absinkt.

2.8. ABSCHIRMUNG DER GAMMASTRAHLUNG

Die direkte Strahlung wird durch 20 cm Blei und 85 cm Abstand abgeschirmt. Die Gammastreustrahlung beseitigt man dadurch, dass man das Präparat allseitig mit 10 cm Blei umgibt. Man kann sich davon überzeugen, dass die in der Apparatur von der Gammastrahlung ausgelösten Comptonelektronen ohne Bedeutung sind.

3. Fehlerdiskussion

Formel (5) gibt nur dann den richtigen Polarisationsgrad P, wenn das Präparat und die Streufolie unendlich dünn sind, wenn die Gefässwände nicht zurückstreuen und wenn alle gestreuten Elektronen Sollelektronen sind. Wir diskutieren sämtlich Abweichungen von diesem Idealzustand und ihre Folgen.

(3. A) Effekte, die schon bei einer hochsymmetrischen Apparatur auftreten. Gemeint ist eine Anordnung mit zwei gleichwertigen Zählern, einer überall gleichmässig dicken Streufolie und einer zur Bahn des Sollelektrons axialsymmetrischen Verteilung der auf die Folie fallenden Elektronen.

(3. Aa) Die endliche Präparatdicke führt zu einer Depolarisation durch Eigenstreuung im Präparat von z.B. 3%. Nähere Einzelheiten in § 4.

(3. Ab) Elektronen, die mit falschem Anfangsimpuls (Richtung und Energie) die Quelle verlassen und von den Gefässwänden in der Nähe der Quelle mit richtigem Impuls zurückgestreut werden, geben zu einem unpolarisierten Untergrund Anlass. Dank M_1, der grossen Glasglocke

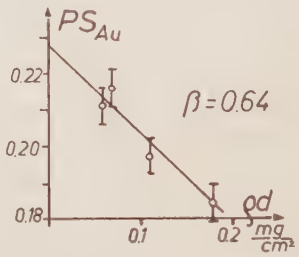

Fig. 6. Beispiel: Die nach (23) gemessene Asymmetrie $\overline{PS}_{Au}$ als Funktion der Streufoliendicke d. Um auf $d = 0$ zu extrapolieren, wurde durch die Messpunkte die beste Gerade gelegt. Der Anstieg dieser Geraden zo stimmt mit der theoretischen Erwartung[17]) überein.

G_1 und der Blende B_1 beträgt dieser Untergrund nur 0.3%.

(3. Ac) Die endliche Dicke d der Streufolie führt zu Störungen durch Zweifach- und Kleinwinkelstreuungen. Man muss daher auf $d = 0$ extrapolieren. Das ist experimentell (Messung mit verschiedenen d)[20]) und theoretisch[17]) möglich (Fig. 6). Ohne Beachtung von Ac) erhält man leicht z.B. um 10% zu geringe Polarisationsgrade.

(3. Ad) Elektronen mit folgendem Schicksal ergeben einen isotropen Zähluntergrund: Mott-Streuung von der Folie zur Gefässwand und von dort Rückdiffusion in die Zähler. Da dieser Effekt wegen der beteiligten Mott-Streuung gleich dem Solleffekt proportional zu d ist, lässt er sich durch eine $d \to 0$-Messung nicht erfassen. Er muss aus der Gefässgeometrie, dem Rückstreukoeffizienten des Wandmaterials und dem Energieverlust bei Rückstreuung in Verbindung

[17]) H. Wegener, Z. Phys. **151** (1958) 252.
[18]) B. Mühlschlegel and H. Koppe, Z. Phys. **150** (1958) 474.
[19]) C. Mohr and L. Tassie, Proc. Phys. Soc. A **67** (1954) 711.
[20]) H. Bienlein, Erlanger Dissertation (1958).

mit der Energieabhängigkeit der Zähler berechnet werden. Bei uns beträgt dieser isotrope Untergrund noch 2.5%, obwohl er durch die grosse Glasglocke G_2, kleine Rückstreuung des Wandmaterials (Glas, Plexiglas) und Energiediskriminierung der Elektronen möglichst klein gehalten wurde. Erste Messungen mit einem halb so grossen Gefäss zeigten 50% unerwünschte Elektronen.

(3. Ae) Unvollständige Spinumlenkung. Nach Durchlaufen des 120°-Ablenkfeldes steht der Spin, wie schon erwähnt, nur für 170 keV-Elektronen senkrecht zur Bahn. Für schnellere oder langsamere Elektronen ist nur die Komponente senkrecht zur Streuebene wirksam. Dadurch bedingte Korrektionen meist kleiner als 0.5%.

(3. Af) Endliche Öffnungswinkel. Die Bahnen und Spins der zur Streuung gelangenden Elektronen bilden ein ausgedehntes ($\varnothing = 3$ cm) pinselartiges Büschel (Öffnungswinkel bis zu $\pm 6°$). Die Zährohre werden von der Streufolie unter einem Raumwinkel von $\pm 12°$ gesehen. Mittelung über alle vorkommenden Winkel führt für die Stellung grösster azimutaler Asymmetrie zu einer scheinbaren Verminderung des Polarisationsgrades von z.B. 2%.

Sämtliche Effekte (Aa) bis (Af) verringern also die Asymmetrie und täuschen somit einen um z.B. 20% zu kleinen Polarisationsgrad vor.

(3. B) Effekte, die auftreten, wenn die Elektronenverteilung nicht mehr axialsymmetrisch sondern nur noch spiegelsymmetrisch zu einer Ebene ist, welche die optische Achse der zweiten Magnetlinse enthält. Betrachte dazu ein Elektron mit dem Polarisationsvektor $\boldsymbol{p}$, welches in Richtung $\mathbf{t}_0$ auf die Streufolie trifft und von dieser an der Stelle $\boldsymbol{r}_S$ gestreut wird. Die Schichtdicke des Streuers (Ordnungszahl Z, Atomzahl/Volumen n_z) betrage dort $d_z(\boldsymbol{r}_S) = \bar{d}_z\,(1 + \delta_z(\boldsymbol{r}_S))$ mit $\delta_z \ll 1$, $\bar{d}_z$ = mittlere Schichtdicke. Wir betrachten also den Fall nicht ganz einheitlicher Schichtdicke. Nach Streuung in Richtung $\mathbf{t}_1 = (\boldsymbol{r}_1 - \boldsymbol{r}_S)/|\,\boldsymbol{r}_1 - \boldsymbol{r}_S\,|$ trifft das Elektron den Zähler No. 1 an der Stelle $\boldsymbol{r}_1$. Die Nachweiswahrscheinlichkeit betrage hier $N_1(\boldsymbol{r}_1)$. Daneben haben wir den Zähler No. 2 mit $N_2(\boldsymbol{r}_2)$. Da sich beide Zählerstellungen stets nur im Azimut um 180° unterscheiden, darf man annehmen, dass $N_2(\boldsymbol{r}_2) = \text{konst.}$ $N_1(\boldsymbol{r}'_2)$ ist, wenn $\boldsymbol{r}'_2$ sich von $\boldsymbol{r}_2$ nur im Azimut um 180° unterscheidet. Den differentiellen Mott-Querschnitt (2) schreiben wir in der Form:

$$\frac{\mathrm{d}\sigma}{\mathrm{d}\Omega} = Z^2\, q_z\, r\,\{1 + S_z\,[\boldsymbol{p}\cdot(\mathbf{t}_0 \times \mathbf{t}_i)]/\sqrt{1 - \xi_i^2}\}\,. \quad (9)$$

mit $\xi = \mathbf{t}_0\,\mathbf{t}_i$, E = Elektronenergie, $r = r(\xi_i, E)$ = Rutherford-Querschnitt/Z^2 und $q_z = q_z(\xi_i,E)$ = $(\mathrm{d}\sigma_0/\mathrm{d}\Omega)/rZ^2$ ebenso wie $S_z = S_z(\xi_i,E)$ tabelliert bei Sherman[15]).

Die Verteilung aller die Streufolie treffenden Elektronen heisse $v(\mathbf{t},\boldsymbol{p},E,\boldsymbol{r}_S)$. Es seien $\mathbf{t}_0 = \mathbf{z}_0 + \delta\mathbf{t}_0$, $\boldsymbol{p} = p\mathbf{x}_0 + \delta\boldsymbol{p}$, $E = E + \delta E$, $\mathbf{t}_1 = \bar{\mathbf{t}}_1 + \mathrm{d}\mathbf{t}_1$ ($\bar{\mathbf{t}}_i$ = Einheitsvektor von der Streufolienmitte bis zur Mitte des i'ten Zählers), $\xi_i = \bar{\xi}_i + \delta\xi_i$ und v nur dann $\neq 0$, wenn die δ-Grössen klein sind.

Die Wahrscheinlichkeit dafür, dass ein Elektron im Zähler No. 1 nachgewiesen wird, lautet damit:

$$W_{1,z} = n_z\,\bar{d}_z\,Z^2 \int \mathrm{d}\mathbf{t}_0 \int \mathrm{d}\boldsymbol{p} \int \mathrm{d}E \int \mathrm{d}\boldsymbol{r}_S \int \mathrm{d}\boldsymbol{r}_1\, N_1(\boldsymbol{r}_1)$$
$$\cdot v\, q_z\, r\,(1 + \delta_z)\left\{1 + S_z\,\frac{\boldsymbol{p}\cdot(\mathbf{t}_0 \times \mathbf{t}_1)}{\sqrt{1 - \bar{\xi}_1^2}}\right\}. \quad (10)$$

Da $q_z = q_z(\xi_1,E)$ nur schwach veränderlich ist, entwickeln wir an der Stelle $\bar{\xi}_1,\bar{E}$:

$$q_z = \bar{q}_z\left\{1 + \left(\delta\xi_1\,\frac{\partial}{\partial\xi} + \delta E\,\frac{\partial}{\partial E}\right)\ln q_z \cdots\right\}. \quad (11)$$

Gemessen wird z.B. mit Streufolien aus Au und Al. Da die Sherman-S-Funktion für Al sehr klein ist (Fig. 2), gibt die Al-Messung Auskunft über apparative Asymmetrien. Bilde nun das Verhältnis der Nachweiswahrscheinlichkeiten

$$V(\varphi) = (W_{2,\mathrm{Au}}/W_{1,\mathrm{Au}})/(W_{2,\mathrm{Al}}/W_{1,\mathrm{Al}}) \quad (12)$$

Durch das Argument φ (= Azimut des Zählers No. 1) wird ausgedrückt, dass V natürlich φ-abhängig ist. Um die in $V(\varphi)$ enthaltene (sehr kleine) Aluminium-Mott-Asymmetrie zu eliminieren, bilde:

$$A(\varphi) = V(\varphi)\,\{1 + 2\,[S_{\mathrm{Al}}\,(V - 1)/S_{\mathrm{Au}}\,(V + 1)]\}. \quad (13)$$

Mit den Mittelwertsdefinitionen

$$< G >_i = \frac{\int \mathrm{d}\boldsymbol{t}_0 \int \mathrm{d}\boldsymbol{p} \int \mathrm{d}E \int \mathrm{d}\boldsymbol{r}_s \int \mathrm{d}\boldsymbol{r}_i N_i(\boldsymbol{r}_i)\, v\, r(\xi_i, E)\, G(\boldsymbol{t}_0, \boldsymbol{p}, E, \boldsymbol{r}_s, \boldsymbol{r}_i)}{\int \mathrm{d}\boldsymbol{t}_0 \int \mathrm{d}\boldsymbol{p} \int \mathrm{d}E \int \mathrm{d}\boldsymbol{r}_s \int \mathrm{d}\boldsymbol{r}_i N_i(\boldsymbol{r}_i)\, v\, r(\xi_i, E)} \tag{14}$$

und

$$< G > \equiv < G >_2 - < G >_1 \tag{15}$$

wird daraus bis zu einschliesslich linearen Gliedern in den kleinen δ-Grössen:

$$A(\varphi) = \Big\{ 1 + < \delta_{\mathrm{Au}} - \delta_{\mathrm{Al}} > + \Big(< \delta\xi > \frac{\partial}{\partial \xi} + < \delta E > \frac{\partial}{\partial E} \Big) \ln \frac{q_{\mathrm{Au}}}{q_{\mathrm{Al}}} \Big\} \cdot \frac{1 + < S_{\mathrm{Au}} [\boldsymbol{p} \cdot (\boldsymbol{t}_0 \times \boldsymbol{t}_2)] / \sqrt{1 - \xi_2^2} >_2}{1 + < S_{\mathrm{Au}} [\boldsymbol{p} \cdot (\boldsymbol{t}_0 \times \boldsymbol{t}_1)] / \sqrt{1 - \xi_1^2} >_1} . \tag{16}$$

Beachte bei der Auswertung der Mittelwertsintegrale, dass $\bar{\xi}_1 = \bar{\xi}_2 = \cos\vartheta$, da sich die beiden Zähler nur im Azimut unterscheiden. Zur weiteren Diskussion setze den Fall, dass die Elektronenverteilung nach Austritt aus dem elektrischen Feld hinsichtlich Ort, Impuls und Spin zur $\boldsymbol{x}_0$-$\boldsymbol{z}_0$-Sollbahnebene symmetrisch ist. Dass das bei uns zutrifft, wurde schon in Fig. 5 gezeigt. Die zweite Magnetspule dreht die Orts- und Impulsverteilung und deren Symmetrieebene je nach Stromrichtung um den bekannten Winkel $\varphi_0 = \pm\, |\, \varphi_0\, |$. Der Spin dreht sich aus der $\boldsymbol{x}_0$-Richtung um das Doppelte $2\varphi_0$, ist also nicht mehr symmetrisch zur Symmetrieebene verteilt. Dieser Symmetrieverlust bringt Komplikationen mit sich.

Um die in Zähler und Nenner von (16) auftretenden Mittelwertintegrale über S_{Au} zu berechnen, entwickeln wir $S_{\mathrm{Au}}(\xi) = S_{\mathrm{Au}}(\bar{\xi}) + (\partial S_{\mathrm{Au}}/\partial\xi)\, \delta\xi$ an der Stelle $\bar{\xi}$ und alle übrigen Grössen nach kleinen δ-Grössen. Das Resultat der einfachen aber etwas mühseligen Entwicklung lautet:

$$< S_{\mathrm{Au}} (\boldsymbol{p} \cdot (\boldsymbol{t}_0 \times \boldsymbol{t}_1)) / \sqrt{1 - \bar{\xi}_1^2} >_1 = P \Big[- \Big(S_{\mathrm{Au}} + < \delta\xi_1 >_1 \frac{\partial S_{\mathrm{Au}}}{\partial \xi} \Big) \sin(\varphi - 2\varphi_0) + S_{\mathrm{Au}} \Big\{ < \boldsymbol{y}_0, \frac{\delta \boldsymbol{p}}{P} >_1 \frac{1}{\cos 2\varphi_0} + \operatorname{ctg}\vartheta \Big(\boldsymbol{y}_0 \cos\varphi - \boldsymbol{x}_0 \sin\varphi, < \delta \boldsymbol{t}_0 - \frac{\delta \boldsymbol{t}_1}{\cos\vartheta} >_1 \Big) \Big\} \cdot \cos(\varphi - 2\varphi_0) \Big] . \tag{17}$$

Die entsprechende Grösse mit dem Index 2 folgt daraus durch die Ersetzung $1 \to 2$; $\varphi_0 \to \varphi_0$; $\varphi \to \varphi + \pi$.

Falls in (16) und (17) alle δ-Grössen verschwinden, lautet der Asymmetrieausdruck

$$A(\varphi) = \frac{1 + P S_{\mathrm{Au}} \sin(\varphi - 2\varphi_0)}{1 - P S_{\mathrm{Au}} \sin(\varphi - 2\varphi_0)} . \tag{18}$$

Davon abweichend treten folgende Fehler auf:

(3. Ba) Schichtdickenfehler $< \delta_{\mathrm{Au}} - \delta_{\mathrm{Al}} >$. Dieser Fehler verschwindet, wenn die Folien überall gleich dick sind. Ist jedoch z.B. die Hälfte der Au-Folie, die dem ersten Zähler näher als dem zweiten ist, um 10% dicker als die andere Hälfte, so werden in dem ersten Zähler apriori mehr Elektronen gestreut als in den zweiten, im Falle unserer Geometrie 3.5%. Da die Streufolie bis auf Feinheiten gleichmässig mit Elektronen bestrahlt wird und bei uns mit den Zählern gedreht wird, hängt $< \delta_{\mathrm{Au}} - \delta_{\mathrm{Al}} >$ nicht von φ ab.

(3. Bb) Relativistischer Fehler

$$\Big(< \delta\xi > \frac{\partial}{\partial \xi} + < \delta E > \frac{\partial}{\partial E} \Big) \ln \frac{q_{\mathrm{Au}}}{q_{\mathrm{Al}}} .$$

Dieser Fehler tritt auf, weil die Streuwahrscheinlichkeiten für Au and Al verschiedenartig von E und ξ abhängen. Der massgebliche Faktor $q_{\mathrm{Au}}/q_{\mathrm{Al}}$ kann aus Sherman[15]) entnommen werden. Obwohl er nur relativistisch $\neq 1$ wird, darf man die Grösse des (Bb)-Fehlers nicht unterschätzen. Man sieht leicht ein, dass die Mittelwerte $< \delta\xi > = < \delta\xi_2 >_2 - < \delta\xi_1 >_1$ und $< \delta E >$ verschwinden, wenn die Zähler symmetrisch zur Symmetrieebene der Elektronenverteilung aufgestellt sind. Der relativistische Fehler hat also die Form

$$\Big(< \delta\xi > \frac{\partial}{\partial \xi} - < \delta E > \frac{\partial}{\partial E} \Big) \ln \frac{q_{\mathrm{Au}}}{q_{\mathrm{Al}}} = \rho(\varphi) \cos(\varphi - \varphi_0) . \tag{19}$$

Im allgemeinen wird ρ noch von φ abhängen. Es nimmt leicht Werte von einigen Prozent an.

(3. Bc) Fehler, die in (17) neben S_{Au} auftreten. Sie gehören teilweise in die Gruppe (Af), da sie schon bei einer vollkommen symmetrischen Apparatur vorkommen können. Die mit dem Faktor $\cos(\varphi - 2\varphi_0)$ versehenen Fehler $< \delta \boldsymbol{p} >_1$, $< \delta \boldsymbol{t}_0 >_1$ und $< \delta \boldsymbol{t}_1 >_1$ rühren von den endlichen

Offnungswinkeln her. Sie verschwinden, wenn man $\cos(\varphi - 2\varphi_0) = 0$ macht.

(3. C) Folgerungen: Um mit einer solchen Apparatur genau messen zu können, hat man folgendes zu beachten: Der relativistische Fehler (19) verschwindet, falls $\varphi - \varphi_0 = \pm \frac{1}{2}\pi$, der Hauptfehler (Bc), falls $\varphi - 2\varphi_0 = \pm \frac{1}{2}\pi$, beide zusammen, falls $\varphi = \pm \frac{1}{2}\pi$ und $\varphi_0 = 0$ oder π.

Den Drehwinkel $\varphi_0 = 0$ erreicht man, wenn man auf die zweite Spule verzichtet oder die vorn erwähnte Doppelspule wählt. Für genaue Messungen arbeitet man besser ohne zweite Spule, da sie aus verschiedenen Gründen depolarisierend wirkt. Diese Gründe sind: (a) Elektronen, die durch die Randgebiete der Linse laufen, erleiden andere Spindrehungen als die Sollelektronen; (b) die Spindrehung ist für etwas verschieden schnelle Elektronen verschieden. (a) und (b) führen zu einer Verschmierung der Spinstellung. Nach vorläufigen Messungen wird dadurch die Polarisation scheinbar um 5% erniedrigt. Bei Absolutmessungen wird man deshalb auf Linse 2 verzichten. Bei Vergleichsmessungen—etwa zwischen zwei verschiedenen Quellen—kann man die Depolarisation zugunsten einer grösseren Streuintensität bei kleinerem Untergrund in Kauf nehmen.

Aus (17) folgt für die Messtellung $\varphi = \frac{1}{2}\pi$, $\varphi_0 = 0$:

$$< S_{Au} \sin\vartheta / \sqrt{1 - \tfrac{\xi_1^2}{2}} >_1 \frac{1}{2}$$

$$= \mp P \left(S_{Au} + < \delta\xi_1 >_1 \frac{\partial S_{Au}}{\partial \xi} \right) \equiv \mp P \bar{S}_{Au} \qquad (20)$$

$\bar{S}_{Au}$ muss berechnet werden. Da wir mit einem Streuwinkel $\vartheta = 120°$, also nahe beim Maximum von S_{Au} arbeiten, hängt $\bar{S}_{Au}$ wegen der Kleinheit von $\partial S/\partial\xi$ kaum von der genauen Form der Verteilung v ab, die ja den Wert von $<\delta\xi_1>_1$ bestimmt. Wir erhalten somit für die Asymmetrie:

$$A(\varphi = +\tfrac{1}{2}\pi) = \frac{1 + P\bar{S}_{Au}}{1 - P\bar{S}_{Au}} (1 + < \delta_{Au} - \delta_{Al} >) \qquad (21)$$

einen Ausdruck, der nur noch vom Schichtdicken-Fehler abhängt. Dreht man Streufolie und Zähler um π, so ergibt sich

$$A(\varphi = -\tfrac{1}{2}\pi) = \frac{1 - P\bar{S}_{Au}}{1 + P\bar{S}_{Au}} (1 + < \delta_{Au} - \delta_{Al} >) \qquad (22)$$

und daher

$$P = \frac{1}{\bar{S}_{Au}} \frac{\sqrt{A(\frac{1}{2}\pi)} - \sqrt{A(-\frac{1}{2}\pi)}}{\sqrt{A(\frac{1}{2}\pi)} + \sqrt{A(-\frac{1}{2}\pi)}} . \qquad (23)$$

Um die Fehler (Bb) und (Bc) zu eliminieren, mussten wir $\varphi_0 = 0$ (oder π) wählen, weil der transversale Spin und die örtliche Elektronenverteilung in einem Magnetfeld verschieden gedreht werden. Will man jedoch (etwa aus Intensitätsgründen) auf M_2 nicht verzichten, so bereitet die Auswertung einer Asymmetriemessung wegen (Bb) und (Bc) u.U. ernsthafte Schwierigkeiten. Die Auswertung wird jedoch leicht, wenn einerseits $\partial S/\partial\xi = 0$ und andererseits der Faktor ρ des relativistischen Fehlers (19) nicht von φ abhängt. Das kann in Sonderfällen zutreffen, z.B. bei einem homogenen aber etwas schräg auf die Folie treffenden Elektronenstrahl. In einem solchen Fall wählt man $\varphi - 2\varphi_0 = \pm \frac{1}{2}\pi$, damit der Fehler (Bc) verschwindet und misst mit zwei Drehwinkeln $\varphi_0 = \pm |\varphi_0|$ durch Wechsel der Stromrichtung in Spule M_2. Aus den vier Messgrössen $A(\varphi = 2\varphi_0 \pm \frac{1}{2}\pi;\ \varphi_0 = \pm |\varphi_0|)$ folgt dann wegen (16) und (17) der von den Fehlern (Ba), (Bb) und (Bc) unabhängige Ausdruck

$$\frac{1 + PS_{Au}}{1 - PS_{Au}} \qquad (24)$$

$$= \sqrt{\frac{A(2\varphi_0 + \frac{1}{2}\pi;\ +|\varphi_0|) + A(2\varphi_0 + \frac{1}{2}\pi;\ -|\varphi_0|)}{A(2\varphi_0 - \frac{1}{2}\pi;\ +|\varphi_0|) + A(2\varphi_0 - \frac{1}{2}\pi;\ -|\varphi_0|)}}$$

und daraus PS_{Au}, natürlich jetzt behaftet mit der durch M_2 verursachten, oben erwähnten Depolarisation.

4. Depolarisation in der Quelle

Das Präparat sei eine Schicht der Dicke t, der Dichte ρ, der Ordnungszahl Z, mit dem Atomgewicht A. Die Elektronen, die die Schicht in Richtung der Schichtnormalen $\mathbf{t}_0$ verlassen, haben 0, 1, 2... Grosswinkelstreuungen erlitten. Wir entwickeln den Polarisationsgrad P dieser Elektronen nach $(t\rho)$:

$$P = P_0 + P_1 (t\rho) + \cdots \qquad (25)$$

P_0 ist die Polarisation bei Entstehung des

Elektrons. Die Störung $P_1 t\rho$ soll berechnet werden. Da die Wahrscheinlichkeit für *eine* Grosswinkelstreuung proportional zu t ist, interessieren Elektronen mit zwei oder mehr Grosswinkelstreuungen nicht. Wir haben dann

(a) Elektronen, die fast in Richtung $\mathbf{t}_0$ erzeugt werden und durch Kleinwinkelstreuung die Richtung $\mathbf{t}_0$ erhalten.

(b) Elektronen, die in Richtung $\mathbf{t} \neq \mathbf{t}_0$ entstehen und durch eine Mott-Streuung nach $\mathbf{t}_0$ gestreut werden.

Die Gruppe (a) ist von Mühlschlegel und Koppe abgeschätzt worden[18]). Sie finden (im Original ist ein Druckfehler!)

$$\left\{\frac{P_1 t\rho}{P}\right\}_a = -0.38\,\frac{Z\,(Z+1)}{A}\left(1.1 + {}^{10}\lg\frac{t\rho\ (\mathrm{mg/cm^2})}{\beta^2}\right) \cdot \left(\frac{1-\beta^2}{\beta^2}\right)^2 \times 10^{-3}\, t\rho\ (\mathrm{mg/cm^2})\,. \qquad (26)$$

Die Gruppe (b) lässt sich mit der Methode[17]) des Konvergenz erzeugenden Faktors berechnen. Mit den Bezeichnungen aus[17]) schreibt sich die Wahrscheinlichkeit dafür, dass ein Elektron bei z_1 in Richtung $\mathbf{t}$ erzeugt und bei z_2 in Richtung $\mathbf{t}_0$ gestreut wird:

$$w = \frac{n_z}{t}\int_0^t \mathrm{d}z_1 \int_0^t \mathrm{d}z_2 \int_{\mathbf{t}\neq\mathbf{t}_0} \mathrm{d}\Omega(1)\, K\left(\frac{z_2 - z_1}{\mathbf{t}_0\,\mathbf{t}}, z_1\right) \sigma\,(\mathbf{t}\to\mathbf{t}_0)/|\,\mathbf{t}\,\mathbf{t}_0\,|\,. \qquad (27)$$

Wegen des δ-funktionsartigen Charakters von

$$\int \mathrm{d}z_1 \int \mathrm{d}z_2\, K/|\,\mathbf{t}\,\mathbf{t}_0\,| \approx f\,\delta\,(\mathbf{t}\,\mathbf{t}_0) \qquad (28)$$

wird daraus

$$w = 2\pi f\, n_z\, t\, \sigma\,(\mathbf{t}\to\mathbf{t}_0)_{\mathbf{t}\,\mathbf{t}_0=0} \qquad (29)$$

mit

$$f = 1.5 - 0.77\ {}^{10}\lg\,(2\lambda t) - 0.3\,\sqrt{2\lambda t}$$

aus [17]). Man hat also nur mit 90°-Streuung zu tun. Die Spinmitdrehung lässt sich nach Mühlschlegel und Koppe[18]) in Bornscher Näherung berechnen. Der Polarisationsgrad der 90°-Elektronen beträgt $P_0\beta^2/(2-\beta^2)$. Aus Wahrscheinlichkeit (29) und Polarisationsgrad der 90°-Streuung folgt mit $q = q_z(\xi = 0, E)$ aus (9):

$$\left\{\frac{P_1 t\rho}{P}\right\}_b = -0.30\, q\, f\,\frac{Z\,(Z+1)}{A}\left(\frac{1}{1-\beta^{\frac{3}{2}}}\right)\left(\frac{1-\beta^2}{\beta^2}\right)^2 \times 10^{-3}\, t\rho\ (\mathrm{mg/cm^2}). \qquad (30)$$

Ein Vergleich mit (26) zeigt, dass die Depolarisation durch 90°-Streuung meist erheblicher ist als die durch Kleinwinkelstreuung.

Als Beispiel betrachte eine von uns in dieser Form verwendete 90 mC- Co^{60}-Quelle (Fig. 7).

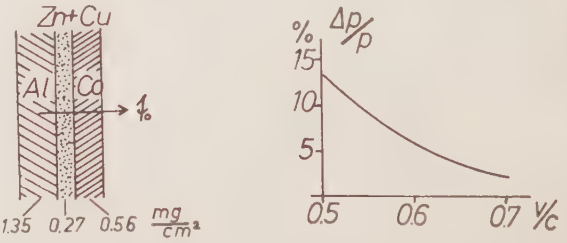

Fig. 7. Links: 90 mC-Co^{60}-Präparat auf Al + Cu + Zn-Unterlage. Rechts: Berechnete Depolarisation $\Delta P/P = -(P_1 t\varrho)/P$ durch Eigenstreuung in der Quelle für verschiedene v/c-Werte.

Für die Depolarisation durch Kleinwinkelstreuung (26) ist nur die Co-Schicht mit 0.56 mg/cm² massgeblich. Für $\beta = 0.5$ bis 0.7 erhält man Werte zwischen 3.6% und 0.36%. Die Depolarisation durch 90°-Streuung besorgt der ganze Schichtkomplex. Da Zn, Cu und Co etwa gleicher Z und A besitzen, dürfen wir sie zu einer Schicht der Dicke 0.83 mg/cm² zusammenfassen, in der das Co gleichmässig verteilt ist. Die für eine solche Schicht berechneten f-Werte liegen ($0.5 \leqslant \beta \leqslant 0.7$) zwischen 1.9 und 2.6, die daraus nach (30) resultierenden Depolarisationen zwischen 5.9% und 1.2%. Um den Einfluss der Al-Unterlage zu berücksichtigen, berechne man das Streuvermögen der Al-Schicht zu dem der 0.83 mg/cm²-Schicht für $\vartheta = 90°$. Man findet 72%. Unter den 90°-gestreuten Elektronen rühren also 72% vom Al her. Da der f-Wert für Al ebenfalls rund 2 ist, muss man die Depolarisation der 0.83 mg/cm²-Schicht noch um 72% vergrössern. In Fig. 7 ist die gesamte Depolarisation der Quelle als Funktion von β dargestellt.

5. Messungen an Co^{60}

Mit der beschriebenen Co^{60}-Quelle wurden Messungen durchgeführt. Wir geben ein Beispiel (ohne M_2):

Elektronengeschwindigkeit $v/c = 0.64$. Streufolien: (a) 30 μg/cm²-Astralon-Trägerfolie zur

Messung des Nulleffektes, (b) 1.5 mg/cm²-Al-Folie auf Trägerfolie zur Bestimmung der apparativen Asymmetrie, (c) 60 μg/cm² Au-Folie auf Trägerfolie. Gemessen werden in beiden Zählern $i = 1, 2$ der Nulleffekt $N_{i,0}$ sowie die Zählraten $N_{i,\mathrm{Al}}$ und $N_{i,\mathrm{Au}}$ für zwei Azimute $\varphi = +\frac{1}{2}\pi$ und $\varphi = -\frac{1}{2}\pi$. Aus den Zählraten bildet man

$$V(\varphi) = [(N_{2,\mathrm{Au}} - N_{2,0})\,(N_{1,\mathrm{Al}} - N_{1,0})]/[(N_{1,\mathrm{Au}} - N_{1,0})\,(N_{2,\mathrm{Al}} - N_{2,0})] \quad (31)$$

und daraus nach (13) die Grösse $A(\varphi)$. Aus A folgt nach (23) das Produkt $P\overline{S}_{\mathrm{Au}}$, das in unserem Fall nach einer Messzeit von 25 Std. z.B. $P\overline{S}_{\mathrm{Au}} = 0.211 \pm 0.005$ (statistischer Fehler) beträgt. Dieser Wert ist wegen der Fehler (Aa) bis (Af) zu korrigieren, die sich wie folgt zusammensetzen: (Aa) aus Fig. 7 = 4.0%; (Ab) = 0.3%; (Ac) aus [17]) und Fig. 6 = 6.4%; (Ad) = 2.5%; (Ae) = 0.0%; (Af) = 1.8%, soweit nicht in $\overline{S}_{\mathrm{Au}}$ berücksichtigt. Am ungenauesten sind die Fehler (Aa) und (Ac) abzuschätzen. Sie können nach [17]) bis zu 15% falsch sein, sodass die A-Korrektionen einen systematischen Fehler von 1.5% enthalten können. Die A Korrekturen erhöhen den $P\overline{S}_{\mathrm{Au}}$ Wert auf 0.245 ± 0.007 (Gesamtfehler). Zur Berechnung von $\overline{S}_{\mathrm{Au}}$ nach (20) dient Shermans Tabelle für $Z = 80$†. Das Resultat ist für $Z_{\mathrm{Au}} = 79$ um 2% zu erniedrigen. Man findet so $\overline{S}_{\mathrm{Au}} = -0.411$ und damit $P = -(0.93 \pm 0.03)\,v/c$.

In Tabelle 1 sind die Endresultate verschiedener Co^{60}-Messungen zusammengestellt. Für die grösste Energie finden wir volle Polarisation,

Tabelle 1

Energie	120 keV	155 keV	209 keV
$-P/(v/c)$	0.86 ± 0.02	0.95 ± 0.02	1.00 ± 0.02

für die kleinste Energie fehlen daran (14 ± 2)%, vorausgesetzt, dass die Sherman-Werte korrekt sind. Tatsächlich sind diese Werte aber ohne Berücksichtigung der Abschirmung durch die Hülle berechnet, die bei kleinen Energien die Asymmetrie beeinflussen muss. Mohr und Tassie[19]) finden für 120 keV-Elektronen bei $\vartheta = 120°$ eine Verminderung der S-Funktion um etwa 13%. Damit ergäbe sich auch bei unserem kleinsten Energiewert volle Polarisation.

Wir danken Herrn Professor Dr. R. Fleischmann für sein förderndes Interesse.

Die Deutsche Forschungsgemeinschaft und das Deutsche wissenschaftliche Committe der Research Corporation New York stellten Geräte zur Verfügung. Das Präparat fertigte die Fa. Buchler u. Co., Braunschweig.

† Die S-Funktion ist nur für Winkel in Abständen von 15° tabelliert. Die zur Berechnung von $\overline{S}$ nötigen Zwischenwerte lassen sich so schlecht interpolieren, dass $\overline{S}$ bis zu 0.8% falsch sein kann.

NUCLEAR INSTRUMENTS AND METHODS 4 (1959) 90–98; NORTH-HOLLAND PUBLISHING CO.

HOCHSTABILISIERENDE PROTONENRESONANZ-MAGNETFELDREGELUNG MIT ELEKTRONISCHEM INTEGRATOR

W. MÜLLER-WARMUTH und P. SERVOZ-GAVIN†

Max-Planck-Institut für Chemie, Mainz

Received 22 December 1958

The design, construction and performance of a precision magnetic field stabilizer for electromagnets supplied with line voltage is described. It includes a current stabilizer and a two-loop servosystem using nuclear magnetic resonance. One loop acts upon a correcting coil, the other drives the current stabilizer through an electronic integrator. Due to the second loop, the apparatus is a type-1 servosystem which cancels practically the steady-state error and keeps the velocity error constant, allowing very linear sweep of the field. The over-all system is studied in terms of servomechanisms theory. The final time stability is 10^{-7}. Together with the synchronised autodyn-detector we described in a previous paper[15]), this system affords a handy and flexible way to control, to measure, and to sweep magnetic fields from a standard frequency source.

1. Einleitung

In den letzten Jahren hat man dem Problem, sehr stabile magnetische Felder zu erzeugen und diese mit hoher Präzision zu messen, gesteigerte Aufmerksamkeit geschenkt. Besonders in der Kernphysik werden mehr und mehr Apparate benötigt, die homogene und stabile, möglichst genau bekannte Magnetfelder erfordern. Die Anforderungen sind im einzelnen natürlich sehr verschieden, was die Grösse dieser Felder, den überstreichbaren Bereich, ihre Stabilität, Homogenität, die Möglichkeiten einer sinusförmigen oder zeitlinearen Modulation u.s.w. anbetrifft. Es gibt jedoch eine Anzahl von Apparaturen, wie Massenspektrographen, Beschleuniger, Kernspektrometer etc., die mit Magnetfeldern von vielleicht 1000–10 000 G arbeiten, welche praktisch in der Bedienung sein und eine zeitlich Konstanz von—sagen wir—besser als 10^{-6} besitzen sollen. Für solche Fälle kann eine ziemlich allgemein anwendbare Lösung gefunden werden.

Zum Aufbau geeigneter Magnetfelder gehört die Auswahl des Magneten, seiner Speisung und des Stabilisierverfahrens. Bloom und Packard haben früher eine Übersicht über einige wesentliche hierfür gültige Gesichtspunkte gegeben[1]).

† Die vorliegende Arbeit enthält Teile der Dissertation von P. Sepvoz-Gavin (D 77).

Obwohl Permanentmagnete die höchste bis jetzt bekannte Stabilität ermöglicht haben[1,2]), sind ihre Anwendungsgebiete oft zu begrenzt, als dass man auf Elektromagnete verzichten könnte. Diese erlauben stärkere Felder, grössere Steuerbereiche, ihre Temperaturkoeffizienten sind kleiner und ihre Vorgeschichte lässt sich leichter beeinflussen, um homogene Felder herzustellen. Sie sind alles in allem vielseitiger in der Handhabung.

Als Stromquellen für die Erregerwicklungen der Elektromagnete kommen in erster Linie Batterien, Umformeraggregate und das Wechselstromnetz in Betracht. Die Benutzung von Akkumulatorenbatterien — Beispiele[8,11]) —

[1]) A. L. Bloom and M. E. Packard, Science **122** (1955) 738.

[2]) H. Primas and H. H. Günthard, Rev. Sci. Instr. **28** (1957) 510.

[3]) H. S. Sommers, P. R. Weiss and W. Halpern, Rev. Sci. Instr. **20** (1949) 244.

[4]) H. S. Sommers, P. R. Weiss and W. Halpern, Rev. Sci. Instr. **22** (1951) 612.

[5]) M. E. Packard, Rev. Sci. Instr. **19** (1948) 435.

[6]) N. T. van der Walt, Rev. Sci. Instr. **24** (1953) 413.

[7]) M. W. P. Strandberg, M. Tinkham, I. H. Solt and C. F. Davis, Rev. Sci. Instr. **27** (1956) 596.

[8]) H. A. Thomas, L. L. Driscoll, J. A. Hipple, J. Res. NBS **44** (1950) 569.

[9]) G. Lindström, Ark. Fys. **4** (1951) 23.

[10]) H. A. Thomas, Electronics **25** (1952) 114.

[11]) R. Beringer and M. A. Heald, Phys. Rev. **95** (1954) 1474.

scheint auf den ersten Blick eine ideale Lösung anzubieten. Im Falle grösserer Magnete muss man aber auch an die hohen Kosten, den ungeheuren Raumbedarf und die Wartung solcher leistungsfähigen Akkumulatoren denken. Motor-Generatoraggregate sind ebenfalls besonders nach den guten Ergebnissen von Sommers, Weiss und Halpern[3,4]) oft gebraucht worden, wie die Beispiele[10,14]) zeigen. Uns erschien die Speisung des Magneten aus dem Netz, die auch Packard bei der ersten Stabilisierung mit Kernresonanz anwandte[5]), nicht nur die billigste, sondern auch die einfachste Methode.

Zur Stabilisierung der Magnetfelder kommen verschiedene Verfahren in Frage. Ausser den klassischen Methoden, wie der Stromstabilisierung allein oder rotierenden Flussmessern mit Bezugsmagneten[6,7]), die eine für die hier aufgestellten Forderungen unzureichende Stabilität besitzen, sind in den letzten Jahren die zwei wichtigsten Methoden entwickelt und verfeinert worden: die Anwendung der magnetischen Kernresonanzphänomene[5,8–15]) und die Benutzung von Induktionsspannungen, die bei Flussänderungen in einer Empfängerspule induziert werden und mittels eines Integrators, eines Verstärkers und einer Kompensationsspule zur Regelung dienen[2,16]). Die Protonenresonanzstabilisierung dürfte bei sehr langsamen Drifts überlegen sein, die Induktionsspulenregelung für die Kurzzeitstabilität. Während die zweite Methode zu einer etwas besseren Endstabilität (10^{-8} anstatt 10^{-7}) führt[2]), besitzt ein mit Protonenresonanzregelung arbeitender Apparat für Allzweckmagnete jedoch den Vorteil, dass das Magnetfeld mit einem Frequenznormal jederzeit zugleich gemessen und gesteuert werden kann.

Diesen Überlegungen entsprechend haben wir uns bemüht, eine nicht zu komplizierte und vielseitig anzuwendende Methode zu entwickeln, die eine mit der Frequenz kontrollierbare relative Magnetfeldstabilität von etwa 10^{-7} gewährleistet. In früheren Arbeiten[12,15]) haben wir die Hauptmerkmale unsereres Apparates beschrieben, der inzwischen soweit vervollständigt und verbessert werden konnte, dass die erstrebte Stabilität erreicht wurde und eine etwas eingehendere Beschreibung gegeben werden kann. Wir benutzen eine Kombination von Stromregler und magnetischem Kernresonanzregler, die unabhängig voneinander arbeiten, direkt an das Wechselstromnetz anzuschliessen und einfach in der Bedienung sind. Wie wir gezeigt haben[15]), hängt die Genauigkeit des Verfahrens im wesentlichen von dem zur Verfügung stehenden Resonanzsignal, von der Wahl einer günstigen Übertragungsfunktion des Regelkreises und von der Konstanz der Hochfrequenz ab. Wir haben die Anwendung eines synchronisierten Autodyndetektors beschrieben, der zusammen mit einem Normalfrequenzgenerator die nötige Frequenzkonstanz sicherstellt und ausserdem auf einfache Weise erlaubt, von einem Feld (= Frequenz) wert auf den anderen überzugehen oder auch das Magnetfeld mit der Frequenz messbar zu steuern.

Zur Verwirklichung einer hohen Feldstabilität strebt man eine möglichst kleine Bandbreite des Kernresonanzsignales an. Selbst wenn es aber gelingt, gewisse experimentelle Schwierigkeiten zu überwinden und das Regelsignal aus einer äusserst engen Linie abzuleiten, muss man an die damit verbundene längere Relaxationszeit denken, die den Frequenzgang des Reglers begrenzt. Zu breite Linien ergeben andererseits unzureichende Signal-zu-Rausch-Verhältnisse, die letzten Endes ebenfalls das Frequenzverhalten verschlechtern. Wir haben eine Linienbreite von etwa 200 mG ($T_2 \approx 0.4$ msec bei 3 000 G), benutzt, die sich noch bei nicht allzuhohen Homogenitätsforderungen an Allzweckmagneten erzielen lässt. Die Empfindlichkeit genügt dann—wie die folgenden Abschnitte zeigen—ohne weiteres, um die Anforderungen an Regelfaktor und Frequenzgang zu erfüllen.

Das Blockschaltbild, Abb. 1, zeigt den

[12]) W. Müller-Warmuth, Physikal. Verhandl. 8 (1957) 32.
[13]) E. B. Baker and L. W. Burd, Rev. Sci. Instr. 28 (1957) 313.
[14]) H. Andresen, Z. Angew. Phys. 9 (1957) 326.
[15]) W. Müller-Warmuth and P. Servoz-Gavin, Z. Naturf. 13a (1958) 194.
[16]) C. Fric, Compt. Rend. 246 (1958) 3602.

vollständigen Apparat. Er besteht aus einem Stromstabilisator und einer Protonenresonanzregelung, die unabhängig voneinander arbeiten können. Zur Verbesserung des Gesamtverhaltens kann ein Integratorglied eingeschaltet werden, das beide Kreise verbindet. Die einzelnen elektronisch stabilisierten Netzgeräte sind nicht eingezeichnet. Das gleiche gilt für Wechselspannungsstabilisatoren, welche durch Heizspannungen verursachte Instabilitäten der Regelgeräte ausschliessen sollen.

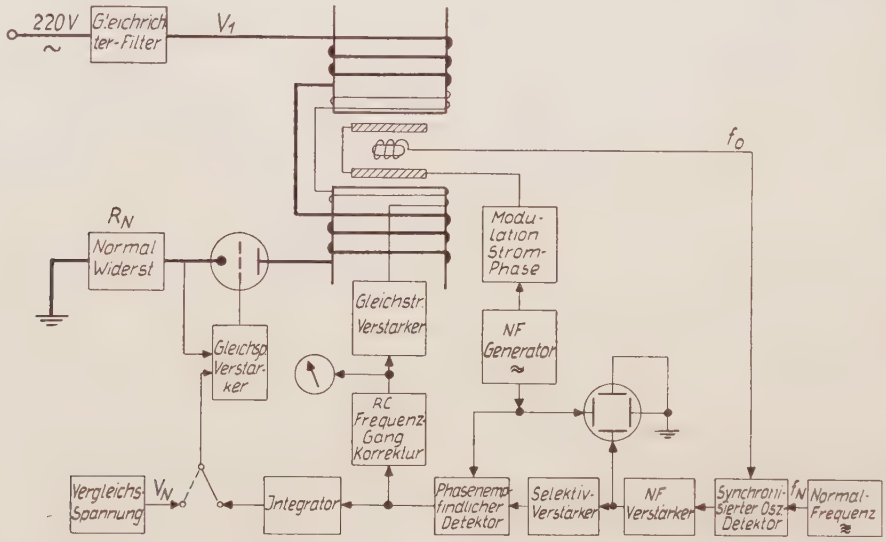

Abb. 1. Blockschaltbild der vollständigen Apparatur.

2. Der Stromstabilisator und die Einführung von Regelgleichungen

Zur Speisung des Magneten wird die 220 V-Netzspannung je nach Spannungsbedraf hochtransformiert und gleichgerichtet. Der durch *LC*-Filter gesiebte Gleichstrom durchfliesst nacheinander die Magnetwicklungen, eine Reihe parallel geschalteter Leistungsröhren und einen Standardwiderstand R_N. Dieser wurde aus Manganindraht von möglichst niedrigem Temperaturkoeffizienten selbstgewickelt, mit einer Reihe von Anzapfungen versehen und in Öl thermisch isoliert. Die an R_N abfallende Spannung wird mit einer Bezugsspannung (Glimmstabilisator 85 A2, von einem feinstabilisierten Netzgerät gespeist) verglichen und die Differenz nach Verstärkung zur Regelung benutzt (vgl. linker Teil von Abb. 1). Eine ganze Reihe von Stromstabilisatoren, die nach diesem oder ähnlichem Prinzip arbeiten, sind in der Literatur beschrieben worden[5,17–20]). Uns kam es darauf an, eine bestmögliche Stromstabilität mit einer einfachen Bedienungsweise zu verbinden. Die Grobeinstellung des Stromes geschieht durch einen Stufenschalter, der einen kleineren oder grösseren Teil von R_N kurzschliesst, die Feineinstellung durch ein Helipotpotentiometer, das den Spannungsabgriff einstellt.

Der in dieser Arbeit beschriebene Apparat wurde an einem 1.4 kW Massenspektrometermagneten erprobt, dessen Strom dabei von 50 bis 600 mA variiert werden konnte. Ähnliche Stromstabilisatoren wurden für andere Magnete gebaut, unter anderen für einen 24-Tonnen/2 kW-Magneten (10–2 500 mA), auf den jetzt auch die Protonenresonanzstabilisierung angewandt wird.

Das Regelverhalten soll, da es auch für das Folgende von Bedeutung sein wird, etwas genauer untersucht werden. Aus Abb. 2, die

[17]) I. Pelchowitch, Philips Research Rep. **9** (1954) 22.
[18]) R. J. Abraham, D. W. Ovenall, D. H. Whiffen, J. Sci. Instr. **34** (1957) 269.
[19]) V. P. Afanas'ev, Pribory i Tehk. Ekspt. (U.S.S.R.) **1** (1958) 59.
[20]) W. Müller-Warmuth, Z. Angew. Phys. **10** (1958) 497.

denselben Inhalt wie Abb. 1 in einem für die Regeltheorie praktischen Blockdiagramm wiedergibt, lässt sich das resultierende Magnetfeld $f_i(s)$ herleiten†. Dabei bleibt zu beachten, dass alle Übertragungsfunktionen F, f, α usw. im allgemeinen Funktionen der Laplace-Variablen s, also frequenzabhängig sind:

$$f_i = \frac{f_1 + \alpha f_r}{1 + \alpha}. \tag{1}$$

$f_1 = F_{s2} F_M V_1$ resultierendes Feld bei geöffneter Stabilisatorschleife

$f_r = (F_M/F_R) V_N$ Sollwert des Feldes (V_N Bezugsspannung)

$\alpha = F_{s1} \cdot F_{s2} \cdot F_R$ Übertragungsfunktion der geöffneten Schleife

$f_r - f_1$ ist die Abweichung vom Sollwert bei nicht ausgeregelten Stromschwankungen. Die durch verschiedene Einflüsse hervorgerufenen Feldänderungen werden durch den Stabilisator um den Regelfaktor

$$R_\alpha = \left| \frac{f_r - f_i}{f_r - f_1} \right| = \left| \frac{1}{1 + \alpha} \right| \tag{3}$$

geschwächt. Gegenüber Netzspannungsschwankungen wird dann also z.B. der Regelfaktor

$$R_\alpha^{V_1} = \frac{\Delta f_i / f_r}{\Delta V_1 / V_1} = \left| \frac{f_1}{f_r} \right| R_\alpha. \tag{4}$$

In Tabelle 1 sind die gemessen Zahlenwerte der Regelfaktoren für $s = 0$ zusammengestellt, mit denen sich jegliche relative Schwankungen des

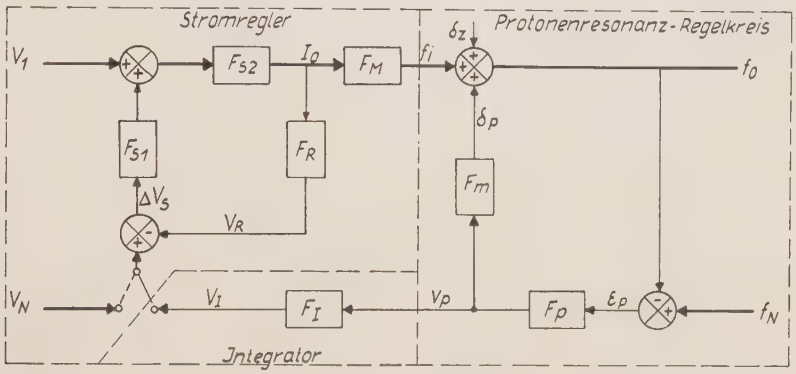

Abb. 2. Schematisiertes Blockdiagramm der Regler.

F_{s1} Übertragungsfunktion des Gleichspannungsverstärkers einschl. Stabilisierfilter

$$F_{s2} = \frac{1}{R_i + R_M + (\mu + 1) R_N} \frac{1}{1 + T_{s2} \cdot s}$$

Konduktanz des Magnetkreises (R_i Innenwiderstand, μ Verstärkungsfaktor der parallelgeschalteten Röhren; R_M Ohmscher Widerstand, T_{s2} Zeitkonstante des Magneten

$F_R = R_N$ Normalwiderstand

$F_M = f_i/I_0$ Umrechnung Strom in Feld.

Aus (1) folgt für die Abweichung vom Sollwert des Reglers

$$f_r - f_i = \frac{f_r - f_1}{1 + \alpha}. \tag{2}$$

† Die Magnetfelder werden hier grundsätzlich in Frequenzeinheiten gemessen. Aufgrund des gyromagnetischen Verhältnisses für Protonen gilt die Umrechnung 1 G = 4.258 kHz.

Netzes (V_1), der Belastung (R_M), der Bezugsspannung (V_N) und des Normalwiderstandes R_N multiplizieren

Tabelle 1

Regelfaktoren des Stromreglers

R_α	$R_\alpha^{V_1}$	$R_\alpha^{R_M}$	$R_\alpha^{V_N}$, $R_\alpha^{R_N}$
2.5×10^{-5}	8×10^{-6}	2×10^{-7}	1

Für das Verhalten gegenüber zeitlich schnelleren Änderungen wird in Abb. 3 die Dämpfungscharakteristik der Regelfaktoren gegeben, d.h. R_α und $R_\alpha^{V_1}$ in Dezibel als Funktionen der Frequenz. Man entnimmt diesen Kurven z.B., dass ein am Ausgang des Gleichrichtergerätes auftretender 100 Hz-Wechselsspannungsanteil

um 100 db geschwächt wird, um 70 db durch die Magnetwicklung und um 30 db durch den Regler. Der relative Brummanteil wird damit vernachlässigbar klein (5×10^{-8}).

Bei dem Entwurf von Geräten mit Rückkopplungsschleifen muss man besonders auf die Amplitude schneller als 12 db/Oktave abfällt. Für unseren Stromstabilisator hängt die Übertragungsfunktion neben Verstärkung und Frequenzgang des Reglers auch von der Zeitkonstante der Erregerwicklung des Magneten ab. Eine Untersuchung im angedeuteten Sinne

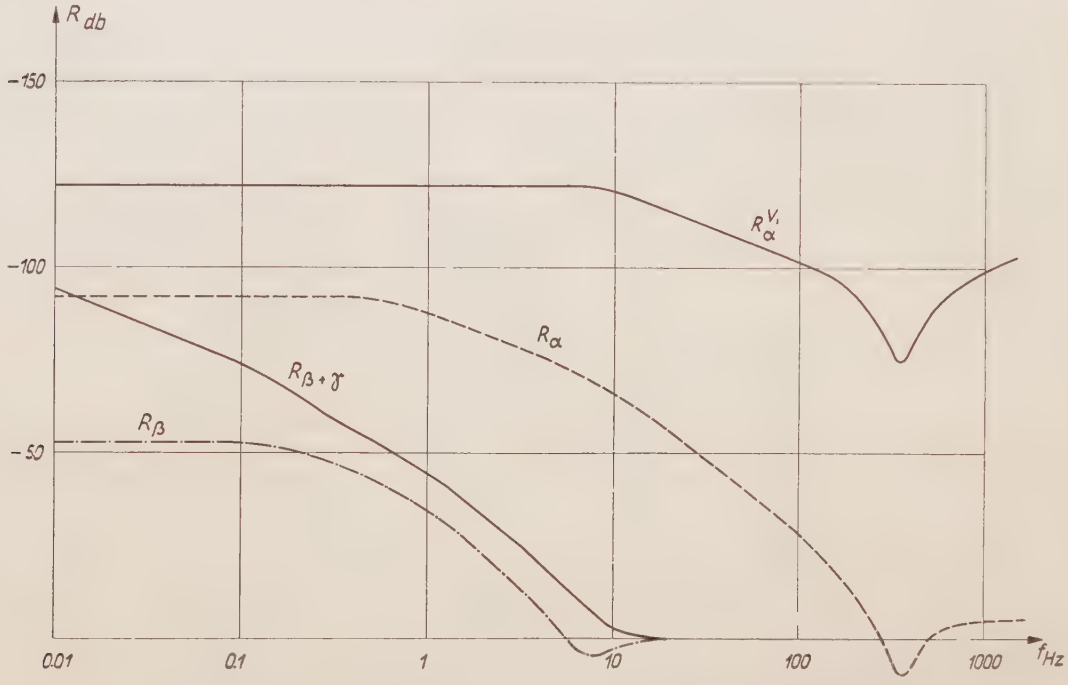

Abb. 3. Dämpfungschrakteristiken der im Text definierten Regelfaktoren.

eine Stabilität des Systems in sich bedacht sein. Entsprechend dem Nyquist-Kriterium darf die Über-alles-Übertragungsfunktion der geöffneten Schleife daher den Punkt (—1, 0) des Polardiagramms nicht einschliessen. Nach den Theoremen von Bode für "Phasenminimumsysteme"[21]) kann man eine äquivalente Aussage auch aus den Dämpfungscharakteristiken von Amplitude und Phase der Übertragungsfunktion entnehmen[22]). Der relative Phasenwinkel hängt eng mit dem Amplitudenabfall als Funktion der Frequenz zusammen. Das System ist instabil, wenn dieser Phasenwinkel für den Punkt der Einheitsamplitude kleiner als 180° ist, oder zeigte, dass bei unserem Magneten das System bei etwa 350 Hz schwingen könnte. Eine Unterdrückung dieser Schwingungen erfolgte durch geeignete Justierung eines Stabilisierfilters im Gleichsspannungsverstärker. Ähnliche Stabilitätsbetrachtungen waren für die Kernresonanzregelkreise erforderlich.

Die Messung der relativen Magnetfeldkonstanz aufgrund der Stromregelung erfolgte mit einem Protonenresonanzempfänger. Sie beträgt über mehrere Stunden 1.5×10^{-5}. Da die Regelfaktoren für Netzspannungs- und Belastungsschwankungen eine noch bessere Ausregelung dieser Einflüsse gewährleisten, dürften die verbleibenden Schwankungen seitens des Stromes vom Normalwiderstand R_N und von der Bezugsspannung V_N herrühren. Als Vorstabilisierung für unseren Protonenresonanzregler mit

[21]) H. W. Bode, Network Analysis and Feedback Amplifier Design (Van Nostrand Comp. New York, 1945).

[22]) H. Chestnut and W. Mayer, Servomechanism and Regulating System Design (Wiley and Sons, New York, 1955).

Integrator würde auch eine geringere Konstanz ausreichen. Jedoch gibt es Anwendungen mit einer Stromregelung allein, die schon relativ gut sein soll.

3. Die Protonenresonanzstabilisierung

Restliche Feldschwankungen auf grund der unzureichenden Stromkonstanz oder von Magnetfeldänderungen infolge direkter äusserer Einflüsse werden durch einen Protonenresonanz-

Abb. 2 die Regelgleichungen für den Protonenresonanzregelkreis (ohne Integrator)

$$f_0 = f_i + \delta z + \delta p = \frac{f_i + \delta z + \beta f_N}{1 + \beta}. \quad (5)$$

$f_N - f_0 = \dfrac{f_N - (f_i + \delta z)}{1 + \beta}$ bleibende Abweichung (6)

$f_i = \dfrac{f_1 + \alpha f_r}{1 + \alpha}$ vgl. (1), durch die Hauptwicklung erzeugtes Magnetfeld

δz durch direkte (thermische, mechanische) Einflüsse entstandenes (Stör-)Magnetfeld

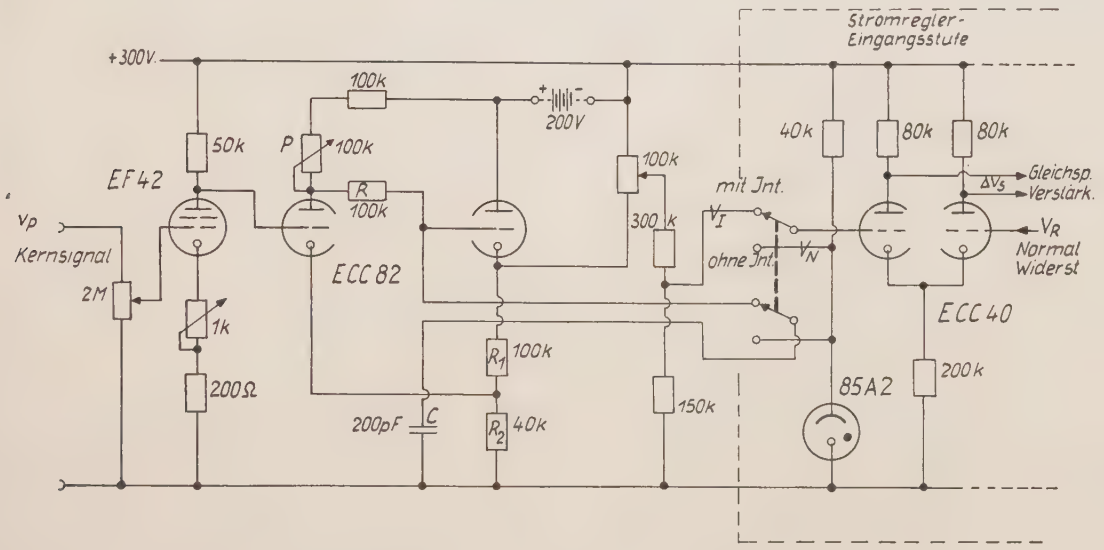

Abb. 4. Schaltung des Integrators mit Vorstufe und Eingangsteil des Stromreglers.

regelkreis korrigiert. Er besteht, wie man in den Abb. 1 und 2 sieht, aus zwei Schleifen. Eine 0.2 cm³-Wasserprobe, die einige Kupferionen enthält, befindet sich an einer homogenen Stelle des Spaltes. Die Niederfrequenzmodulation sehr kleiner Amplitude liefert am Ausgang der Detektorstufe ein differenziertes Absorptionssignal. Dieses wird in bekannter Weise verstärkt und mittels eines phasenempfindlichen Empfängers in eine Gleichspannung v_P umgewandelt. In der ersten Rückkopplungsschleife erzeugt dieses Signal einen Regelstrom, der über eine Hilfsspule von wenigen Windungen auf das Feld einwirkt. In einer zweiten Schleife regelt v_P über einen elektronischen Integrator und über den Stromstabilisator das Magnetfeld.

Wie beim Stromstabilisator ergeben sich aus

δp durch die Regelung erzeugtes Korrekturfeld

f_N Sollwert des Feldes (Normalfrequenz)

$\beta = F_P F_m$ Übertragungsfunktion der offenen Schleife (F_P Produkt der Übertragungsfunktionen der in Abb. 1 gezeichneten Einzelglieder einschl. der des Signals, F_m Übertragungsfunktion der Endstufen einschl. Hilfswicklung).

Aus (6) folgt der Regelfaktor

$$R_\beta = \left| \frac{1}{1 + \beta} \right|, \quad (7)$$

dessen Dämpfungscharakteristik in Abb. 3 dargestellt worden ist. Der Messwert $|\beta| = 450$ im stationären Zustand hängt natürlich stark von der Linienbreite des Signals und anderen experimentellen Voraussetzungen ab. Er ist aber auch der grösstmögliche Verstärkungswert, oberhalb dessen das System zu Oszillationen bei

ungefähr 10 Hz neigt. Um die Stabilität der Schleife zu verbessern, wurde ein Korrekturfilter eingeführt, der am Punkt $|\beta| = 1$ etwa 20° zum Phasenwinkel von β addiert. Eine weitergehende Korrektur würde den effektiven Frequenzbereich verkleinern, der jetzt bis 1 Hz geht und den Regelfaktor dann im Verhältnis von ungefähr 10 db/Oktave abfallen lässt.

Der elektronische Integrator der zweiten Schleife, dessen Schaltbild in Abb. 4 gegeben ist, kommt einer perfekten Integration sehr nahe. Sein Ausgang ist für den Nulleingang auf 85 V eingestellt, um bei eingeschalteter Schleife anstelle der Bezugsspannung V_N den Stromstabilisator zu steuern. Bevor man den Kreis anschaltet, wird der Kondensator C auf einen Wert aufgeladen, der die 85 V-Ausgangsspannung erzeugt. Die Zeitkonstante des Kreises $T = RC$ lässt genügend Spielraum, um das Resonanzsignal zu suchen und den Protonenresonanzregelkreis zu schliessen. Das ist um so leichter, als die erste Schleife, die man vorher geschlossen hat, das Feld schon festhält.

Wenn man die Vorwärtsverstärkung dieses Integrators a nennt und $k = R_2/(R_1 + R_2)$ den Anteil der Ausgangsspannung, der positiv zurückgekoppelt wird, ergibt sich die Übertragungsfunktion

$$F_I = \frac{a}{1 - ak + T \cdot s}.$$

Für $a = 1/k$ liegt der Fall vollständiger Integration vor, die mit dem Potentiometer P eingestellt wird

$$F_I = \frac{1}{T_I \cdot s}, \qquad T_I = kT = 7 \text{ sec}. \tag{8}$$

Die Wirkungsweise der zweiten Schleife versteht sich aus den Regelgleichungen. Die Übertragungsfunktion bei geöffneter Rückkopplungsschleife ist (Abb. 2)

$$\gamma = F_P F_I \frac{F_M}{F_R} \frac{\alpha}{1 + \alpha} \approx F_P F_I \frac{F_M}{F_R}. \tag{9}$$

Da F_I einen Pol im Ursprung besitzt, haben wir es hier mit einem "Regler vom Typ 1" zu tun, bei dem die Verstärkung im stationären Betrieb praktisch unendlich ist und bei dem keine Regelabweichung zurückbleibt. Mit den Bezeichnungen α, β, γ lässt sich anstelle von Abb. 2 das stark vereinfachte Blockdiagramm Abb. 5 zeichnen. Daraus ergibt sich

$$f_0 = \frac{f_1/(1 + \alpha) + \delta z + (\beta + \gamma) f_N}{1 + \beta + \gamma} \tag{10}$$

und

$$f_N - f_0 = \frac{f_N - (f_1/(1 + \alpha) + \delta z)}{1 + \beta + \gamma}. \tag{11}$$

Der Regelfaktor der vollständigen Kernresonanzstabilisierung für alle Änderungen, die am

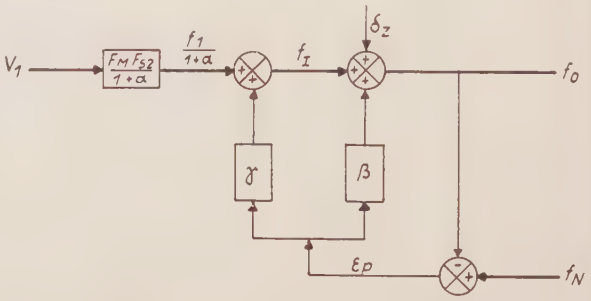

Abb. 5. Vereinfachtes Blockdiagram des Gesamtregelsystems.

Orte der Probe auf das Feld einwirken, ist damit

$$R_{\beta+\gamma} = \left| \frac{1}{1 + \beta + \gamma} \right|. \tag{12}$$

Seine Dämpfungscharakteristik wurde ebenfalls in Abb. 3 eingetragen, wie sie sich aus den experimentellen Werten der einzelnen Parameter ermitteln liess. Die Unvollständigkeit der Integration—der stationäre Wert für $|\gamma|$ ist nicht ganz unendlich—dürfte vernachlässigbar klein sein, da wir selbst für sehr grosse Änderungen der Eingangsgrössen keine bleibende Abweichung messen konnten. Bis etwa 0.2 Hz besteht eine gegenüber R_β wesentlich verbesserte Regelung. Man sieht aus der Darstellung von $R_{\beta+\gamma}$ selbst für höhere Frequenzen einen um etwa 12 db gestiegenen Verstärkungswert, der "cut-off-Punkt" ist von 6 auf 14 Hz verschoben. Eine theoretische Untersuchung zeigt, dass der Integrator für niedrige Frequenzen zwar den Phasenwinkel der vollständigen Übertragungsfunktion um 90° verschiebt, dass bei der Zweischleifenstabilisierung dieser Einfluss mit wachsenden Frequenzen aber immer kleiner wird. Trotz erhöhter Gesamtverstärkung genügt

daher eine ähnliche Phasenkorrektur wie für R_β allein, die bei etwa 10 Hz wirksam wird, um das Gesamtsystem gegen Schwingungen stabil zu machen; man kann sagen, die beiden Schleifen stabilisieren sich gegenseitig. Experimentell konnten wir Entsprechendes beobachten. Langsame Schwankungen werden—um es anders auszudrücken—direkt mittels der Integratorschleife korrigiert, schnelle Änderungen zunächst über die Hilsspule mit der kürzeren Zeitkonstanten, dann werden sie in der zweiten Schleife integriert.

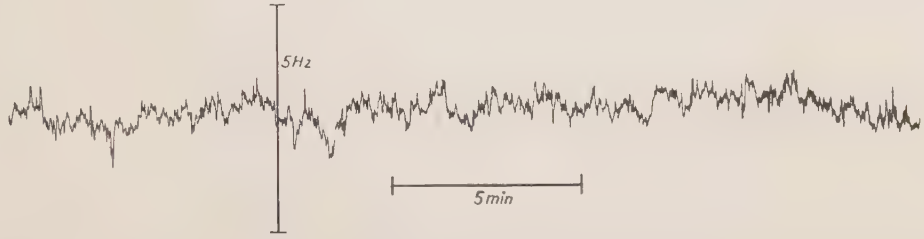

Abb. 6. Ausschnitt aus einer bei 10 MHz registrierten Magnetfeldmessung mit Protonenresonanz (Zeitkonstante des Messempfängers 0.7 sec) zur Kontrolle der Stabilität.

4. Experimentelle Ergebnisse

Das kombinierte Regelsystem wurde nach dem Gesichtspunkt aufgebaut, höchste Magnetfeldstabilität mit der Möglichkeit zu verbinden, die Feldwerte ohne allzuviel Mühe in weiten Bereichen zu verändern. Die Einschaltung gestaltet sich denkbar einfach, da der Stromstabilisator das Feld schon innerhalb enger Grenzen festhält. Nach Auffinden der Protonenresonanz schliesst ein Schalter den Regelkreis β, ohne die α-Regelung zu beeinflussen. Schliesslich kann die Schleife γ geschlossen werden, wie es vorher beschrieben wurde. Danach bleibt bei schon vorhandener Regelung noch die Feineinstellung aller Regeleigenschaften wie Modulationsphase, Verstärkungen und Stabilität gegenüber Schwingneigung, was anhand von eingebauten Messinstrumenten und Oszillographen geschieht. Zum Übergang auf einen in der Nähe liegenden Feldwert braucht nui der Sollwert f_N geändert zu werden, also die Einstellung des Normalfrequenzgenerators zusammen mit dem Oszillator. Die Integratorschleife bietet dabei den Vorteil, dass man das Feld bis zu 30% durch f_N allein steuern kann, wenn der Frequenzbereich des Probenkopfes es zulässt.

Um wirklich die hohe Endstabilität des Magnetfeldes zu erreichen, welche die Regelfaktoren erwarten lassen, müssen externe Störungen wie Streufelder von Transformatoren nahe am Magneten und starke Hochfrequenzfelder im Bereiche der Protonenfrequenz vermieden werden. Es ist ferner zu bedenken, dass die vollständige Ausregelung aller Schwankungen nur am Orte der Probe erfolgt. Bei ausgedehnteren Magnetfeldern können sich äussere Kräfte, bewegte Metallgegenstände im Raum und zeitliche Temperaturschwankungen verschieden auf den Ort der Stabilisierung und den einer beliebigen Messstelle auswirken. Dann bleibt die Regelung unvollständig.

Zur Überprüfung der im Endeffekt erreichten Magnetfeldstabilität wurde eine empfindliche Messapparatur aufgebaut, die auch mit Protonenresonanz oder mit Fluorresonanz arbeitete. Ihre Frequenz war ebenfalls synchronisiert (Stabilität besser als 10^{-7}) und auf 0.5 Hz (das entspricht etwa 0.1 mG) genau einstellbar. Das Gleichstromsignal am Ausgang des Empfängers wurde registriert. Durch Verändern der Normalfrequenz um einige Hertz konnte—nachdem der Messoszillator auf das Zentrum der Absorptionskurve eingestellt worden war—ein Eichsignal gewonnen werden. Abb. 6 zeigt einen Ausschnitt aus der auf diese Weise gemessene Stabilitätskurve. Die relative Stabilität beträgt für einige Minuten 10^{-7} und ist für eine halbe Stunde nur wenig schlechter. Für viele Stunden blieb das Feld auf 2 bis 3×10^{-7} konstant. Aus experimentellen Gründen waren Stabilisierprobe und Messprobe bei diesen Messungen etwa 30 cm voneinander entfernt im Magnetfeld

untergebracht. Daher musste besonders auf die oben erwähnten Voraussetzungen für räumlich ausgedehnte Magnetfelder geachtet werden. Kleine Änderungen des thermischen Gleichgewichtes im Laborraum vermochten schon das Ergebnis zu beeinträchtigen. Bei einer grösseren Entfernung zwischen den beiden Probenköpfen ergaben sich keine so guten Messergebnisse, zumal wir keine besonderen Massnahmen zur Temperaturkonstanthaltung des Magneten getroffen hatten.

Um mit der Stabilität zugleich auch die Linearität einer Steuerung des Magneten zu prüfen, haben wir mit einem Servomotor die Normalfrequenz f_N des Regelsystems langsam geändert. Über die Regelschleifen wurde somit das Feld zeitlinear und messbar verändert. Die Frequenz des zweiten Empfängers war vorher so eingestellt worden, dass sich im Verlaufe dieser Abtastung (4 kHz/Stunde) die Ableitung der ^{19}F-Resonanzlinie registrierte (Abb. 7). Für eine zeitlineare Änderung der Eingangsgrösse bietet der "Reglertyp 1" den besonderen Vorteil, dass der restliche Fehler der Ausgangsgrösse konstant, also die Linearität einer Feldsteuerung erhalten bleibt. Das ist bei dem sonst üblichen Protonenresonanzregelsystem, das zum "Typ 0" gehört, ebenso wie das Verschwinden eines Fehlers im stationären Betrieb, nicht der Fall.

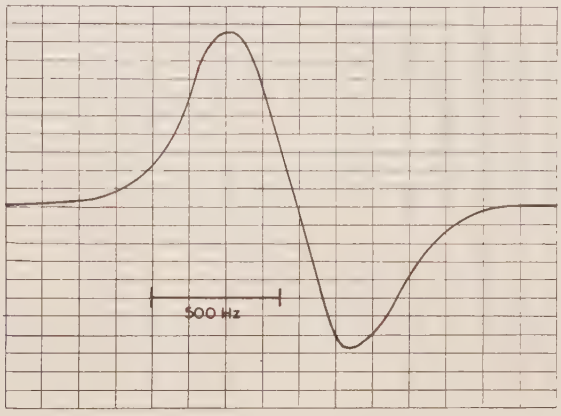

Abb. 7. Registrierte Ableitung einer ^{19}F-Resonanzabsorption bei langsamer Feldabtastung zur Kontrolle der Stabilität und der Linearität einer Steuerung (Unsymmetrien der Kurve sind auf unzureichende Homogenität des Magneten zurückzuführen, der nicht für Kernresonanzuntersuchungen vorgesehen war).

Für die grosszügige Förderung unserer Arbeiten möchten wir Herrn Prof. Dr. J. Mattauch aufrichtig danken.

NUCLEAR INSTRUMENTS 4 (1958) 99–102; NORTH-HOLLAND PUBLISHING CO. – AMSTERDAM

GAS SCATTERING IN A STRONG FOCUSING SYNCHROTRON

MORTON D. KOSTIN

Cambridge Electron Accelerator†, Massachusetts Institute of Technology and Harvard University, Cambridge, Massachusetts

Received 25 October 1958

Strong focusing synchrotron dynamics as they apply to gas scattering are discussed. The gas scattering transport equation which includes the effects of adiabatic damping is formulated. A practical method of obtaining the solution is developed.

1. Introduction

Gas scattering in synchrotrons have been treated by several authors[1–4]). In this paper we will develop a practical and systematic method of determining the gas scattering losses for an arbitrary initial distribution and an arbitrary acceleration cycle.

It is assumed that the reader is familiar with the strong focusing synchrotron paper by Courant and Snyder[5]). In general, we will use the nomenclature given in their article.

2. Betatron Oscillations

The salient features of strong focusing synchrotron dynamics as they apply to the problem of gas scattering will be considered first. A system of curvilinear coordinates is established:

s = distance along equilibrium orbit,
y = either horizontal or vertical displacement from equilibrium orbit.

A prime $'$ indicates differentiation with respect to s.

Consider a two-dimensional phase space with coordinates y and y'. At a given position s, a relation exists between the y and y' coordinates of a particle.

$$W = \frac{1}{\beta}[y^2 + (\alpha y + \beta y')^2] = \gamma y^2 + 2\,\alpha y y' + \beta y'^2$$

where α, β, γ are functions of s and are determined by the elements of the $M(s + L,s)$ matrix. L is the length of a unit cell. W is a constant independent of s. (For the moment we neglect adiabatic damping.)

Relation (1) is the equation of an ellipse. If we think of a three dimensional phase space with coordinates y, y', and s we can imagine a tubular elliptical surface whose axis coincides with the s axis. Any section perpendicular to the s axis is an ellipse which bounds a constant area equal to πW. W will be called the betatron area.

If only betatron forces are present then the trajectory of a particle will be entirely confined to the tubular elliptical surface.

The limiting elliptical tubular surface is determined by the dimensions of the vacuum chamber. The value of W corresponding to the limiting elliptical tubular surface is designated by the subscript $_L$.

2.1. ADIABATIC DAMPING

As the particle momentum increases, the value of W decreases accordingly to the relation $W = W_0/u$ where $u = p/p_0$ is the normalized momentum. The subscript $_0$ denotes quantities at the beginning of the acceleration cycle.

† This work supported by U. S. Atomic Energy Commission.

[1]) N. M. Blachman and E. D. Courant, Phys. Rev. **74** (1948) 140.
[2]) N. M. Blachman and E. D. Courant, Phys. Rev. **75** (1949) 315.
[3]) M. J. Moravscik and J. M. Sellen, Jr., Rev. Sci. Instr. **26** (1955) 1158.
[4]) R. J. B. Hadden, A.E.R.E., GP/R 2189, (1957).
[5]) E. D. Courant and H. S. Snyder, Ann. Phys. **3** (1958) 1.

If we think of particles with the same value of W as equivalent, then a particle can be characterized by the (W, u) pair.

2.2. SCATTERING

When a particle engages in a scattering its value of y' suddenly changes, while y and s remain essentially constant. In this process the particle will jump to another phase ellipse. There will be a sudden change in its value of W.

3. Transport Equations

Let $n(W, u)\,\mathrm{d}W$ represent the number of particles with betatron area between W and $W + \mathrm{d}W$ at the normalized acceleration momentum u.

Consider the interval between u and $u + \mathrm{d}u$. The number of particles flowing into $\mathrm{d}W$ across W is

$$n(W,u) \qquad \dot{W}(W,u)\,\mathrm{d}u$$

where

$$\dot{W} = \mathrm{d}W/\mathrm{d}u\ .$$

The number of particles flowing into $\mathrm{d}W$ across $W + \mathrm{d}W$ is

$$-n(W + \mathrm{d}W,u) \qquad \dot{W}(W + \mathrm{d}W,u)\,\mathrm{d}u\ .$$

The number of particles scattered out of $\mathrm{d}W$ is

$$\mathrm{d}W\mathrm{d}u\, n(W,u) \int \Sigma\,(W \to \overline{W})\,\mathrm{d}\overline{W}$$

where $n(W, u)\,\mathrm{d}W\,\Sigma\,(W \to \overline{W})\,\mathrm{d}\overline{W}\mathrm{d}u$ represent the number of particles with initial betatron area between W and $W + \mathrm{d}W$ that engage in a collision which scatters them between $\overline{W}$ and $\overline{W} + \mathrm{d}\overline{W}$ during u to $u + \mathrm{d}u$. The number of particles scattered into $\mathrm{d}W$ is

$$\mathrm{d}W\mathrm{d}u \int n(\overline{W},u) \sum (\overline{W} \to W)\,\mathrm{d}\overline{W}\ .$$

The net gain to the number of particles in $\mathrm{d}W$ is

$$\mathrm{d}W\,\mathrm{d}u\,\frac{\partial n}{\partial u}\ .$$

The above relations are combined to give

$$\frac{\partial n}{\partial u} = \int n(\overline{W},u) \sum (\overline{W} \to W)\,\mathrm{d}\overline{W}$$

$$-n(W,u) \int \Sigma\,(W \to \overline{W})\,\mathrm{d}\overline{W} - \frac{\partial[n\dot{W}]}{\partial W}$$

From $W = W_0/u$, we get

$$\dot{W} = -W/u\ .$$

Hence, the equation which describes the particle distribution in a strong focusing accelerator under the influence of betatron, scattering, and adiabatic forces is

$$\frac{\partial n}{\partial u} = \int n(\overline{W},u) \sum (\overline{W} \to W)\,\mathrm{d}\overline{W}$$

$$-n(W,u) \int \Sigma\,(W \to \overline{W})\,\mathrm{d}\overline{W} + \frac{1}{u}\frac{\partial[nW]}{\partial W}\ . \qquad (2)$$

4. Transport Equation solution

A practical means of solving the transport equation consists of dividing the betatron area range into q distinct groups.

Let

$$N_m(u) = \int_{W_{m-1}}^{W_m} n(W,u)\,\mathrm{d}u$$

represent the number of particles in group m.

Multiply (2) by $\mathrm{d}W$ and integrate from W_{m-1} to W_m. The result is

$$\frac{\mathrm{d}N_m}{\mathrm{d}u} = \sum_{p=1}^{q} a_{mp}N_p - N_m \sum_{p=1}^{q} a_{pm} +$$

$$+\frac{1}{u}\left[n(W_m,u)\,W_m - n(W_{m-1},u)\,W_{m-1}\right]$$

where

$$\mathrm{d}u \int_{W_{p-1}}^{W_p} \mathrm{d}\overline{W}\, n(\overline{W},u) \int_{W_{m-1}}^{W_m} \sum (\overline{W} \to W)\,\mathrm{d}W = a_{mp}\,N_p\,\mathrm{d}u$$

represents the number of particles in group p which engage in a collision and are scattered into group m between u and $u + \mathrm{d}u$.

The coefficient a_{mp} is given by the relation

$$a_{mp} = \eta_s\,\sigma_{mp}\,\frac{\mathrm{d}s}{\mathrm{d}u}$$

where

η_s is the scatterer density,

σ_{mp} is the microscopic cross-section for an average particle in group p to engage in a collision which scatters it into group m,

$\mathrm{d}s/\mathrm{d}u$ depends on the nature of the acceleration cycle.

The group m particle density is

$$n_m = \frac{N_m}{W_m - W_{m-1}}\ .$$

The number of particles which flow across a boundary between groups depends on the density of the particles which are about to

cross. An approximation which yields accurate results is

$$n(W_m,u) \cong n_{m+1} = \frac{N_{m+1}}{W_{m+1} - W_m} .$$

We can simplify the notation

$$\frac{dN_m}{du} = \sum_{p=1}^{q} b_{mp} N_p$$

where

$$b_{m1} = a_{m1} , \qquad b_{m2} = a_{m2} , \ \ldots$$

$$b_{mm} = -a_{Tm} - \frac{1}{u} \frac{W_{m-1}}{W_m - W_{m-1}}$$

$$b_{mm+1} = a_{mm+1} + \frac{1}{u} \frac{W_m}{W_{m+1} - W_m}$$

$$\ldots b_{mg-1} = a_{mg-1} , \qquad b_{mg} = a_{mg}$$

$$a_{Tm} = \sum_{p}^{q} a_{pm} - a_{mm} .$$

We choose the range of the last group to be from W_L to ∞. W_L is the betatron area of the limiting ellipse. Particles scattered into the last group are lost and cannot return to the previous groups. This means that $b_{mq} = 0$ for $m = 1, 2, \ldots q$.

The problem is resolved to the solution of a system of $q - 1$ first order linear differential equations with variable coefficients.

$$\frac{dN_m(u)}{du} = \sum_{p=1}^{q-1} b_{mp}(u)\, N_p(u) \quad m = 1, 2, \ldots, q-1 . \tag{3}$$

5. Solution of System of Equations

Several methods exist for solving a system of first order linear differential equations with variable coefficients. One of the simplest techniques is to decompose, the u range into j subranges.

If the variation in $N_p(u)$ is small over a subrange then multiply (3) by du and integrate from u_{k-1} to u_k. The result is

$$N_{m,k} - N_{m,k-1} = \sum_{p}^{q-1} b_{mp,k}\, N_{p,k-1}$$

where

$$b_{mp,k} = \int_{u_{k-1}}^{u_k} b_{mp}(u)\, du$$

$$N_{m,k} = N_m(u_k) .$$

The system of equations can be expressed in matrix form

$$\mathbf{N}_k = \mathbf{M}_k \mathbf{N}_{k-1}$$

where

$$\mathbf{N}_k = \begin{vmatrix} N_{1,k} \\ N_{2,k} \\ N_{3,k} \\ \cdot \\ \cdot \\ N_{g-1,k} \end{vmatrix}$$

$$\mathbf{M}_k = \begin{vmatrix} b_{11,k}+1 & b_{12,k} & b_{13,k} & \cdot & \cdot & \cdot & b_{1g-1,k} \\ b_{21,k} & b_{22,k}+1 & b_{23,k} & & & & \\ b_{31,k} & b_{32,k} & b_{33,k}+1 & & & & \\ \cdot & & & \cdot & & & \\ \cdot & & & & \cdot & & \\ b_{g-11,k} & & & & & b_{g-1g-1k,}+1 & \end{vmatrix} .$$

The distribution of particles after jth group will be

$$\mathbf{N}_j = \mathbf{M}_j \mathbf{M}_{j-1} \cdots \mathbf{M}_1 \mathbf{N}_0 . \tag{4}$$

In general it is not necessary for j to be large since most of the scattering occurs at low energies. The fraction of particles lost after the j th group is

$$\sum_{p=1}^{q-1} N_{p,j} \Big/ \sum_{p}^{q-1} N_{p,0} .$$

The M_k matrix can be expressed as the sum of two matrices.

$$\mathbf{M}_k = \eta_s \mathbf{M}_{s,k} + \mathbf{M}_{D,k}$$

$\eta_s \mathbf{M}_{s,k}$ contains only elements relating to the scattering between W groups. $\mathbf{M}_{D,k}$ contains only elements relating to the damping. η_s is the scatterer density. Eq. (4) now becomes

$$\mathbf{N}_j = [\eta_s{}^j \mathbf{A}_j + \cdots + \eta_s{}^2 \mathbf{A}_2 + \eta_s \mathbf{A}_1 + \mathbf{A}_0] \mathbf{N}_0$$

where $\mathbf{A}_k$ are the matrices resulting from the multiplication. $\mathbf{A}_k$ can be interpreted as the matrix expressing the distribution resulting from k scatterings accompanied by $j - k$ dampings.

6. Synchronous Oscillations

The effect of the synchronous oscillations can be considered to shift the betatron oscillation equilibrium position.

We can generalize to include gas-scattering with synchronous oscillations by constructing a phase space consisting of y, y' and y_{sm} orthogonal coordinates. y_{sm} is the maximum synchronous displacement of a given particle. Instead of a phase ellipse we now deal with a phase suface, (e.g., elliptical cone) and scattering

from one phase surface to another. The relations given in this article can be extended in a simple manner.

7. Application

The scattering loss can be calculated by direct use of relation (4). If it is necessary to know the scattering loss at many different pressures, pressure distributions, and gas compositions, the numerical work can be considerably reduced by separating the problem into single scattering losses and multiple scattering losses. Multiple scattering losses are defined as total scattering losses minus single scattering losses. This method was used to compute the scattering losses in the M.I.T.—Harvard Electron Accelerator.

The electrons are accelerated from 20 MeV to 6 GeV in 1/120 sec. The limiting vertical distance from the equilibrium orbit is 0.7 inches. $\beta_{max} = 583$ inches and $\beta_{min} = 105$ inches. The initial electron distribution was taken to be uniform throughout the limiting phase ellipse. The microscopic cross-section σ_{mp} used in computing a_{mp} was found by integrating the Goudsmit and Saunderson differential scattering cross-section[6]) over the W and u groups.

Vertical scattering losses resulting from diatomic oxygen at a uniform pressure of 1×10^{-5} mm Hg and 5×10^{-5} mm Hg are given in table 1. These figures were obtained using three W groups and six u groups. The calculations were performed on a desk computer without difficulty.

Calculations indicate that to a first approximation the relation between single scattering loss and multiple scattering loss can be considered to depend only on the single scattering loss, and not on the vacuum chamber pressure distribution and the gas causing the scattering. Except for large losses, the ratio of multiple scattering loss to single scattering loss varies approximately as the single scattering loss, provided the ratio is less than one.

A simple method of calculating single scattering losses for an arbitrary gas with any pressure distribution can be found in the M.I.T.-Harvard Accelerator report CEA-65.

Table I

Vertical scattering losses

Diatomic oxygen–uniform pressure. Uniform initial electron distribution in limiting phase ellipse

Group	$u = p'/p_0$	1×10^{-5} mm Hg			5×10^{-5} mm Hg		
		Total Loss (%)	Single Scattering Loss (%)	Multiple Scattering Loss (%)	Total Loss (%)	Single Scattering Loss (%)	Multiple Scattering Loss (%)
1	1.500	3.0	3.0	0	15.0	15.0	0
2	2.250	4.3	4.3	0	21.8	21.8	0
3	3.375	5.8	5.75	0.05	25.85	25.00	0.85
4	5.063	6.35	6.25	0.1	28.75	26.55	2.20
5	7.594	6.85	6.6	0.15	30.85	27.45	3.40
6	11.391	6.95	6.75	0.2	32.3	27.95	4.35

[6]) B. Rossi, High Energy Particles (Prentice Hall, New York, 1952) p. 65.

Acknowledgment

The author would like to acknowledge the helpful suggestions of K. W. Robinson.

NUCLEAR INSTRUMENTS AND METHODS 4 (1959) 103–106; NORTH-HOLLAND PUBLISHING CO.

CALCULATION OF THE PENETRATION OF GAMMA RAYS THROUGH THE EDGES OF A ½-INCH DIAMETER LEAD COLLIMATOR

C. SHARP COOK

U. S. Naval Radiological Defense Laboratory San Francisco, California

Received 12 December 1958

Gamma radiation from a point radioactive source located on the axis of a cylindrically-shaped collimator is not sharply defined by the geometrical aperture of the collimator. Instead some of the radiation penetrates the edges of the collimator. Calculations of the magnitude of this penetration have been made for a ½-inch diameter cylindrical aperture in a lead collimator, from point sources 8, 9, 10½, 13, 16, 32 and 48 inches from the detector end of the collimator. The results of these calculations are reported here.

1. Introduction

During many of our studies[1]) of gamma-ray spectra, we have collimated the incident gamma radiation into a region along the axis of a right circular cylindrical NaI(Tl) crystal. Because of the variety of our studies, we have generally used a cylindrical collimating aperture, ½ inch in diameter, in a lead shield.

The geometrical aperture of such a collimator does not sharply define the radiation from an external source of gamma rays. Instead some of the gamma rays penetrate the edges of the collimator, the number being a function of path length and attenuation coefficient of the collimator material[2,3,4]).

For point sources along the axis of the collimator calculations have been made to determine the number of gamma rays that penetrate the edges of the collimating aperture without being either absorbed or scattered. These gamma rays have the same probability for contributing to the full energy peak as those that pass through the geometrical aperture. Any contribution of small angle scatter to the full energy peak has not been included in the calculation.

2. Details of Calculations

If a gamma-ray source, S, is located on the axis of the collimator, the amount of unscattered

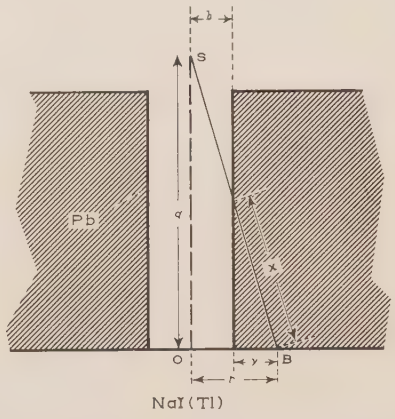

Fig. 1. Cross-Sectional View of Collimator.

radiation which arrives at some point, B, in fig. 1 on the surface of a NaI(Tl) scintillation crystal detector is reduced by a multiplicative factor exp $(-\mu x)$ below what would have arrived had there been no collimator, where μ is the attenuation coefficient for the collimating material. The quantity of radiation that passes through an incremental ring of width, dr, at a radial distance, r, from the center, 0, of the

[1]) For examples of these studies see R. L. Mather; R. A. Taylor and C. S. Cook, Nucleonics **14**, No. 8 (1956) 69; and C. S. Cook, Nuclear Physics **7** (1958) 480.

[2]) R. L. Mather, J. Appl. Phys. **28** (1957) 1200.

[3]) R. A. Hefferlin and W. E. Kreger, Nuclear Instruments **3** (1958) 149.

[4]) F. M. Tomnovec and R. L. Mather, J. Appl. Phys. **28** (1957) 1208.

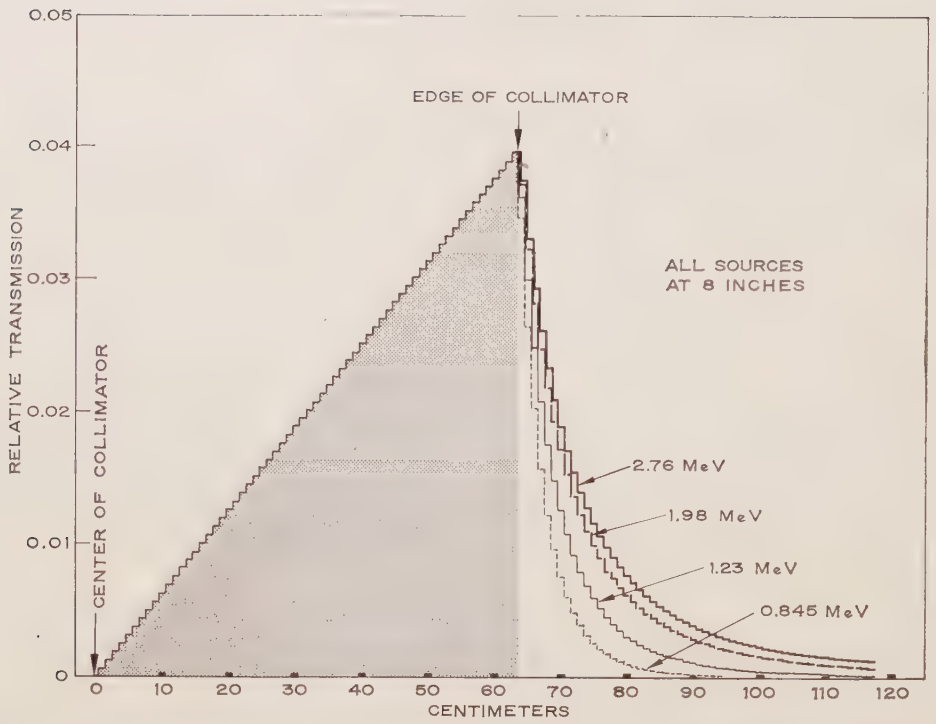

Fig. 2. Relative contribution to full energy peak of each incremental ring for four selected gamma ray energies with source at single position.

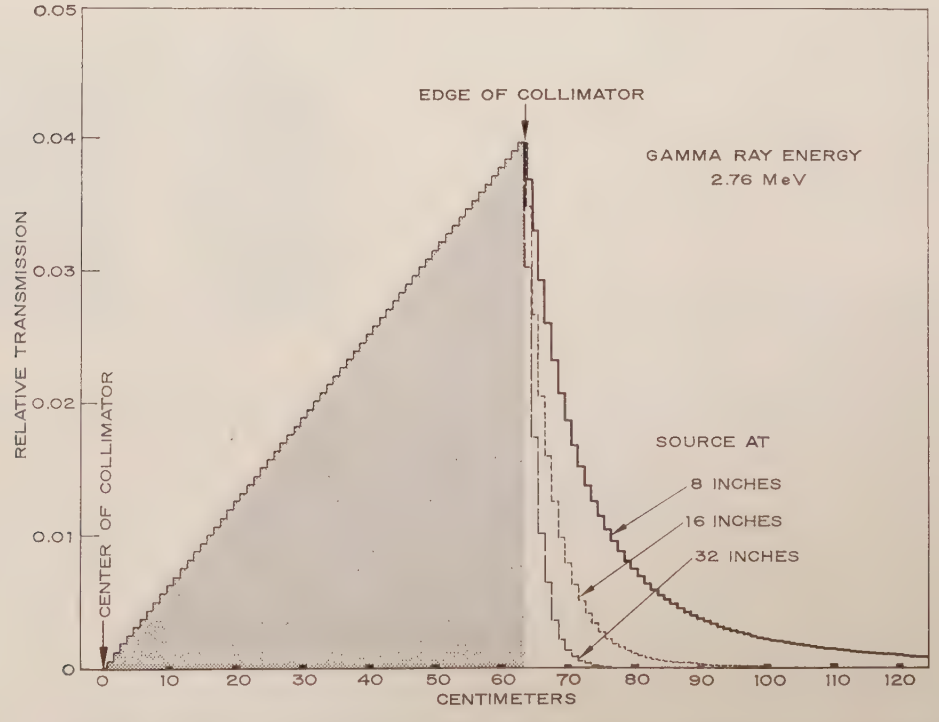

Fig. 3. Relative contribution to full energy peak of each incremental ring for single gamma ray energy with source at three selected positions.

base of the aperture depends both on the solid angle subtended by the ring and the attenuation of the gamma radiation in passing through the distance, x, of collimating material. If in fig. 1 $a \gg b$, the area of the ring is to a first approximation directly proportional to the solid angle, with the result that the intensity dI of the radiation crossing the incremental ring is

$$dI = I_0(2\pi r dr) \exp(-\mu x)$$
$$= 2\pi I_0 r \exp\left[-\mu(r-b)(a^2+r^2)^{1/2}/r\right] dr$$

where I_0 is the intensity of the gamma radiation per unit area at the bottom of the collimator. Thus the total intensity I of unscattered radiation getting into the NaI(Tl) crystal is

$$I = \pi I_0 b^2 + \int_b^\infty 2\pi I_0 r \exp\left[-\mu(r-b)(a^2+r^2)^{1/2}/r\right] dr.$$

Thus the ratio of the radiation intensity defined by the geometrical aperture to the total intensity of unscattered radiation incident on the surface of the crystal is

$$R = \frac{\pi I_0 b^2}{\pi I_0 b^2 + \int_b^\infty 2\pi I_0 r \exp\left[-\mu(r-b)(a^2+r^2)^{1/2}/r\right] dr}.$$

The integral has been solved by numerical integration on the USNRDL Datatron using summation intervals $\Delta r = 0.01$ cm. Summation has been continued until the intensity in the last ring is

$$(2\pi r \Delta r) \exp(-\mu x) < 0.0000001 .$$

To illustrate the contribution of each $\Delta r = 0.01$ cm interval the single case $\mu = 0.64$ cm^{-1}, $a = 16$ inches has been chosen. Beginning at the edge of the collimator, the contribution of each interval is given in table 1.

A tabulation of the results of the numerical integration and the resulting ratio for a number of different attenuation coefficients and a number of different source heights above the bottom of the collimator is given in table 2.

To illustrate the contribution of each incremental ring to the radiation intensity at the surface of the NaI(Tl) crystal, selected examples are shown in figs. 2 and 3. It can be noted that the degree of collimation is improved either by lowering the energy of the incident radiation or by increasing the length of collimation.

The author was assisted by Paul Wong in the coding of the problem for the NRDL Datatron.

TABLE 1

Tabulation of the contribution of individual $\Delta r = 0.01$ cm intervals for the $\mu = 0.64$ cm^{-1}, $a = 16$ inches case

Interval	$(2\pi r\Delta r)$ exp $(-\mu x)$	Interval	$(2\pi r\Delta r)$ exp $(-\mu x)$	Interval	$(2\pi r\Delta r)$ exp $(-\mu x)$	Interval	$(2\pi r\Delta r)$ exp $(-\mu x)$
64	0.0328170	84	0.0000923	104	0.0000026	124	0.0000002
65	0.0224073	85	0.0000741	105	0.0000023	125	0.0000002
66	0.0154809	86	0.0000598	106	0.0000020	126	0.0000002
67	0.0108167	87	0.0000485	107	0.0000017	127	0.0000002
68	0.0076396	88	0.0000395	108	0.0000015	128	0.0000002
69	0.0054514	89	0.0000324	109	0.0000013	129	0.0000001
70	0.0039285	90	0.0000266	110	0.0000012	130	0.0000001
71	0.0028578	91	0.0000220	111	0.0000010	131	0.0000001
72	0.0020978	92	0.0000183	112	0.0000009	132	0.0000001
73	0.0015533	93	0.0000152	113	0.0000008	133	0.0000001
74	0.0011597	94	0.0000127	114	0.0000007	134	0.0000001
75	0.0008728	95	0.0000107	115	0.0000006	135	0.0000001
76	0.0006619	96	0.0000090	116	0.0000006	136	0.0000001
77	0.0005057	97	0.0000076	117	0.0000005	137	0.0000001
78	0.0003891	98	0.0000065	118	0.0000004	138	0.0000001
79	0.0003014	99	0.0000055	119	0.0000004	139	0.0000001
80	0.0002350	100	0.0000047	120	0.0000004	140	0.0000001
81	0.0001844	101	0.0000040	121	0.0000003	141	0.0000001
82	0.0001456	102	0.0000035	122	0.0000003	142	0.0000001
83	0.0001156	103	0.0000030	123	0.0000003	143	0.0000000

TABLE 2

Tabulation of the ratio, R, of those quanta defined by a $\frac{1}{2}$-inch diameter geometrical aperture to all quanta contributing to the full energy peak

$\mu(\text{cm}^{-1})$	a (inches)						
	8	9	$10\frac{1}{2}$	13	16	32	48
0.45	0.701	0.756	0.807	0.852	0.883	0.944	0.964
0.46	0.713	0.765	0.812	0.856	0.886	0.946	0.965
0.47	0.725	0.773	0.818	0.859	0.888	0.947	0.966
0.48	0.735	0.780	0.823	0.863	0.891	0.948	0.966
0.49	0.744	0.787	0.827	0.866	0.893	0.949	0.967
0.50	0.759	0.793	0.832	0.869	0.896	0.950	0.968
0.51	0.761	0.799	0.836	0.872	0.898	0.951	0.968
0.52	0.768	0.805	0.840	0.875	0.900	0.952	0.969
0.53	0.775	0.810	0.843	0.877	0.902	0.953	0.970
0.55	0.787	0.819	0.850	0.882	0.906	0.955	0.971
0.58	0.803	0.831	0.859	0.889	0.911	0.957	0.973
0.60	0.812	0.838	0.864	0.893	0.914	0.959	0.974
0.64	0.827	0.849	0.874	0.900	0.920	0.962	0.975
0.68	0.839	0.860	0.882	0.906	0.925	0.964	0.977
0.72	0.850	0.869	0.889	0.912	0.929	0.966	0.979
0.76	0.859	0.876	0.985	0.917	0.933	0.968	0.980
0.80	0.867	0.883	0.901	0.921	0.937	0.970	0.981
0.85	0.875	0.891	0.907	0.926	0.941	0.972	0.982
0.90	0.883	0.897	0.913	0.931	0.944	0.974	0.984
0.925	0.887	0.900	0.915	0.933	0.946	0.974	0.984
1.00	0.896	0.908	0.922	0.938	0.950	0.977	0.986
1.10	0.906	0.917	0.930	0.944	0.955	0.979	0.987
1.20	0.914	0.924	0.936	0.949	0.959	0.981	0.989
1.30	0.921	0.931	0.941	0.953	0.962	0.983	0.990
1.40	0.927	0.936	0.946	0.957	0.965	0.984	0.991
1.50	0.932	0.940	0.949	0.960	0.968	0.986	0.992
1.60	0.937	0.944	0.953	0.962	0.970	0.987	0.993
1.70	0.941	0.948	0.956	0.965	0.972	0.988	0.993
1.80	0.944	0.951	0.958	0.967	0.974	0.989	0.994
1.90	0.947	0.954	0.961	0.969	0.975	0.990	0.995
2.00	0.950	0.956	0.963	0.970	0.977	0.990	0.995

NUCLEAR INSTRUMENTS AND METHODS 4 (1959) 107–111; NORTH-HOLLAND PUBLISHING CO.

INSTRUMENT FOR ELECTRON-GAMMA DIRECTIONAL CORRELATION EXPERIMENTS WITH MAGNETIC MOMENTUM SELECTION

T. R. GERHOLM and B.-G. PETTERSSON

Institute of Physics, University of Uppsala

Received 15 January 1959

A medium thick lens spectrometer was adapted for electron-gamma angular correlation experiments. The requirements to be filled are discussed. It has been found that the necessary mutual independence between spectrometer and gamma-counter can be obtained by suitable iron and mu-metal shielding. A transmission of 1.5% at 3% resolution has been obtained, when utilizing a mean emission angle of 11°.5.

1. Introduction

The directional correlation between cascading nuclear gamma rays are often studied in order to determine the multipolarities of the nuclear transitions. However, in order to determine the spins and parities of the corresponding energy levels and to establish the character of the transitions involved, additional information must be available. This can be found from the K/L ratios or from the conversion coefficients. As is well known, directional-polarisation experiments, in principle, gives the character of the transitions, but this method is of a fairly limited value since such measurements are very tedious to perform due to the inherent low efficiency of the triple coincidence arrangement used in this case.

There exists, however, an alternative way to obtain the information necessary to establish the spins and parities of the nuclear energy levels, which has not been much used hitherto, namely conversion-electron gamma directional correlation measurements. It may be shown, that the angular distribution of gamma rays relative to a given direction of emission of the cascading conversion electrons depends not only on the multipolarities but also on the characters of the corresponding transitions.

The directional correlation between beta rays and cascading nuclear gamma rays also shows interesting features. The correlation function depends on the beta interaction Hamiltonian and on the particular matrix element responsible for the beta transition. Therefore beta gamma directional correlations may sometimes yield information of the interactions involved in beta decay.

While gamma-gamma directional correlations are made in a straightforward way by means of two NaI(Tl) scintillation spectrometers operated in coincidence, the electron gamma directional correlation experiments involves certain experimental difficulties.

First of all it is necessary to secure sufficiently precise energy selection of the conversion electrons together with a resonable detection efficiency. Secondly, great care must be undertaken in order to avoid a wipe out of the angular correlation pattern due to scattering of the electrons in the source and in the backing support.

Most experiments on electron-gamma angular correlations have been made with scintillation spectrometers. An organic scintillator is used in the electron channel and the differential discriminator is adjusted on the conversion peak. However, the poor energy resolution provided by the scintillation spectrometer in particular in the electron channel, limits the potentialities of the method to very special cases only, where the decay schemes are particularly simple and the cascading transitions are well separated in energy.

Furthermore, since the angular distribution

of the L-electrons is generally quite different from that of the K-electrons, it is necessary to avoid admixtures of L-electrons in the K-electron correlation measurements. For this reason the differential discriminator channel is generally adjusted on the very edge of the unresolved (K + L) conversion peak, where the admixture of L-electrons is negligably small. This means, however, that the detection efficiency in the electron channel is considerably reduced. The accumulation of data, therefore becomes tedious.

The use of a magnetic beta ray spectrometer for momentum selection of the electrons offers several advantages. Good energy-selection is provided in the electron channel, and it therefore becomes possible to study complicated decay-schemes with closely spaced lines. The K and L-shell electrons are well resolved and the beta-ray spectrometer can therefore be adjusted on the peak of the K-conversion electrons which means that the maximum transmission of the beta ray spectrometer is utilized. Furthermore, because of the narrow momentum band pass of the spectrometer, only a small fraction of the coincidences are due to electrons belonging to a continuous beta-ray spectrum below the conversion lines or to inelastically scattered conversion electrons originating from higher energy transitions. By suitable means a positron background below the conversion line of interest can be completely removed.

On the other hand, the magnetic field used in the beta-ray spectrometer introduces certain complications. It is, of course, necessary to shield the photomultiplier in the gammachannel against the field.

However, this magnetic shield, when rotated around the source, must not affect the field distribution in the spectrometer. Otherwise the effective transmission of the spectrometer will vary with the angle. In this way systematical errors may be introduced.

2. Choice of Magnet. Preliminary Experiments

The first apparatus for electron gamma angular correlation experiments, where magnetic momentum selection was applied in the electron channel was published by Goldberg and Frankel[1]).

This instrument seems to be the only one of this kind hitherto described in the literature. Frankel and his co-workers used a short lens beta-ray spectrometer. Since in this instrument the source is situated in a "fieldfree space" the mutual magnetic independency is easily obtained. However, the efficiency of the short lens instrument is fairly low. At a resolution (relative width of half-maximum) of 2 or 3 percent the transmission (effective solid angle) is only a few tenths of (4π) the unit sphere. The coincidence counting rate therefore becomes fairly low. The long lens spectrometer gives more than 10 times higher transmission at corresponding resolving power, but in this case the source is situated inside of the magnetic field and it therefore becomes difficult to arrange an efficient magnetic shielding of the gamma channel.

If the magnet coils are encapsuled in iron, however, the source can be placed outside the field[2,3]).

A medium thick magnetic lens seems to be a suitable compromise in this case. As a matter of fact such a magnet was already available at this institute. Already in 1944 Siegbahn constructed a medium thick lens spectrometer[4]). He investigated its focusing properties and showed that this lens gives considerably higher transmission than the conventional short lens. Siegbahns' lens is encapsuled in iron and the magnetic field in the vicinity of the source is only a few percent of the maximum field strength in the spectrometer.

It should therefore not become too difficult to realize the desired magnetic independency.

Some preliminary experiments were carried out. It was shown that by means of a suitable iron and mu-metal shielding the photomultiplier in the gamma channel was unaffected by the magnetic field in the 180° as well as in the 90°

[1]) N. Goldberg and S. Frankel, Phys. Rev. **100** (1955) 1350.

[2]) T. R. Gerholm, Rev. Sci. Instr. **26** (1955) 1069.

[3]) H. Slätis and C. J. Herrlander, Rev. Sci. Instr. **26** (1955) 613.

[4]) K. Siegbahn, Arkiv mat. astr. fysik, Band **30**B, No. 1.

positions even at a field strength sufficient to focuse 5000 $B\rho$ electrons.

In order to get a reasonable resolving power, one is in this case forced to use a fairly small aperture angle because of the shape of the field. This limitation is not too serious in this particular case since for angular correlation experiments large aperture angles must be avoided anyhow, in order to keep the correction for finite solid angle reasonably small. Such a geometrical correction should always be applied in angular correlation experiments. If a beta-ray spectrometer is used, however, the situation is somewhat complicated for two reasons[5]). The corrections increases rapidly with increasing aperture angles. In the spectrometer only the outer part of the aperture cone is accepted. For obvious reasons, the central part, where the correction is small, is screened off. This means that the geometrical correction is larger for a beta-ray spectrometer than for a scintillation crystal with a corresponding solid angle. Furthermore the aperture angle of the spectrometer depends on the transmission-setting and the dimensions of the source. The curvature of the electron trajectories should also be taken into account. Altogether this implies that for the spectrometer the aperture angle is not easily determined with great accuracy. It is therefore advisable to chose a fairly small aperture angle thus reducing the influence of the geometrical correction. The uncertainty in this correction then gives only a minor contribution to the limits of error in the final result.

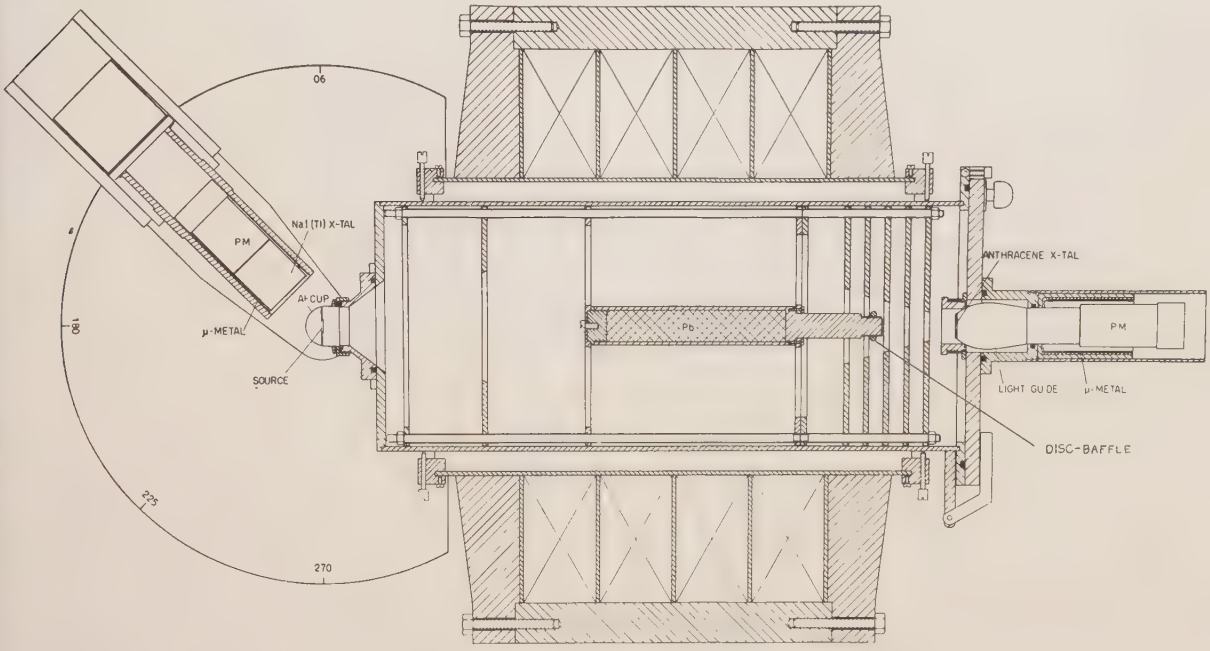

Fig. 1. Electron-gamma angular correlation spectrometer.

3. Electron Optics

On the basis of the preliminary focusing experiments discussed above, the mean emission angle was taken to be 12°.5. The electron-trajectories were then determined by means of the usual photographic ray-tracing technique.

The disc-baffle (fig. 1) determines the trajectories of the extreme rays, i.e. the maximum and minimum emission angles. Within certain limits the effective transmission as well as the mean angle of emission can be varied at will by adjusting the radial and axial settings of this discbaffle. A number of different discs which correspond

[5]) S. Frankel, Phys. Rev. 83 (1951) 673.

[6]) Porter, Freedman, Novey and Wagner, Phys. Rev. 103 (1956) 921.

to different diameters were made and for each disc the axial position was adjusted to correspond to the chosen mean angle of emission.

To determine the size of the detector a photographic plate was placed perpendicular to the axes. From the exposures the diameter of the focus was found to be 24 mm. A ⌀ 25 mm anthracene crystal with a thickness of 2 mm is used as detector. The crystal was cemented with Araldite onto a short light guide provided with a matched profile light-collecting head (logaritmic spiral + parabola). An EMI 6342 photomultiplier tube supplied with a mu-metal and iron shield is used.

The thickness of the crystal, 2 mm, is chosen to stop completely electrons with energies of about 600 keV. The scintillation peak as observed with a differential discriminator was found to have a relative halfwidth of 18% for 500 keV electrons. For electron energies above 600 keV double peaks appeared[6]). These doublepeaks are supposed to be due to the fact that some of the electrons are completely absorbed while some penetrate through the crystal giving off only a fraction of their energy to the scintillator.

Since positron and negatron trajectories rotate in opposite directions through the lens, a twisted baffle system can be used to suppress the positron background. This reduces the admixtures of positron gamma coincidences to negligible amounts.

In order to construct this baffle the rotation of the trajectories were determined.

An interesting fact is that the rotation of the electron trajectories in this case ($\alpha_{max} = 12.°5$) comes very close to the theoretical value derived for the paraxial ray approximation[7]).

Finally the rotational symmetry was investigated. For this purpose a disc baffle with a sector slit was placed in front of the source perpendicular to the axes of symmetry. The source was carefully centered on the symmetry axes by light optical means. The sector slit was rotated round the axes and the peak transmission was studied for various azimutal emission angles.

[7]) K. Siegbahn, Beta- and Gamma-Ray Spectroscopy (North Holland Publ. Company, Amsterdam, 1955) p. 78.

By means of a number of micrometerscrews (fig. 1), the vacuum chamber with sourceholder, baffles and detector could be adjusted relative to the lens. After a rather tedious trial and error procedure, rotational symmetry within 5% was obtained.

4. Transmission and Resolution

An absolute determination of the transmission at a resolution of 2.5% was done in three ways. By measuring the counting rate on the peak of the 662-keV K-conversion line of a Cs^{137} source with known strength.

By a coincidence measurement on Bi^{207} taking the 1064-keV K-conversion line in the spectrometer and the 569 keV line in the γ-detector.

By a geometrical calculation. All three methods gave within the limits of error the same result.

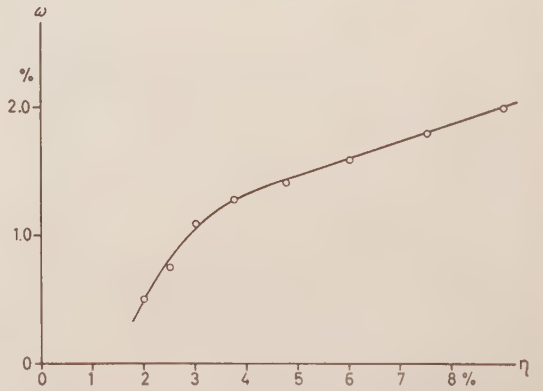

Fig. 2. Effective transmission (percent of 4π) versus resolution (relative width at half maximum of spectrometer resolution curve).

In fig. 2 is shown the transmission as a function of the resolution.

5. The Source Holder

In order to obtain a good rotational symmetry, the source must be carefully centered on the axis. For this purpose the source holder is mounted on a slide which can be moved in the vertical direction by means of a micrometerscrew. The source and the backing support are mounted on a thin Al-ring placed in a luciteframe.

It is also necessary to avoid gamma ray scattering. This is particularly serious in the 90° position, where small angle Compton scattering of gamma rays may give rise to events accepted by the differential discriminator since the scattered gamma rays will have nearly the same energy as the initial radiation.

To avoid this the source is located in a semi-spherical Al-cup made sufficiently large. Presence of dense materials is avoided in the vicinity of the source. An essential feature of the spectrometer of importance in this connection is that the iron and copper of the magnetic lens is sufficiently far away from the source. Therefore the scattering effects in these dense materials are reduced partly because of the geometrical distances and partly because Compton-scattering in these remote parts of the instrument backwards into the scintillation crystal corresponds to large angular deflections and hence to large energy differences between inital and scattered gamma rays. The scattered gamma rays will then, in general, not be accepted by the discriminator.

6. Performance and Applications

To check the correct working of the apparatus, a correlation measurement was made on the well-known 1064–569 keV cascade in Bi^{207}.

McGowan[8]) reports for the 1064 keV e^-—569 keV γ correlation a value of $A_2 = 0.241 \pm 0.004$ in agreement with the theoretical value $A_2 = 0.232 \pm 0.004$. We found an $A_2 = 0.240 \pm 0.007$.

For a detailed report on some other applications of this instrument see refs. [9]) and [10]).

[8]) F. K. Mc Gowan, Phys. Rev. **92** (1953) 524.

[9]) T. Lindqvist, B. G. Pettersson and K. Siegbahn, Nuclear Physics **5** (1958) 47.

[10]) T. R. Gerholm and B. G. Pettersson, Phys. Rev. **110** (1958) 1119.

NUCLEAR INSTRUMENTS AND METHODS 4 (1959) 112–114; NORTH-HOLLAND PUBLISHING CO.

IMPULS - ZEITFORMER FÜR SCHNELLE KOINZIDENZSTUFEN

WOLFGANG GRUHLE

Max Planck-Institut für Kernphysik, Heidelberg

Recieved 11 January 1959

Triggered pulse generators feeding coincidence stages introduce a time dispersion due to the amplitude dependence of the trigger time. The new method combines the steep zero crossover of the double differentiated pulse spectrum with the backlash characteristic of a SCHMITT trigger. By this way it is possible to set the flop-back level of the trigger circuit on the zero crossing of the signals which is independent of amplitude. The highest possible coincidence resolution with slower scintillators may thus be reached.

Die elektrischen Impulse am Ausgang eines Szintillationszählers haben eine amplitudenabhängige Anstiegssteilheit; dadurch tritt in einer Koinzidenzanordnung bei Impulsen verschiedener Amplitude eine störende Zeitdispersion auf. Sie bedingt die untere Grenze für die Koinzidenz-Auflösezeit in der Grössenordnung der Abklingzeit des Szintillators.

Im allgemeinen lässt man von langsamen Szintillatoren, etwa NaI(Tl), vor der Koinzidenzstufe erst Standardimpuls-Generatoren antriggern. Triggerstufen erleiden zwei Arten von Verzögerungen: die Zeitdispersion durch die Signalamplituden und eine interne Verzögerung, die im Bereich der Ansprechschwelle am grössten ist und ihre Ursache im nicht idealen Kennlinienknick hat.

In mehreren Arbeiten[1–5]) ist bereits versucht worden, die Zeitdispersion auszuschalten. Die Verwendung von Dioden und Gleichstromkreisen[1–3]) ergibt ungenügende Temperatur- und Langzeitkonstanz. Doppelte Impuls-Differentiation und Ausnützung des amplitudenunabhängigen Nulldurchganges[4]) als Triggerzeitpunkt verlangt Transponierung des Nullniveaus auf die Triggerschwelle durch störanfälligen Schaltungsaufwand[5–6]).

Die im Folgenden angegebene Schaltung[7]) vermeidet die genannten Nachteile. Das doppelt differenzierte Impulsspektrum triggert einen

[1]) B. Smaller, Nucleonics **10**/3 (1952) 41.
[2]) P. Weinzierl, Rev. Sci. Instr. **27** (1956) 226.
[3]) B. Johansson, Nuclear Instruments **1** (1957) 274.
[4]) K. Malmfors *et al.*, Nuclear Instruments **1** (1957) 186.
[5]) M. Spighel and L. Penège, Journ. Phys. Rad. **18**/3 (1957) 19A.
[6]) E. Gatti, mündl. Mitteilung.
[7]) Vortrag, gehalten 17.9.59 im Colloque International sur l'Electronique Nucléaire (Paris). Nach priv. Mitteilung von E. Fairstein im Dezember 1958 wurde von Love, Peele und Fairstein (ORNL) eine ganz ähnliche Lösung gefunden.

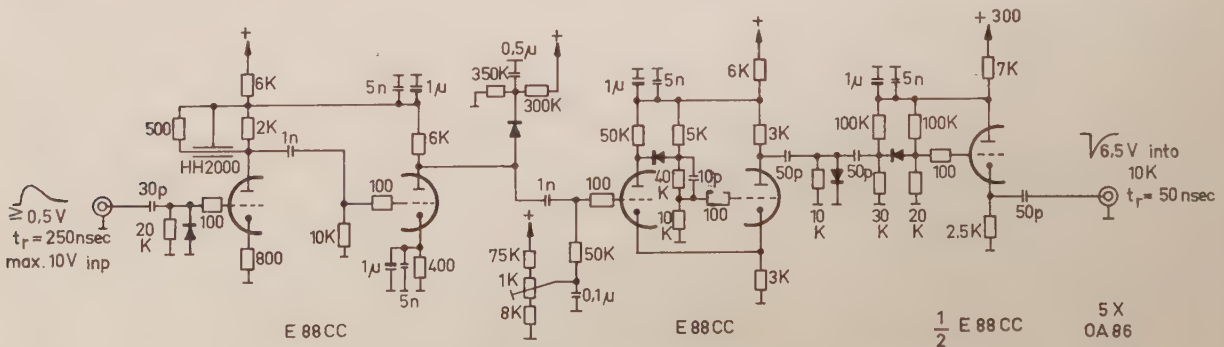

Abb. 1. Impuls-Zeitformer mit amplitudenunabhängigem Triggerzeitpunkt.

sehr konstanten SCHMITT-Kreis an. Da infolge seiner Hysterese der Schwellenwert des Ankippens über dem des Zurückkippens liegt, kann der zweite genau auf Nullniveau gelegt

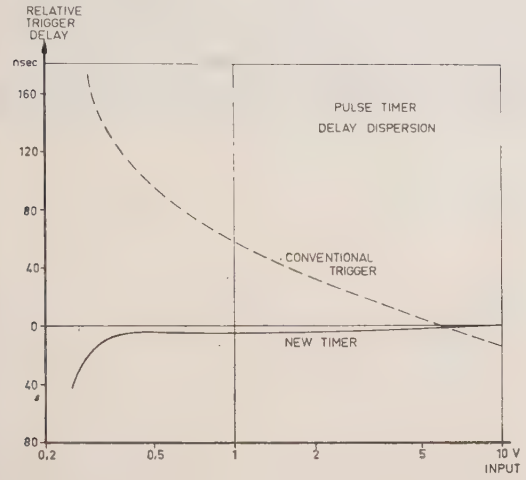

Abb. 2. Triggerverzögerung als Funktion der Signalamplitude, mit (ausgezogen) und ohne (gestrichelt) Zeitformer.

hängt nur noch von der Anstiegszeit der werden. Während das Ankippen mit der oben beschriebenen Zeitdispersion behaftet ist, geschieht das Zurückkippen durch geeignete Wahl der Arbeitsbedingungen beim amplituden- unabhängigen Nulldurchgang. Dieser Signale ab und dient zum Antriggern des nachfolgenden Koinzidenz-Impulsgenerators.

Abb. 1 zeigt eine praktisch ausgeführte Form. Das erste Differenzierglied liegt am Eingang, das zweite im Anodenkreis der ersten Röhre (Kabel). Das normalerweise auftretende dritte Überschwingen wird dadurch kompensiert, dass das Differenzierkabel nicht kurzgeschlossen, sondern mit einem kleinen Widerstand fehlabgeschlossen ist. Die ersten beiden Röhren dienen nur als Differenzier- und Umkehrstufe, sie lassen sich leicht an grössere Amplituden oder andere Anstiegszeiten anpassen oder durch einen doppelt differenzierenden Verstärker[8]) ersetzen. Der nachfolgende SCHMITT-Kreis arbeitet mit einer Hysterese von rund 2 Volt und besitzt eine "Verschärfer"-Diode. Durch die Serienschaltung dieses zweiten nichtlinearen Gliedes mit dem Rückkopplungszweig wird der untere Kennlinien-Einsatzknick der Stufe erheblich schärfer. Die negative Abfallflanke wird differenziert und gelangt auf den Ausgangskathodenfolger über einen Diodendiskriminator. Dieser ist nicht kritisch und schneidet sehr kleine (kapazitiv hindurchgehende) Restimpulse unterhalb des Triggerniveaus ab. Der Begrenzer am Eingang des SCHMITT-Kreises kappt sehr grosse Impulsamplituden, die Gitterstrom ziehen würden.

Die Unabhängigkeit des Triggerzeitpunktes von der Signalamplitude zeigt Abb. 2. Hier

[8]) E. Fairstein, Rev. Sci. Instr. **27** (1956) 475.

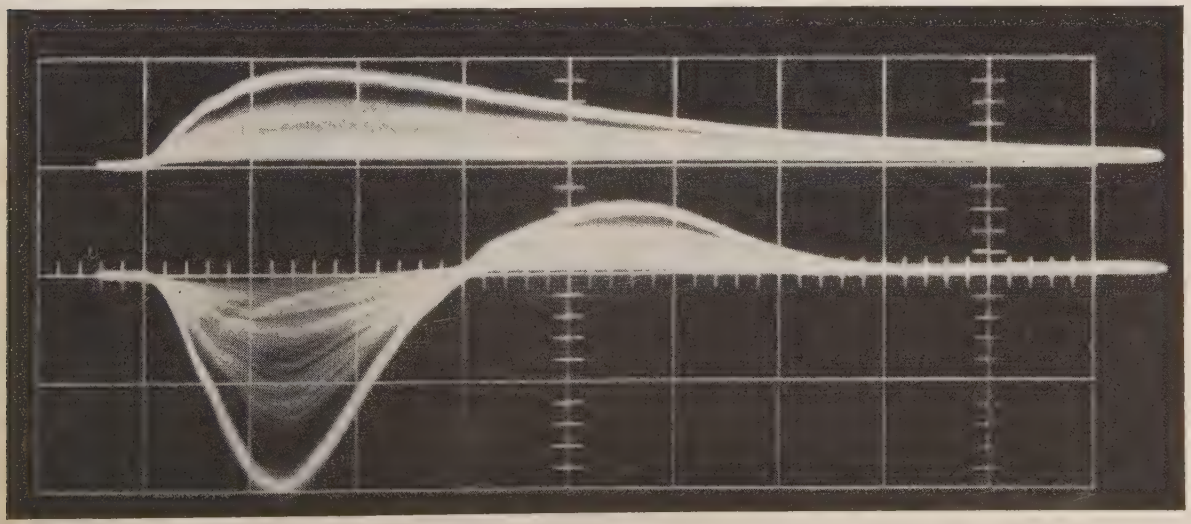

Abb. 3. Impulsspektrum (Cs^{137}) vor und nach der Differentiation.

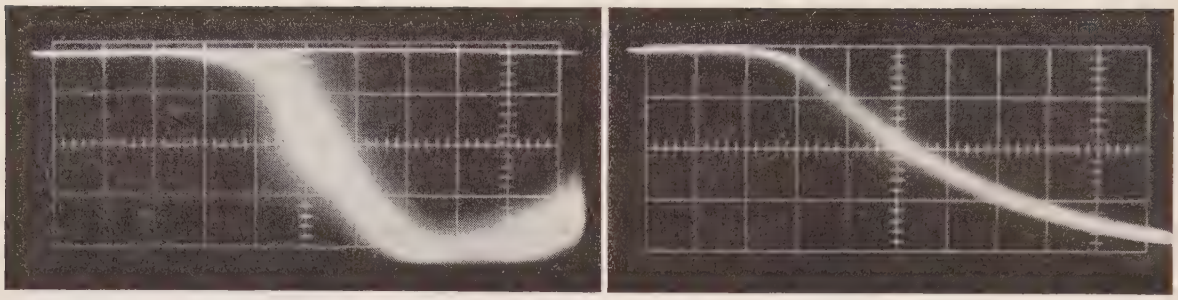

(a) (b)

Abb. 4. Ausgangsimpuls des Zeitformers mit übriggebliebener Zeitdispersion, (a) mit NaI(Tl), (b) mit Anthrazen. Massstab 20 nsec/Karo.

wurde die Triggerverzögerung gegen die Amplitude eines Testimpulses aufgetragen (ausgezogene Kurve). Nur in unmittelbarer Umgebung des Triggereinsatzes ist die oben erwähnte interne Verzögerung übrig geblieben. Sie beträgt aber nur etwa 0.2 Volt im ganzen Amplitudenbereich. Zum Vergleich ist (gestrichelt) die Verzögerung eingetragen, mit der die SCHMITT-Stufe alleine (ohne Zeitformer) antriggert.

Die Aufnahme eines Szintillations-Spektrums von Cs^{137} mit NaI(Tl) vor und nach dem Differenzieren zeigt Abb. 3. Der beim Nulldurchgang vom SCHMITT-Kreis erzeugte Ausgangsimpuls ist in Abb. 4a aufgenommen (Zeitmassstab 20 nsec/cm). Der Oszillograph wurde dabei vom Eingangssignal bei sehr niedriger Ansprechschwelle angetriggert, so dass auch die Nullinie erscheinen kann. Obwohl die verbleibende Zeitdispersion noch den Fehler der Oszillographen-Triggerung enthält, ist sie hauptsächlich auf zeitliche Schwankungen der Signale im Szintillator (Schwankungen der Impuls-Anstiegszeit) zurückzuführen. Dies zeigt ein Vergleich mit Abb. 4b, bei der Anthrazen statt NaI(Tl) verwendet und die Differenzier-Zeitkonstante entsprechend geändert wurde. Die photometrische Auswertung der Abb. 4a und 4b lieferte eine Halbwertsbreite der Verteilung von etwa 24 bzw. 11 nsec. Diese Werte dürften die untere Grenze einer Koinzidenzauflösung darstellen, die mit NaI(Tl)- bzw. Anthrazen-Kristallen noch sinnvoll erscheint.

Die Schaltung arbeitete in doppelter Ausführung vor der Koinzidensztufe eines COMPTON-Szintillations-Spektrometers monatelang im Dauerbetrieb ohne Nachjustierung. Der Koinzidenzwirkungsgrad wird nur noch durch die primären zeitlichen Schwankungen der Signale begrenzt.

NUCLEAR INSTRUMENTS AND METHODS 4 (1959) 115–116; NORTH-HOLLAND PUBLISHING CO.

A FAST SCALING STAGE

F. A. MULLER

Natuurkundig Laboratorium der Universiteit van Amsterdam

Received 31 January 1959

A description is given of a new type of scaling stage. The tested circuit, with stray capacitances kept at a minimum, operated on incoming pulses up to 100 MHz.

The speed of operation of scaling stages is limited by tube capacities and transconductance. The minimum time between two separately counted pulses is needed for two phases: first the proper switching phase and second a relaxation phase during which the system regains its sensitivity to triggering. The circuit to be shown here eliminates the second phase and is therefore capable of a higher speed of operation than other systems known to the author. It can be described as a bistable circuit that can be turned into an oscillator for short times. When this is done during one half cycle of the oscillator a transition from one stable state to the other is effected. The circuit is shown in figure 1. The coupling from anodes to grids of T_1 is essentially direct. As long as no negative pulses enter, both halves of T_2 carry a current of 20 mA and the crystal diodes are conducting. Therefore the cathodes of T_1 are connected through a small impedance. The system will then have two stable states, only one half of T_1 will be conducting.

When now a negative pulse shuts down the current through T_2 the potential of the whole system rises. At the same time the diodes stop conducting and the system is no longer bistable since the connection between the cathodes has become capacitive. The capacity is chosen so as to make the system just oscillate. Its frequency is then 50 MHz and the oscillation is directly in full swing since it starts in an extreme position.

At the end of the pulse the upward movement reverses in a downward one; the oscillation however continues until the crystal diodes are conducting again. When the length of the pulse is 6 nsec the total length of the oscillation will

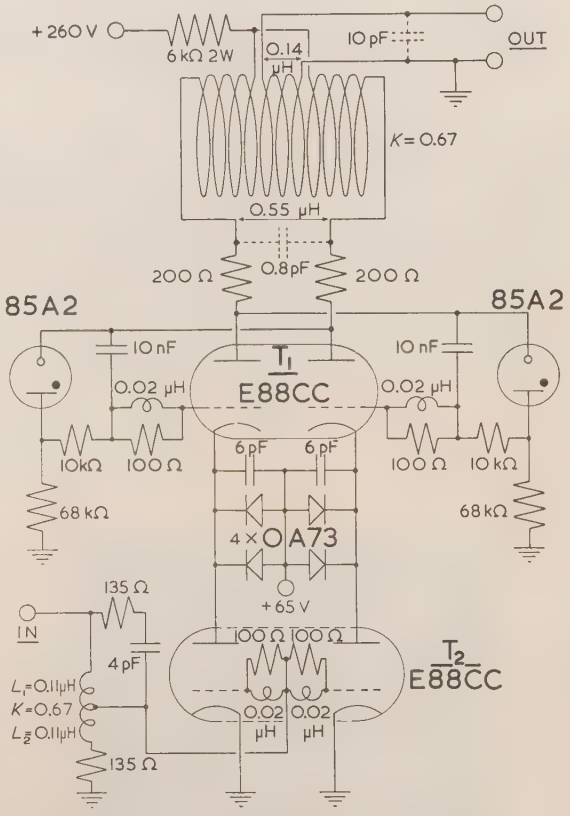

Fig. 1. Circuit diagram of fast scaling stage.

be 10 nsec, therefore one half cycle will be completed and the system will end up in the opposite state.

Figure 2 shows both cathode voltages as a

function of time for a pulse of 6 nsec duration as well as for a pulse of 12 nsec. Obviously a pulse of 12 nsec acts as two pulses: a second 6 nsec pulse coming directly after another is counted independently. The second pulse is stored up in

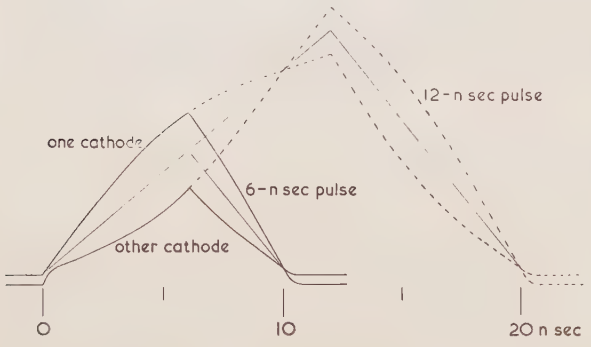

Fig. 2. Time course of cathode voltages in scaling stage as result of 6 nsec pulse (full line) and 12 nsec pulse (dotted line). The thin line indicates the average position.

the increased potential of the whole system. This storage is of course not indefinite and equally distributed pulses should not exceed a frequency of 100 MHz in order to be scaled correctly.

The transformer in the anode circuit is designed so as to provide high frequency compensation as well as an output pulse, alternately positive and negative, of about 1 V height and 8 nsec duration. The high frequency compensation adds about 30 percent to the maximum operating frequency. The capacitive components of this compensation circuit can be realized as small stray capacities and the input capacity of a tube E 180 F, coupling the stage to the next. The transformer can be made as shown in the circuit diagram, 4, 3 and 4 turns of 0.3 mm wire spaced regularly at 0.9 mm, total length 9 mm, diameter 11 mm.

The input circuit converts the input capacitance of about 20 pF into a resistance of 135 ohm whereas it contributes not much to the rise time of the incoming pulse. The rise time for a sharp incoming pulse is 2 nsec.

The tested circuit has been built with as small as possible stray capacities. Its symmetry had to be carefully adjusted, the tubes 85A2 had to be equal within 0.1 volt. This requirement will be lessened when crystal diodes with smaller forward resistance and good H.F. properties will be available. At the cost of some speed the reliability of the circuit can be improved by slightly increasing the anode resistors, while keeping the inductances of the compensating transformer proportional to the square of the anode resistances.

NUCLEAR INSTRUMENTS AND METHODS 4 (1959) 117; NORTH-HOLLAND PUBLISHING CO.

LETTER TO THE EDITOR

HIGH SPEED TRANSISTORIZED SCALE-OF-TWO

E. BALDINGER, P. SANTSCHI and P. WEHRLI

Department of Applied Physics, University of Basel, Switzerland

Received 22 December 1958

We recently described a new circuit for a scale-of-two suitable for high counting rates[1]).

Meanwhile we pushed forward our work into two directions:

(1) We improved the circuit by slightly changing the d.c.-conditions of the transistors. A circuit diagramm of this improved scale-of-two is shown in fig. 1. Using SB 100 and 2N 128 transistors, a time resolution of 50 mμs had been achieved permitting reasonable tolerances for the variation of the circuit elements. (The value of each resistor may be changed about $\pm$ 10%.) 40 mμs is the absolute upper limit with nearly no tolerances.

The proper function of this scale-of-two had been checked with a multiple-pulse-generator. This generator gives groups of 4 to 20 pulses with max. 20 V pulse hight and 30 mμs base width. Fig. 2 shows typical input—and output—signals of the scale-of-two.

[1]) E. Baldinger and P. Santschi, ZAMP 9 (1958) 88–90; Nuclear Instruments 2 (1958) 128–129.

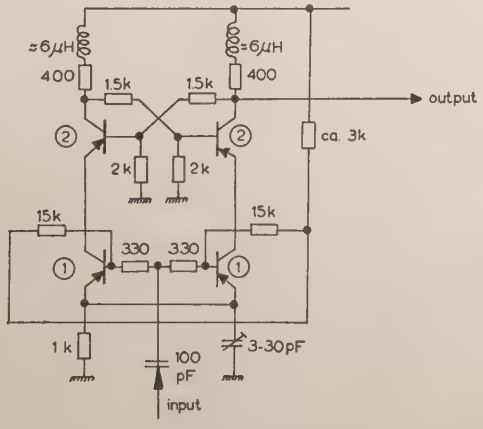

Fig. 1. 20 Mc/sec Scale-of-two. ① Philco SB 100, ② Philco 2N 128. Triggersignal: 5 V in reverse direction, may be varied from 3 V to max 8 V. Supply voltage — 10 V.

Coupling of two of these stages is possible with a conventional 2N 128 emitter-follower. We built further a scale-of-ten consisting of the above mentioned stages. This scale-of-ten is working at frequencies as high as 10 Mc/sec with good tolerances[2]).

(2) Preliminary experiments had been accomplished using 2N 501 transistors for the upper two and 2N 128 transistors for the lower ones in the same circuit as shown in fig. 1, where the supply voltage had been changed from —10 V to —20 V. A resolution of 20 mμs for double-pulses had been achieved. Withoud changing the circuit the scale is going well up to 40 Mc/sec with sine-wave-input. Tolerances of this scale-of-two are equal to that mentioned above.

This work had been supported by "Stiftung-Hasler-Werke-Bern".

[2]) E. Baldinger, P. Santschi and P. Wehrli, H.P.A. 31 (1958) 575–576.

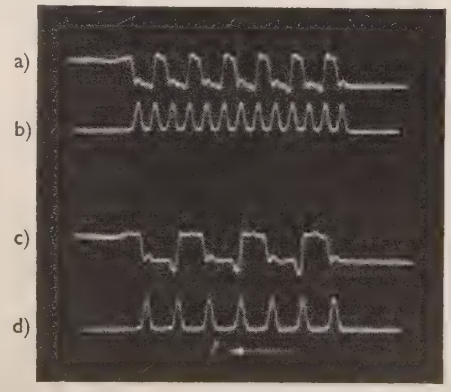

Fig. 2. (a) Output – Signal, vert. 2V/cm, hor. 0.1 μs/cm; (b) Input – Signal, vert. 5V/cm, hor. 0.1 μs/cm; (c) Output – Signal, vert. 2V/cm, hor. 0.1 μs/cm; (d) Input – Signal, vert. 5V/cm, hor. 0.1 μs/cm.

NUCLEAR INSTRUMENTS AND METHODS 4 (1959) 118–119; NORTH-HOLLAND PUBLISHING CO.

LETTER TO THE EDITOR

THE SELECTION OF STAINLESS STEELS FOR USE IN LIQUID HYDROGEN BUBBLE CHAMBERS†

PIERRE AMIOT

Proton Synchrotron Division of CERN, *Geneva*

Received 11 February 1959

It is felt that some useful purpose may be served by publishing experimental results connected with the magnetic properties and the stability of stainless austenitic steels, obtained in the course of tests for the selection of the steel to be used in the construction of liquid hydrogen bubble chambers, which should be non-magnetic at low temperatures.

1. Chemical Composition of Steels Tested

Serial No.	C %	Si %	Mn %	Cr %	Ni %	Mo %	Nb + Ti %	N_2 %	% Ni equiv.	% Cr equiv.
1	0.04	≈ 0.80	≈ 0.50	≈ 15	≈ 27	≈ 1.20	≈ 2	?	28.5	18.5
2	0.03	0.44	0.54	17.30	9.49	—	—	0.023	11.35	18.0
3	0.03	0.32	0.65	17.36	9.53	0.05	—	0.013	11.15	17.9
4	0.09	0.46	0.42	17.6	9.77	0.19	—	0.023	13.35	18.5
5	0.03	0.37	0.98	18.4	13.4	0.06	0.12	0.009	15.05	19.1

It is worth calculating the chromium and nickel equivalents of our various steels to see how they fit into the composition diagrams for austenitic steels[1,2].

equivalent in
$\%\text{Ni} = \%\text{Ni} + 30\,\%\text{C} + 30\,\%\text{N}_2 + 0.5\,\%\text{Mn}$

equivalent in
$\%\text{Cr} = \%\text{Cr} + \%\text{Mo} + 1.5\,\%\text{Si} + 0.5\,\%\text{Nb}$

† Magnetic measurements were carried out under contract for the European Organization for Nuclear Research —Geneva— by the Association pour le Développement des Recherches auprès de l'Université de Grenoble, under the supervision of Prof. L. Weil, of the Faculty of Sciences, Grenoble University (France).

Analytical tests were conducted either by the manufacturers or by the Laboratoire fédéral d'Essais des Matériaux, Zurich (Switzerland).

The results can be found in the two last columns of the previous table.

2. Heat Treatment

All the steels, including sample 3–1, have been tested in the "as received" condition, which means after heat treatment by the producer. The sample 3–2 received a further 20% cold working followed by quenching from 1 050° C.

3. Results *(See table next page)*

These were obtained on cylindrical samples 8 mm long and 1.5 mm in diameter.

The following table gives the values of the magnetization per gram σ in CGS EMU for a field of 15 000 oersted, as defined by:

$$B = H + 4\pi\rho\sigma$$

where ρ is the specific mass.

4. Examination of Results

The magnetism of No. 1 Steel is obviously reversible and this is attributable to the fact

[1] A. L. Schaeffler, The Iron Age **162** (1) (1948) 72–79.

[2] W. T. De Long, G. A. Ostrom and E. R. Szumachowski, The welding Journal **35**, Suppl. (Nov. 1956) p. 521s–528s.

that a Curie point exists below the ambient temperature.

No. 4 and No. 5 Steels are both perfectly stable at 20° K. It is difficult to say whether the slight increase in magnetization at low temperature is attributable to a Curie point or to an increase in paramagnetism.

chemical inhomogeneities consequent upon the small amount of hot work on this steel (6 to 1 reduction).

It should finally be noted that the phase change rate depends on the number of cooling cycles through which the samples are put.

In conclusion it seems that steels having up

	Before cooling $T = 293°$ K	After cooling once $T = 20°$ K	After cooling n times $T = 20°$ K	After cooling n times $T = 293°$ K
No. 1 Steel	0.93	18.0	$n = 40$ 18.5	0.94
No. 2 Steel	—†	7.5	$n = 40$ 8.1	—†
No. 3–1 Steel	1.95	18.1	$n = 6$ 20.5	19.0
No. 3–2 Steel	3.92	10.1	$n = 6$ 15.0	13.8
No. 4 Steel	1.03	2.12	$n = 6$ 2.12	1.04
No. 5 Steel	0.48	2.40	$n = 6$ 2.44	0.50

† Though no exact figures are available, a qualitative experiment shows that No. 2 Steel is practically non-magnetic at ambient temperature and slightly magnetic after cooling. Its behaviour is therefore similar to that of No. 3 Steel.

As for No. 2 and No. 3 Steels, they show a $\gamma \rightarrow \alpha$ phase change at low temperatures. The change in No. 2 Steel is of the order of 3.5%. No. 3 Steel produces a phase α of about 9% in stage 1 and a little under 7% in stage 2. According to the diagram quoted as a reference[2]), No. 2 Steel is situated in a zone where the proportion of phase α actually is 3.5%. According to the same diagram, the same rate of change can be expected of No. 3 Steel. It is believed, though not confirmed so far, that this difference is due to the considerable

to 7% α phase, which corresponds to a permeability at 15 000 oersted, of roughly 1.10, can be used for liquid hydrogen bubble chambers, if the carbon content is low enough to give a negligible brittleness. In large cast parts there may be difficulties in meeting the above requirements.

Acknowledgments

The author wishes to record his gratitude to CERN for being allowed to publish the above results.

BOOK REVIEWS

K. DIELS, R. JAECKEL, *Leybold Vakuum–Taschenbuch für Laboratorium und Betrieb*, (Springer-Verlag, 1958)

This is not a textbook on vacuum technique and certainly does not form an introduction to the subject, but is a book of reference.

The application of high vacuum technique is very extensive today and calls for many specific solutions. In the preface to the book the authors also stress the importance of calculating every detail in a vacuum system, if it should well fulfil the function aimed at. In accordance with that a large part of the book deals whith problems regarding mechanical parts in a pumping system: pumps, valves, baffles, tubing etc. A lot of valuable information on the subject is to be found in tables and diagrams, but is perhaps not of general interest for the user of vacuum apparatus. Naturally this information is limited with Leybold pumps and equipment.

The average reader will find more interest in the latter parts of the book which deal with vacuum gauges, special techniques and properties of materials.

A small but very clear chapter on different vacuum gauges describes 14 types, with details about the theory of operation, the measuring ranges, and what is really measured. There is also a comparison of their advantages and disadvantages, but this seems to be of less value as the necessary associated equipment is not taken into account.

Two large chapters are devoted to properties of materials, giving the information in the form of tables and diagrams with little text, information that physicists, chemists and others will find most valuable and up to date. This together with the vast amount of references at the end of the book gives as a lasting impression that the book well serves its purpose as a small but comprehensive reference book.

SETH BERGLUND

J. KOCH (Editor), R. H. V. M. DAWTON, M. L. SMITH, W. WALCHER: *Electromagnetic Isotope Separators and Applications of Electromagnetically Enriched Isotopes* (North-Holland Publishing Company, 1958, XI + 314 p., Gld. 26,50)

The reviewer can attest to an ever-increasing need for a general survey of methods and applications of electromagnetic isotope separation. It has been almost embarrassing to have to refer "the potential worker in the field", who has grown many-headed indeed in recent years, to a variety of more or less obscure sources. The initiative of the North-Holland Publishing Company in issuing an Edited Volume on the subject, written by recognized authorities, is received with satisfaction.

Despite its compact size, this book contains a considerable amount of information. In the first of the three parts, the editor has found ample opportunity to demonstrate his familiarity with the history of small and medium size separators. The very ambitious enumeration of applications leaves no doubt as to the usefulness of such instruments in nuclear research. Several tables make for increased clarity, and the illustrative material is strikingly good (as in the rest of the book).

R. H. V. M. Dawton and M. L. Smith share the authorship of Part B, which is devoted to large scale separation. In an attractively straightforward manner they describe the principles and development of the calutron-type machines and even give some interesting details of the gigantic Oak Ridge project for the production of U^{235} during the war. The inclusion of a chapter on the Harwell 90° sector separator illustrates the difficulty in making a clear distinction between laboratory separators and production plants.

General treatments of physical and technical problems have been omitted from the first two parts and brought together in a separate Part C, written by W. Walcher. The arrangement offers obvious advantages, and much of the contents of this third part will be extremely useful for future designers of separators.

The authors do not claim completeness in their accounts, and indeed a survey of the subject index does reveal a few remarkable omissions. But those who look in vain for terms such as "separation factor", "enrichment factor", or "degree of separation" will probably find what they need under "enhancement" or "isotopic contamination", and so on. In the reviewer's opinion, however, a coherent discussion of the basic concept of attainable isotopic purity would have increased the value of this book, which is already well worth its moderate price.

G. ANDERSSON

Spotlight on Industry

This section appears each month and features various happenings of interest in the nuclear industrial world and objective information on products of the nuclear manufacturers. It is offered entirely as a service and all nuclear manufacturers are cordially invited to submit clearly objective and descriptive material on their endeavours and product developments for consideration for use in this section.

SHIELDED SCINTILLATION HEAD UNIT NE 5503

NEW SPECIAL ROTARY LIGHT LOCKING DEVICE

Nuclear Enterprises (G.B.) Ltd., Bankhead Medway, Sighthill, Edinburgh, 11, Scotland

The new head unit features a special rotary light locking device which prevents light reaching the photomultiplier during the changing of samples. In order to do this, the sample cell is loaded in a chamber on the side of the castle and revolved in a simple two-movement operation into the counting position. This operation brings the counting cell in close contact with the photomultiplier. The coupling medium between the photomultiplier and the sample cell is silicone fluid MS 200 of low viscosity. The reason for the light locking device is that a photomultiplier which is not dark-adapted gives a background noise many times greater than it does after being kept in the dark for several days. The rotary light locking device is superior to an optical shutter system which necessitates a finite gap between photomultiplier and counting cell and resultant loss of light. A new 1″ diameter photomultiplier of very low noise level is incorporated in the head, along with a White cathode follower preamplifier of good signal to noise ratio, and a 1½″ thick lead shield.

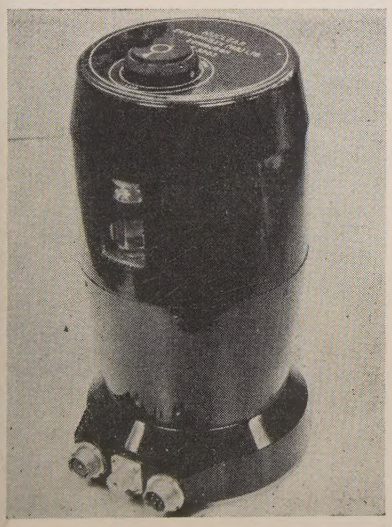

NEUTRON SPECTROMETER

E.M.I. Electronics Ltd., Engineering Development Division, Wells, Somerset, England

A fully transistorised data recording and analysing system has been developed by E.M.I. Electronics Ltd., in conjunction with U.K.A.E.A. scientists and engineers.

The system has been designed to meet the needs of nuclear experiments where continuous monitoring of data for up to 24 hours at a time is often necessary to accumulate enough high accuracy data to carry out subsequent statistical analysis.

The recording units take inputs such as neutron time of flight information and scintillation counter identity and convert them into binary coded form which is then recorded on 16 parallel channels on 1 inch wide magnetic tape at a speed of 1 inch per second or less. These tapes are then removed for fast processing on the central Analyser, which handles the tapes at speeds up to 100 i.p.s., and the data is sorted and addressed into a ferrite core store. The contents

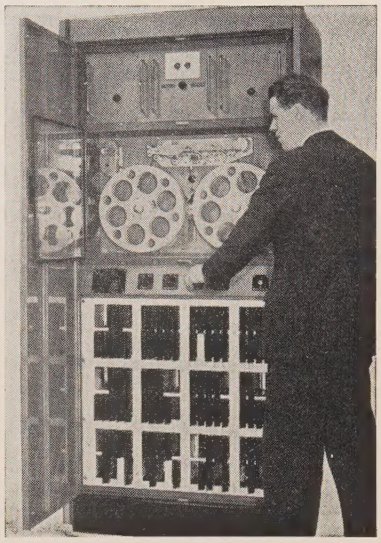

Fig. 1. Recording unit (front view).

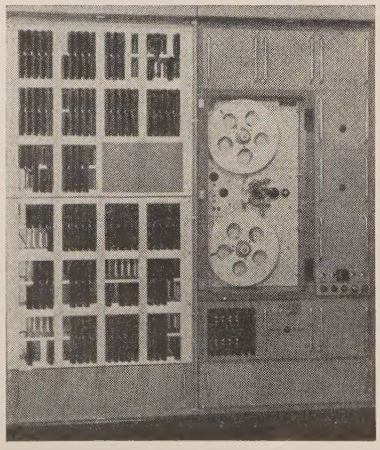

Fig. 2. Analyser unit.

of the core store can then be read out sequentially or at a speed suited to punched paper tape or cards, for direct input into a conventional digital computer.

The central Analyser can digest and sort the information on the output tapes from three independent recording units in a normal 8 hour day, and the preservation of the data in magnetic form releases both the units and the experimental rig under test for fresh work at the end of each run on the 7 200 ft tapes. Similarly, the high speed sorting of the data in the Analyser enables conventional computers to carry out the final calculations with maximum efficiency when fed with programmed data.

DIFFERENTIAL "63" INCREMETER WITH AN EFFECTIVE SCALE LENGTH OF 63″ AND AN ACCURACY OF 0.05 OF 1%

Ad. Auriema, Inc., 85 Broad Street, New York 4, N.Y., U.S.A.

The Incremeter from Sensitive Research Instrument Corp. combines a differential instrument of high comparison accuracy with a highly stable reference source. The instrument's actual scale length of 6.3″ represents only 10% of its total effective scale length. Each 10% of its

full scale range is selected by an incremental switch. Since there are 10 increments (going from 0–0.1, 0.1–0.2 etc. up to 0.9–1.0) it follows that any 10% of the instrument's full scale range is expanded over a full 6.3″ scale length. A 100 division scale becomes a 1 000 division scale in which each division represents 0.1 of 1% of its full scale range. The Incremeter is a direct reading instrument which requires no balancing, nulling or standardizing operations.

Model: INCRE. *Accuracy*: 0.05 of 1% of full scale range. *Type*: Double-pivoted permanent magnet. *Sensitivity*: 200 μA (0.2 μA/division) to 10 A and 200 mV (0.2 mV/division) to 1 000 volts full scale. *Availability*: Single range or switch-controlled multirange models for portable or rack panel mounting. Typical multi-range combination: Code SUPRES 1/10/100/1000 V (1 000 Ω/V) 1/10 100/1000 mA. *Scale*: Hand-drawn. Mirrored. 1 000 divisions. Length 63″ (edgewise panel instrument for rack mounting scale length 70″). *Readability*: 0.01% of full scale range. *Repeatability*: 0.01% or better. *Power input*: 95–135 VAC 60 cycles; 25 va. *Diamond pivots, Temperature compensated, Electrically shielded.*

HONEYWELL INDEX OF LITERATURE

Minneapolis-Honeywell Regulator Company

Industrial Division, Wayne and Windrim Avenues, Philadelphia 44, Penna., U.S.A.

The new Honeywell Index of Literature is now available. This bulletin lists Industrial and Valve Division literature. *Product Catalogs, Specifications, Technical Bulletins, Industry Bulletins, Systems Bulletins, Instrumentation Data Sheets.*

A complete alphabetical subject-company index of *Instrumentation* magazine articles is included.

AN ULTRA-SOUND IMAGE CAMERA

The Institution of Electrical Engineers, Savoy Place London W.C.2

A Television camera which works from sound instead of light and can visualize the internal structure of engineering components and materials and parts of the human body. It can also be used for seeing under water.

Sound waves which carry speech and noises through air or water are in many ways similar to light waves or rays. They can be focused with lenses, and images of objects exposed to noise can be formed and reproduced at a distance.

The wavelengths of audible sounds are too great to make these techniques useful, but for ultra-sound of frequency 1–20 millions of cycles per second the wavelengths in water or oil are only fractions of a millimetre and sound lenses 10 cm across are very efficient.

The ultra-sound "television" camera differs from an ordinary television camera in that the light-sensitive (photo-electric) image-receiving-surface is replaced by a sound-sensitive (piezo-electric) image-receiving-surface. This is simply a bare slice of crystalline quartz which under the impact of sound develops on each point of its surface, a voltage proportional to the ultra-sound intensity. The value of this voltage is detected, point by point, by a scanning electron beam, and after amplification controls the brightness of a television receiver to produce a visible image of the invisible internal structure under examination.

MODEL 137 VHF RELAY

Assembly Products, Inc., Chesterland, Ohio, U.S.A.

Model 137 VHS will trigger control action on signal changes as small as 0.2-microampere, or 0.1-millivolt DC. A rectifier is used for control from AC signals.

The clear plastic case of the Model 137 is only 2 inches long and $1\frac{3}{8}$-inch square. Total length including the 9-pin plug-in base is $2\frac{1}{2}$ inches.

As in an indicating meter-relay, control begins when a contact on the signal "pointer" touches another on a limit pointer. For more positive action, a separate locking coil increases the contact pressure. For reset, either manual or automatic, the locking circuit is opened and a spring snaps the contacts apart.